



**THESIS APPROVAL**  
**GRADUATE SCHOOL, KASETSART UNIVERSITY**

\_\_\_\_\_  
Doctor of Philosophy (Chemistry)

**DEGREE**

\_\_\_\_\_  
Chemistry

**FIELD**

\_\_\_\_\_  
Chemistry

**DEPARTMENT**

**TITLE:** Structures & Reactions of nanoporous and nanostructured Materials  
: In silico Nanoscale Design

**NAME:** Mr. Winyoo Sangthong

**THIS THESIS HAS BEEN ACCEPTED BY**

\_\_\_\_\_  
**THESIS ADVISOR**

( \_\_\_\_\_  
Professor Jumras Limtrakul, Ph.D. \_\_\_\_\_ )

\_\_\_\_\_  
**COMMITTEE MEMBER**

( \_\_\_\_\_  
Assistant Professor Piboon Pantu, Ph.D. \_\_\_\_\_ )

\_\_\_\_\_  
**COMMITTEE MEMBER**

( \_\_\_\_\_  
Mr. Pipat Khongpracha, Ph.D. \_\_\_\_\_ )

\_\_\_\_\_  
**DEPARTMENT HEAD**

( \_\_\_\_\_  
Assistant Professor Noojaree Prasitpan, Ph.D. \_\_\_\_\_ )

**APPROVED BY THE GRADUATE SCHOOL ON** \_\_\_\_\_

\_\_\_\_\_  
**DEAN**

( \_\_\_\_\_  
Associate Professor Gunjana Theeragool, D. Agr. \_\_\_\_\_ )

**THESIS**

**STRUCTURES & REACTIONS OF  
NANOPOROUS AND NANOSTRUCTURED MATERIALS  
: IN SILICO NANOSCALE DESIGN**

**WINYOO SANGTHONG**

**A Thesis Submitted in Partial Fulfillment of  
the Requirements for the Degree of  
Doctor of Philosophy (Chemistry)  
Graduate School, Kasetsart University**

**2009**

Winyoo Sangthong 2009: Structures & Reactions of nanoporous and nanostructured Materials: In silico Nanoscale Design. Doctor of Philosophy (Chemistry), Major Field: Chemistry, Department of Chemistry. Thesis Advisor: Professor Jumras Limtrakul, Ph.D. 98 pages.

Density functional theory (DFT) at B3LYP/6-31G(d,p) level of theory and the our-Own-N-layered-Integrated molecular Orbital + molecular Mechanics (ONIOM) at well calibrated ONIOM(B3LYP/6-31G(d,p):UFF) have been employed to investigate the structures of formaldehyde in Na-exchanged faujasite zeolite and their complexed with propylene. The reaction takes place in a concerted reaction step. The inclusion of the zeolite framework has an influence on the structure and energetics of the adsorption complexes and leads to a lower energy barrier of the reaction (25.1 kcal/mol) as compared to the bare model system (34.4 kcal/mol). If the naked Na ion interacts with the isolated complex, the energy barrier of the system is even lower than the zeolitic system (17.5 kcal/mol), due to the large electrostatic field.

Molecular dynamics simulations of *n*-hexane in siliceous MCM-41 materials, revealed a result of confinement, the adsorption energy of hexane increases when the pore sizes decrease. Also, the adsorption energy increases when the loading is increased from one *n*-hexane molecule to the saturation limit. The self-diffusion coefficients decrease with increasing loadings and when the pore sizes decrease. For low loadings the *n*-hexane molecules lie parallel to the pore channel for every pore size. When the loading is increased, they build up concentric rings.

The stability of nanoclusters and nanocluster-based polymorphs of a range of alkali halides (MX; M= Li, Na, K, Rb, Cs and X= F, Cl, Br, I) are investigated using plane wave density functional theory calculations. For the (MX)<sub>12</sub> clusters, the slab cluster isomers are found to be the most stable cluster type except, for the lithium halide series (LiX). The energy difference between the rock salt phase (rs-MX) and the sodalite phase (SOD-MX) is found to follow the same trend as that between the respective slab and cage (MX)<sub>12</sub> clusters. Correspondingly, the lithium halide sodalite phases (SOD-LiX) are all found to be metastable energetically with respect to the lithium halide rock salt forms (rs-LiX).

---

Student's signature

---

Thesis Advisor's signature

## ACKNOWLEDGEMENTS

I would like to express my gratitude to the following people who gave me the guidance, help and support to reach my goal of researching and writing this thesis. First of all, most of credit for this thesis should justifiably go to my advisor, Professor Jumras Limtrakul, for his supervision, valuable guidance, support and for his patience all the aspects over these years. Furthermore, I would also like to thank my Ph.D. committee members, Assistant Professor Piboon Pantu, Doctor Pipat Khongpracha and the representative of Graduate School, Assistant Professor Saman Mongkolsakulvong, for their useful comments and suggestions to help me fulfill this thesis work.

I would like to express my heartfelt thanks to Professor Michael Probst for his suggestions, encouragement and enthusiasm during the beginning stages of my research work. Professor Francesc Illas Riera and Professor Stefan Thomas Bromley, my supervisors in the University of Barcelona Spain, are also gratefully acknowledged for their valuable guidance, continuous support, kindness, encouragement and assistance throughout the course of my graduate studies.

The financial support from the Royal Golden Jubilee Ph.D. Fellowship the Thailand Research Fund (TRF), the Development and Promotion of Science and Technology Talents Project (DPST), as well as the Kasetsart University Research and Development Institute (KURDI) and the Commission on Higher Education, Ministry of Education under Postgraduate Education and Research Programs in Petroleum and Petrochemicals, and Advanced Materials. Support from the National Nanotechnology Center (NANOTEC Center of Excellence) under the National Science and Technology Development Agency are also acknowledged.

I am very grateful to my colleagues at the Laboratory for Computational and Applied Chemistry (LCAC) at the Physical Chemistry Division, Faculty of Science, Kasetsart University for their providing considerable helpful assistance and encouragement during my studies. Their wonderful meals made me really full and happy. Finally, I would like to thank my parents, elder sisters and relatives for their endless love, support and encouragement.

Winyoo Sangthong

March 2009

## TABLE OF CONTENTS

	<b>Page</b>
TABLE OF CONTENTS	i
LIST OF TABLES	iii
LIST OF FIGURES	v
LIST OF ABBREVIATIONS	ix
INTRODUCTION	1
LITERATURE REVIEW	6
METHODS OF CALCULATIONS	13
Methodologies	13
ONIOM approach	13
Molecular Dynamics simulations	15
Density Functional Theory	19
Models and methods	21
Carbonyl-ene reaction of encapsulated formaldehyde in Na-FAU zeolite	21
Adsorption and diffusion of n-hexane in nanoporous silicate MCM-41	23
Models of “Silanol-Free” Siliceous MCM-41	23
Potential Parameters	26
Details of simulations	31
Stable Nanoporous Alkali Halide Polymorphs	32
RESULTS AND DISCUSSION	35
Carbonyl-ene reaction of encapsulated formaldehyde in Na-FAU zeolite	35
Na-exchanged faujasite zeolite	35
Na-exchanged faujasite encapsulated formaldehyde	36

**TABLE OF CONTENTS (continued)**

	<b>Page</b>
Carbonyl-ene reaction between Na-exchanged faujasite encapsulated formaldehyde and propylene	41
Adsorption and diffusion of <i>n</i> -hexane in mesoporous MCM-41	48
Adsorption energy--effect of pore size	49
Adsorption energy--effect of loading	51
Self-diffusion of <i>n</i> -hexane	51
Vibrational spectra	54
Radial distribution functions	56
Stable Nanoporous Alkali Halide Polymorphs	63
Relative stability of (MX) <sub>12</sub> alkali halide clusters	63
Rock-salt structure versus sodalite structure of bulk alkali halides	72
Stability of SOD-LiF	77
CONCLUSIONS	82
LITERATURE CITED	85
CURRICULUM VITAE	96

**LIST OF TABLES**

<b>Table</b>		<b>Page</b>
1	Details of simulation boxes (supercells) of siliceous MCM-41 models. (starting geometry)	25
2	Mathematical expressions used in the analytical potentials.	28
3	Potential parameters used for siliceous MCM-41. (see equations from Table 2)	29
4	Potential parameters used for hexane molecules with siliceous MCM-41 (see equations in Table 2)	30
5	Sizes of simulation boxes of the siliceous MCM-41 models after relaxation.	32
6	Optimized geometric parameters of reactants, transition state and products of the carbonyl-ene reaction between formaldehyde and propylene on Na-faujasite using the ONIOM2 (B3LYP/6-31G(d,p):UFF) method. (bond lengths are in pm and bond angles are in degrees)	36
7	Atomic charge distribution calculated from the natural population analysis. (NPA)	40
8	Optimized geometric parameters of the carbonyl-ene reaction between formaldehyde and propylene for the bare system and the naked Na(I) ion system from B3LYP/6-31G(d,p) calculations. (bond lengths are in pm and bond angles are in degrees)	42
9	Adsorption energies and self-diffusion coefficients at different <i>n</i> -hexane loadings in siliceous MCM-41 model A to D.	50
10	Total energy per MX unit (in eV) of the slab and cage isomers of the (MX) <sub>12</sub> alkali halide clusters.	65

**LIST OF TABLES (continued)**

<b>Table</b>		<b>Page</b>
11	Total energy per MX unit (in eV) and volume per MX unit (in $\text{\AA}^3$ ) of the rock salt and sodalite phases of the alkali halide polymorphs.	74
12	Properties of a range of LiF polymorphs calculated from the EOS fits to the GGA-DFT: $E_0$ , minimum total energy (eV/LiF), $\Delta E_0$ , total energy differences (eV/LiF), $V_0$ , volume at minimum energy ( $\text{\AA}^3/\text{LiF}$ ) and $B_0$ , the bulk modulus. (GPa/LiF)	81

## LIST OF FIGURES

Figure		Page
1	The illustration of the faujasite zeolite structure model.	2
2	The illustration of the MCM-41 structure model.	3
3	Schematic showing $(MX)_{12}$ nanocage assembly of zeolitic MO phases.	5
4	The two-layer (left) and three-layer ONIOM extrapolation schemes.	14
5	The flow chart of molecular dynamics simulation integrated by using the Verlet algorithm.	18
6	ONIOM2 model of the 84T cluster. The 6-ring quantum cluster is drawn as bond and stick model and the 12T ring window is drawn with sticks: (a) side view; (b) upper view.	22
7	Models A-D of siliceous MCM-41.	24
8	The illustrative of models used in the calculation: (a) a 3x2x1 slab cluster, (b) a cage cluster, (c) a unit cell of rock salt phase and (d) a unit cell of sodalite phase.	33
9	Structures and calculated energy profile (kcal/mol) of the carbonyl-ene reaction in Na-faujasite: (a) HCHO/Na-faujasite complex, (b) coadsorption complex, (c) transition state structure, and (d) product structure.	38
10	Structures and calculated energy profile (kcal/mol) of the carbonyl-ene reaction in Na(I) ion system: (a) HCHO/Na(I) complex, (b) coadsorption complex, (c) transition state structure, and (d) product structure.	39

**LIST OF FIGURES (continued)**

<b>Figure</b>		<b>Page</b>
11	Structures and calculated energy profile (kcal/mol) of the carbonyl-ene reaction in the bare system: (a) coadsorption complex, (b) transition state structure, and (c) product structure.	44
12	Calculated energetic profiles (kcal/mol) for the carbonyl-ene reaction between HCHO and CH <sub>3</sub> CH=CH <sub>2</sub> in the Na-faujasite zeolite system (solid line), the naked Na(I) system (dotted line), and the bare system (dashed line).	47
13	Structures and sizes of siliceous MCM-41 models A to D	48
14	Mean square displacements (MSDs) of the centers of mass of the <i>n</i> -hexane molecules in the models A to D. The loading is indicated on the right hand side of the curves.	53
15	Simulated infrared spectra of silanol-free siliceous-MCM-41 of the models A to D from the normalized correlation functions.	55
16	Centers of mass radial distribution functions of the hexane molecules in models A to D for different loadings. (the curves are shifted vertically by 5 units)	57
17	Centers of mass radial distribution of the hexane molecules at saturation in the four systems and in the liquid phase. (the curves are shifted vertically by 5 units)	58
18	Distribution functions of the distances between the centers of the pore and the center of mass of hexane molecules in models A to D. (the curves are shifted vertically by 5 units)	59
19	Distribution functions at saturation (Figure 6) superimposed on the structures A to D.	61
20	Snapshots from the simulation showing a typical distribution of hexane molecules at saturated loading in models A to D.	62

## LIST OF FIGURES (continued)

<b>Figure</b>		<b>Page</b>
21	Schematic representation of the structure of (a) the slab and (b) the cage structures of the $(MX)_{12}$ alkali halide clusters. Red spheres represent the anion whereas the green spheres represent the cations.	64
22	Total energy MX halides clusters (a) slab and (b) cage as a function of the cation and anion.	67
23	Energy difference per MX unit (in eV) between the slab and cage structure of the $(MX)_{12}$ alkali halide clusters as a function of the cation/anion ionic radius. Each set of points relates to a series maintaining the halide and varying the alkali metal. (the lines are parabolic fits to the points to guide the eye)	68
24	ELF maps for the slab and cage structures of LiF, KF and CsF. The red centres indicate the positions of the alkali metal ions and the blue centres the halide ion positions. The grey area shows the form of the ELF basins for each ion.	71
25	rs-MX and SOD-MX structures of alkali halides viewed as the assembling of (a) $(MX)_{12}$ slabs, (b) $(MX)_{12}$ cage clusters, and (c) the assembling of $(MX)_{12}$ cages. Red spheres represent the anion whereas the green spheres represent the cations.	73
26	Total energy MX halides materials (a: RS and b: SOD) as a function of the cation and anion.	76
27	Energy difference per MX unit (in eV) between the rs-MX and SOD-MX alkali halide materials as a function of the cation/anion ionic radius. Each set of points relates to a series maintaining the halide and varying the alkali metal. (the lines are parabolic fits to the points to guide the eye)	77

**LIST OF FIGURES (continued)**

<b>Figure</b>		<b>Page</b>
28	Energy versus volume phase diagram for various polymorphs of LiF: 1=Rock salt, 2=5-5 (or hexagonal), 3=Wurtzite, 4=Zincblende, 5=SOD 6=LiF-I, 7=LiF-II, 8=LiF-III, and 9=NiAs.	81
29	Snapshot from the MD simulation of the SOD-LiF phase showing a typical configuration of the 2x2x2 super cell at 300 K. Red spheres represent the fluoride anion whereas the green spheres represent the cations.	82

**LIST OF ABBREVIATIONS**

B3LYP	=	Becke's three parameters hybrid functional using the Lee-Yang-Parr correlation functional
BSSE	=	Basis set superposition error
CP	=	Counterpoise
DFT	=	Density functional theory
ELF	=	Electron localization function
FAU	=	Faujasite
FTIR	=	Fourier transform infrared spectroscopy
GGA	=	Generalized gradient approximation
HF	=	Hartree-Fock
K	=	Kelvin
kcal/mol	=	Kilocalories per mol
LDA	=	Local density approximation
LJ	=	Lennard-Jones
MCM-41	=	Mobil composition of matter no. 41
MD	=	Molecular dynamics
MSD	=	Mean square displacement
MAS NMR	=	Magic angle spinning nuclear magnetic resonance
NPA	=	Natural population analysis
ONIOM	=	our-Own-N-layered-Integrated molecular Orbital + molecular Mechanics
rs	=	Rock salt
SOD	=	Sodalite
PAW	=	Projector augmented-wave method
QM/MM	=	Quantum mechanical/molecular mechanical
T	=	Tetrahedral
UFF	=	Universal force field
wz	=	wurtzite

# **STRUCTURES & REACTIONS OF NANOPOROUS AND NANOSTRUCTURED MATERIALS: IN SILICO NANOSCALE DESIGN**

## **INTRODUCTION**

Nanoscience and nanotechnology are multidisciplinary fields which have been attractively studied and developed in recent years. Nanoporous materials also have been paid attention to also in nanoscience and nanotechnology because of their unique properties which are widely used in various fields such as separation, ion exchange, catalysis, biosensor and purification. Zeolites are aluminosilicate, three dimensional, microporous crystalline materials with well defined structures. The structure of zeolites consists of silicon atoms that are tetrahedrally coordinated through oxygen atoms. The replacement of the silicon atom with an aluminium atom causes a negative charge on the system. The negative charge is normally compensated by a cation, which could be easily exchanged by other cations. Zeolites are heterogeneous catalysts that are widely used in modern industry nowadays. They have been intensively studied and utilized for a wide range of applications including adsorption, separation of gases or hydrocarbons and catalysis.

Zeolite catalysts also have the advantages of high selectivity towards the desired product due to the shape-selective properties of their acid sites and their microcrystal pore structure. Faujasite (FAU) is one of the three-dimensional zeolites with large cavities present in the structure that are interconnected by 12-membered ring channels (Figure 1). The catalytic property of a specific zeolite named Na exchanged faujasite is interesting. The Na-faujasite type zeolite can now be used to encapsulate formaldehyde which enables it to suppress the decomposition and self-polymerization without losing the reactivity of formaldehyde toward nucleophiles. As a result, the carbonyl-ene reaction between formaldehyde and olefins has progressively moved toward zeolite-based processes. To clearly envision the

formaldehyde/zeolite system, a theoretical study can provide insight into the reaction mechanisms on a molecular level, thus complementing experimental investigations by obtaining information about properties that are not directly accessible by experimental investigations.

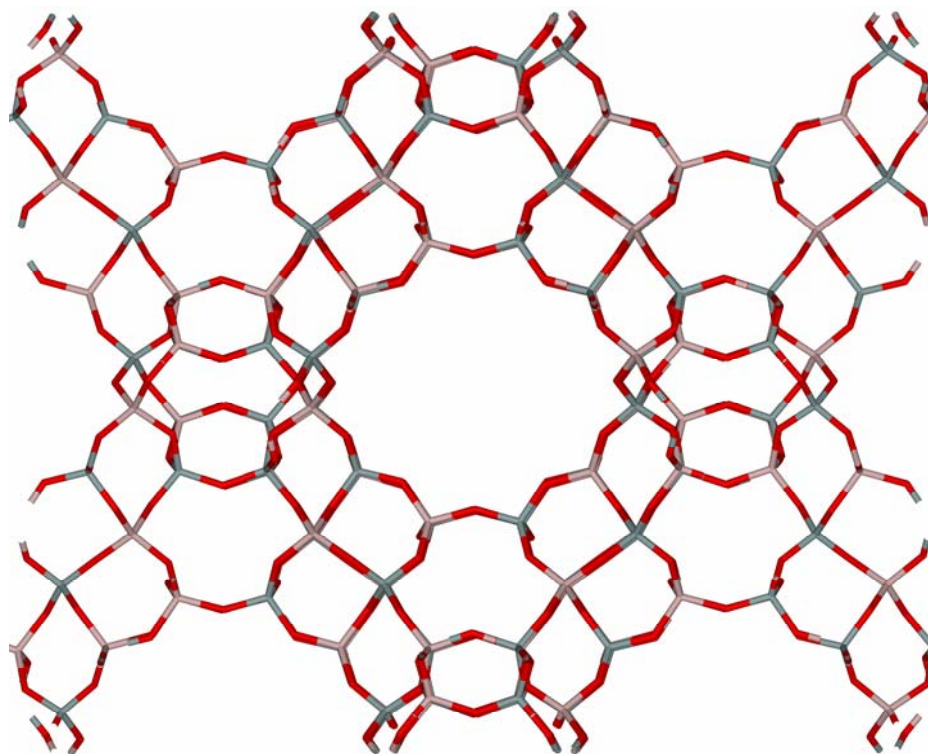


**Figure 1** The illustration of the faujasite zeolite structure model.

There is an important extended framework effect on stabilizing both the adsorption and transition state complexes of reactions in zeolitic systems. To precisely include the effects of the extended zeolite environment on the catalytic properties, one can employ the periodic electronic structure methods such as the periodic density functional theory methodology. However, because of the large unit cells of zeolites, such calculations are often computationally unfeasible. On the other hand, the hybrid methods, such as the combined quantum mechanics/molecular mechanics (QM/MM) methods, as well as the more general ONIOM (our-Own-N-layered-Integrated molecular Orbital + molecular Mechanics) provide a cost effective computational strategy for including the effects of the zeolite framework.

An important line of research has focused on the enlargement of the pore sizes into the mesopore range, allowing large molecules to enter the pore system, to be processed there and then to leave the pore system again. The first synthesis of mesoporous materials was described in 1969. However, due to a lack of analysis, the remarkable features of these materials were not recognized at that time. In 1992, a similar material was obtained by a scientist in Mobil Oil Corporation who discovered the remarkable features of this novel type of silica and opened up a whole new field of research. MCM-41, which stands for Mobil Composition of Matter No. 41, shows a highly ordered hexagonal array of unidimensional pores with a very narrow pore size distribution (Figure 2).

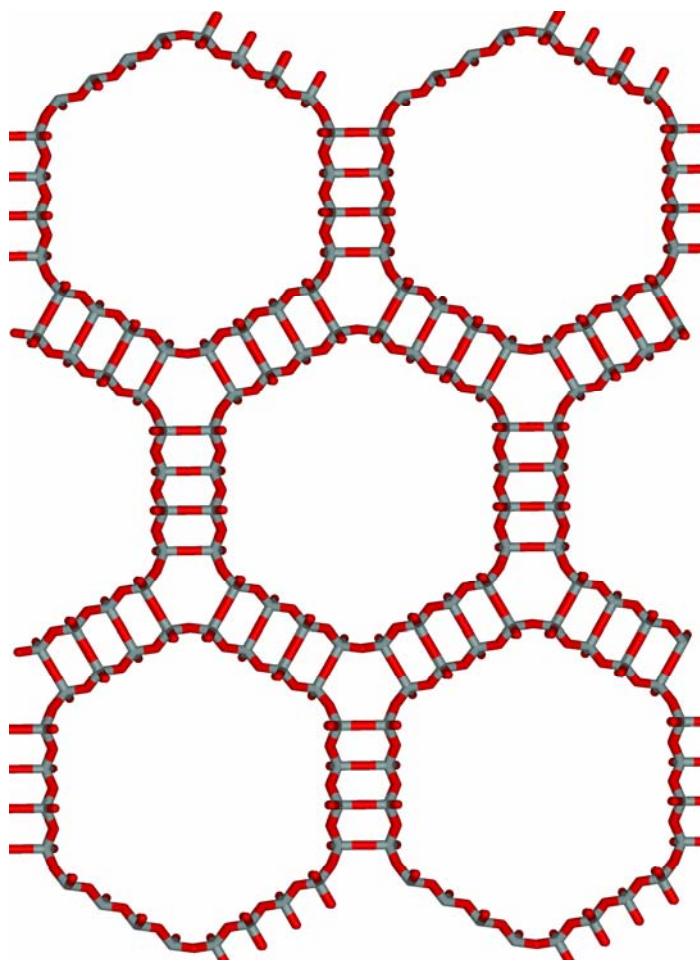


**Figure 2** The illustration of the MCM-41 structure model.

MCM-41 materials possess a regular array of hexagonal, uniform, unidimensional mesopores which can be systematically varied in size from around 16 to 100 Å. These materials bridge the gap between uniform microporous and amorphous mesoporous materials. Such unique characteristics, together with the high surface area open up new potential applications. The framework of MCM-41 is based on an extensive three-dimensional network of oxygen ions that occupied tetrahedral cation sites, and in addition to the  $\text{Si}^{4+}$ , other cations can also occupy these sites. There is no doubt that there exists a strong incentive to use MCM-41, which can deal with bigger molecules and provide better mass transport than zeolites.

In addition to the adsorption property, the influence of the framework structure on diffusion and the details of diffusive processes of molecules adsorbed in the nanoporous materials would be very useful to understand the zeolite behavior and to facilitate the selection of zeolites for a specific application. However, diffusion processes are very difficult to characterize at microscopic level by experiment since all kinds of artifacts, like impurities, defect, etc., may interfere with the measurement and render the interpretation difficult.

With the advance in computer technology and scientific equipment, molecular modeling and simulations are having an increasingly significant impact on the chemical, pharmaceutical, materials and related industries. Molecular modeling and simulations can provide a variety of properties such as transport, chemical, and thermodynamics properties and morphological information for system of interest. Consequently, the diffusion mechanisms of *n*-hexane in silicalite MCM-41 were simulated. Molecular dynamics (MD) simulations are a choice technique to approach this phenomenon.

Moreover, in solid state chemistry, the structure of crystalline solids has been commonly modified by changing the external pressure. This practice has now reached the point where synthesis at very high pressures or even effective negative pressures has become possible, leading to the appearance of low density phases with potential applications. The focus on those materials which can be regarded as formed from

stable cluster building blocks  $(MX)_{12}$  may provide more insight into ways in which these materials maybe fabricated via bottom-up routes (Figure 3). In each case, the zeolitic-like MX phase is constituted solely by the bonded assembly of  $(MX)_{12}$  cages: FAU-MX by bonding via 6+6 atoms interfacial bonding, LTA-MX by  $(MX)_2$  4+4 atoms square-square faces forming, and SOD-MX via M-X 2+2 atoms edge-to-edge interceage interactions forming  $(MX)_2$  linkages.

In this part of work, I utilized the periodic density functional theory (DFT) to explore a wide range of ionic alkali halides for which, in many cases, small clusters have been experimentally generated. The energetic trends of the cluster isomers and their respective bulk phases were compared, throughout the full range of materials which reveals an intriguing link between nanoscale and macroscopic stabilities.



**Figure 3** Schematic showing  $(MX)_{12}$  nanocage assembly of zeolitic MO phases.

## LITERATURE REVIEW

Carbonyl-ene reactions are a common path of hydrocarbon rearrangement and an increasingly useful tool in synthesis. Conventionally, carbonyl-ene reactions proceed according to a concerted mechanism in the presence of Lewis acids as catalysts (Snider, 1980).

In the field of organic chemistry, formaldehyde is well-known as one of the most versatile carbon electrophiles. However, its application is often limited by its intractability due to a low boiling point of  $-19.5\text{ }^{\circ}\text{C}$ . Moreover, it rapidly tends to polymerize to solid paraformaldehyde and trioxane. Therefore, in order to obtain formaldehyde monomer, thermal or Lewis acid treatment is used to depolymerize paraformaldehyde or trioxane, just prior to use. However, these corrosive catalysts cause a number of problems concerning safety, corrosion, handling and waste disposal.

An immense endeavor has been put into developing alternative, more environmentally friendly catalytic systems such as zeolites. Zeolites are important catalysts for many industrial processes, due mainly to their shape- and size-selectivity. Reactions of hydrocarbon compounds on zeolites have been widely studied, especially in hydrocarbon transformation which is a major process of many practical important in the field of oil refining, petrochemical industry and fine chemical productions. More recently, the successful storage of formaldehyde using Na faujasite type zeolite was reported. The appearance of  $^{13}\text{C}$ -labeled formaldehyde encapsulated in Na-faujasite at  $25^{\circ}\text{C}$  was observed by  $^{13}\text{C}$  MAS NMR. Surprisingly, the signal patterns of formaldehyde in Na-FAU remained unchanged after storage in a refrigerator at  $5^{\circ}\text{C}$  for 50 days. Na-FAU enables the suppression of the decomposition and self-polymerization without losing the reactivity of formaldehyde toward nucleophiles. These results demonstrated that the encapsulated formaldehyde is highly stable and can be used as a highly reactive C-electrophile in carbonyl-ene reaction (Okachi and Onaka, 2004).

Theoretical treatments can provide insight into structures or reaction mechanisms of guest molecules in zeolite by giving information about properties that are not directly accessible by experimental investigations. On the one hand, the quantum chemistry techniques are used to address the problem of molecular chemisorption processes and reactions at the Brønsted acid site. Numerous theoretical models, including the periodic electronic structure methods, have been proposed to study intersections in extended systems such as crystals or surface (Limtrakul, 1995; Limtrakul *et al.*, 1997; Sauer *et al.*, 1994).

The disadvantage of such small models is that they do not take into account the effects of the framework, which play an important role to change the structure and energetics of the system significantly. The recent development of hybrid methods such as embedded cluster or combined quantum mechanics/molecular mechanics (QM/MM) method has brought accurate results on a larger system within reach (Braendle and Sauer, 1998; Greatbanks *et al.*, 1996; Khaliullin *et al.*, 2001; Limtrakul *et al.*, 2000; Limtrakul *et al.*, 2001; Sinclair *et al.*, 1998).

The ONIOM (Our-own-N-layer Integrated molecular Orbital and molecular Mechanics) method (de Vries *et al.*, 1999; Svensson *et al.*, 1996) is often applied to study extended systems. Previous studies, the ONIOM method takes advantage of the density functional theory (DFT) for accurate treatment of the interactions of adsorbing molecules with the acid site of zeolite and of the universal force fields (UFF) for representation of the van der Waals interaction due to the confinement effect of the extended zeolitic structure (Bobuatong and Limtrakul, 2003; Kasuriya *et al.*, 2003; Roggero *et al.*, 2001; Tang and Fan, 2000; Torrent *et al.*, 2002). This efficient scheme yielded adsorption energies close to the experimental estimates, suggesting that the ONIOM approach is a sufficiently accurate and practical model for studying adsorption of hydrocarbons on zeolites. Moreover, this methodology success in the study of reaction on zeolitic systems (Choomwattana *et al.*, 2008; Jansang *et al.*, 2006; 2008; Maihom *et al.*, 2008; Namuangruk *et al.*, 2004).

The study of molecular transport phenomena in nanoporous materials are of large interest for the application of these materials in catalysis and separation processes. In contrast to microporous materials like zeolites, which have been extensively investigated by a large variety of experimental techniques of diffusion experiments operating under both equilibrium and non-equilibrium conditions, so far nanoporous host materials of MCM-41 type have been subject of only a rather limited numbers of diffusion studies.

Unlike zeolite, MCM-41 is an innovative mesoporous material consisting of hexagonal, uniform, unidimensional mesopores that do not have a pore channel intersection. The size of the pores can be varied from approximately 1.6 nm to 10 nm and the material has a high surface area of up to  $1000 \text{ m}^2\text{g}^{-1}$  (Beck *et al.*, 1992; Di Renzo *et al.*, 1997; Kresge *et al.*, 1992). The well defined structural characteristics and high thermal and hydrothermal stability of the MCM-41 family of materials makes them an almost perfect model for the study of adsorption and transport properties of guest molecules in mesoporous systems.

The high-silica form of MCM-41 is structurally stable to thermal and hydrothermal treatment. It has great potential for practical use as an adsorbent and mesoporous support for depositing active catalysts. The kinetics and reaction pathways of *n*-hexadecane hydroisomerization and hydrocracking were studied in Pt/MCM-41. The reaction pathways were hypothesized consistent with the concentration of metal. (Girgis and Tsao, 1996).

In the field of catalysis these properties are often studied experimentally by techniques like pulsed field gradient NMR, NMR relaxation, and IR spectroscopy. (Berenguer-Murcia *et al.*, 2003; Boger *et al.*, 1997; Courivaud *et al.*, 2000a; Courivaud *et al.*, 2000b; Hansen *et al.*, 1998; Llewellyn *et al.*, 1995; Nguyen *et al.*, 1998; Qiao *et al.*, 2004; Rathousky *et al.*, 1995; Ribeiro Carrott *et al.*, 2001; Stallmach *et al.*, 2001; Tanchoux *et al.*, 2004; Zhao *et al.*, 1997). However, with experimental methods alone, details of adsorption and diffusion at a microscopic level are very difficult to derive.

Adsorption properties of microporous and mesoporous materials can also be studied by means of simulation methods (Cao *et al.*, 2004; Fox and Bates, 2005; Koh *et al.*, 2002; Sonwane and Li, 2005; Yun *et al.*, 2002). A proven, efficient method for modeling the behavior of organic molecules in nanocatalysts (Hussain and Titiloye, 2005; Kleestorfer *et al.*, 2001; Leroy *et al.*, 2004; Nanok *et al.*, 2005; Rungsirisakun *et al.*, 2006; van Baten and Krishna, 2005; Wongthong *et al.*, 2007) are Molecular Dynamics (MD) simulations, as they provide microscopic level details of the processes as well as macroscopic properties that can be checked against experiments.

The modification of the structure of inorganic crystalline solids through varying the external pressure is now a widely used experimental technique that has led to the discovery of a number of new phases with potential applications (Hemley, 1998; Liu and Bassett, 1986). Theoretical methods have also been widely used to study the behavior of experimentally known ground-state phases of numerous materials under pressure. The structural, energetic, electronic, and optical properties of MgO, ZnO, and CdO in rocksalt, cesium chloride, zinc blende, and wurtzite structures were investigated by using an ab initio pseudopotential method based on density functional theory, generalized gradient corrections to exchange and correlation, and projector-augmented waves. The stability of the ground-state phases rocksalt (MgO, CdO) and wurtzite (ZnO) against hydrostatic pressure and biaxial strain is also studied (Schleife *et al.*, 2006).

Although experiments are now able to effectively maintain negative pressure conditions to explore the possibility of phases lower in density than the ground state, this technique does not yet allow one to investigate a wide class of very low density porous crystalline materials (e.g. zeolites) which are regularly synthesized via bottom-up routes in solution. In order to theoretically explore the feasibility of new crystalline polymorphs, other than those obtained through pressure induced transformations of the most stable phase, global optimization algorithms may be employed to study the energy landscape of materials.

The plausible crystal structures of thirty-eight known binary oxides and various known ternary oxides with the perovskite, pyrochlore and spinel structures were generated by a genetic algorithm (Woodley *et al.*, 1999). The merging ab initio total energy calculations and a specifically devised evolutionary algorithm is an efficient and reliable methodology to predict the most stable crystal structure and a no. of low-energy metastable structures for a given compound (Oganov and Glass, 2006).

Recent work, for instance, provides evidence that materials exhibiting the well-known wurtzite structure such as AlN, GaN, and SiC may exhibit a new graphitic phase as nanofilms. This structure is thermodynamically the most favorable for these thinner films (Freeman *et al.*, 2006). Likewise, ZnO nanostructures have been predicted to experience different types of structural transformations specific to the nanoscale. The infinite large ZnO nanoplates and infinite long ZnO nanowires could transform from wurtzite to graphitic structure below a critical thickness or diameter using a combination of ab initio calculations and analytical formulation, such structural transformation (Zhang and Huang, 2007).

Molecular dynamics simulations and first principles calculations were used to predict a previously unknown phase transformation from wurtzite to a graphite-like hexagonal structure of ZnO nanowires under uniaxial tensile loading (Kulkarni *et al.*, 2006). Compelling evidence that both SiO<sub>2</sub> and MgO may exhibit different stable alternative phases in thin films grown on metal substrates has also been reported. The scanning tunneling microscopy, IR reflection absorption spectroscopy, and XPS were used to study the structure of a thin single crystal SiO<sub>2</sub> film grown on Mo(112). The density functional theory calculations show excellent agreement with the experimental results (Weissenrieder *et al.*, 2005). Free and Ag(111)-supported MgO(111) ultrathin films were studied using an ab initio total energy approach. The graphite like structure were predicted at low thickness, films which are either unsupported or deposited on Ag(111) suggesting new methods to engineer oxide nanostructures (Goniakowski *et al.*, 2004).

Recently, some of our colleagues reported on the prediction of low density nanoporous polymorphs of MgO, ZnO (Carrasco *et al.*, 2007) and SiO<sub>2</sub> (Wojdel *et al.*, 2006) based on the assembly of highly stable nanoclusters. MgO and ZnO were predicted as that new low-density nanoporous crystal phases via the coalescence of nanocluster building blocks using accurate electronic structure calculations. The cagelike (MO)<sub>12</sub> clusters exhibit particularly high gas phase stability, leading to new polymorphs with energetic stabilities rivaling (and sometimes higher) than those of known MO polymorphs (Carrasco *et al.*, 2007). The highly stable (SiO<sub>2</sub>)<sub>8</sub> magic clusters are predicted to be strongly energetically preferred while also having the propensity to form intercluster siloxane (Si-O-Si) bridges. Silicate framework materials are thus proposed with density functional calculations and they differ from known synthesized materials with the most stable frameworks lying in a thermodynamically accessible window shared by mesoporous silicas (Wojdel *et al.*, 2006).

In contrast to top-down global optimizations, this approach can be regarded as a bottom-up means to materials prediction. Although both top-down and bottom-up approaches both aim to find new stable polymorphs the former directly searches through the space of possible polymorphs whereas the latter aims first to find stable building blocks (e.g. through global optimization of cluster isomers and then materials that may be regarded as arising from their assembly. Although both approaches are quite complementary, the focus on those materials which can be regarded as formed from stable cluster building blocks may provide more insight into ways in which these materials maybe fabricated via bottom-up routes. The prediction of stable polymorphs of MgO and ZnO as low density zeolitic analogues, derived from the bottom-up assembly of highly stable (MO)<sub>12</sub> cluster building blocks strongly suggests that similar nanoporous phases are likely to be stable for different types of materials.

The study of gas-phase cluster ions of alkali halides have been widely investigated by mass spectrometric because of their elementary properties. Alkali halide cluster ions have been produced so far by using such methods as low-energy electron beam (Pflaum *et al.*, 1985), laser vaporization (Bloomfield *et al.*, 1991; Twu

*et al.*, 1990), and fast-atom bombardment (Barlak *et al.*, 1981; Barlak *et al.*, 1982; Campana *et al.*, 1981; Ens *et al.*, 1983; Katakuse *et al.*, 1988). The positive charge clusters decay to stable neutral rectangular clusters by the emission of small positive fragments or grow to larger stable neutral clusters by the attachment of small negative clusters.

In relation to the present work on alkali halide polymorphs, the recent careful investigations of a range of known and new hypothetical polymorphs of the alkali halides were studied. These works are based on empirical potential based global optimization followed by refined energy evaluation by DF calculations crystal global optimizations generally start from the assumption of a bulk periodic crystal cell occupied by atoms, and make use of different algorithms to modify the atomic positions and cell dimensions towards possible minima (Doll *et al.*, 2007). Such approaches may be described as top-down approaches. Increasing evidence indicates that the atomic structure of materials at the nanoscale, where the assumption of long range crystalline periodicity breaks down, can be significantly different from that exhibited by bulk materials.

## METHODS OF CALCULATIONS

### Methodologies

In this thesis, three methodologies of theoretical calculations were utilized on three nanoporous systems. First, an ONIOM scheme was used to model the effect of the environment on the carbonyl-ene reaction in Na-exchanged FAU zeolite. Second, the molecular dynamics (MD) simulations method was performed to study the adsorption and diffusion of *n*-hexane in siliceous form of MCM-41. Finally, the nanoporous structures of alkali halide compounds were predicted by utilizing periodic density functional theory (DFT). It is important to understand the background theory of these methods, therefore in order to assess the reliability of the results they should be discussed in some details in the following sections.

### **ONIOM (Our-own N-layered Integrated molecular Orbital and molecular Mechanics)**

ONIOM is the hybrid method that developed by Morokuma and co-workers (Svensson *et al.*, 1996). The basic idea is the partitioning of the whole system into two or more different parts or layers. The objective is to perform a high-level calculation on just a small part of the system and to include the effects of the remainder at lower levels of theory, with the end results being of similar accuracy to a high-level calculation on the full system.

In the quantum mechanical calculations, only a small active part of the zeolite lattice is accurately approximated by quantum mechanical methods. This quantum mechanical region is referred to as the cluster. The rest of the crystal will be called the environment, which is usually calculated by less accurate methods. The interaction between quantum cluster and its environment is described exclusively by molecular mechanics. The environment can be modeled by either a force field or a computationally less expensive quantum mechanical method. The former is known as a hybrid quantum mechanics and molecular mechanics (QM/MM) method (Deka and

Hirao, 2002; Hillier, 1999; Joshi and Thomson, 2005; Sherwood *et al.*, 2003) and the latter is recognized as the more general ONIOM (our own N-layered integrated molecular orbital and molecular mechanics) scheme. Applications of the ONIOM methodology to study the reactions in zeolites have recently been reported (Bobuatong and Limtrakul, 2003; Choomwattana *et al.*, 2008; Jansang *et al.*, 2006; 2008; Kasuriya *et al.*, 2003; Maihom *et al.*, 2008; Namuangruk *et al.*, 2004; Roggero *et al.*, 2001; Tang and Fan, 2000; Torrent *et al.*, 2002).

The small region of the system where the chemical process takes place, such as bond breaking and formation, is treated with a high level quantum mechanical method, while the remainder of the system is treated at a lower level. Each layer can, in principle, be treated at an arbitrary level of theory. The two-layer and three-layer ONIOM extrapolation schemes are shown in Figure 4.

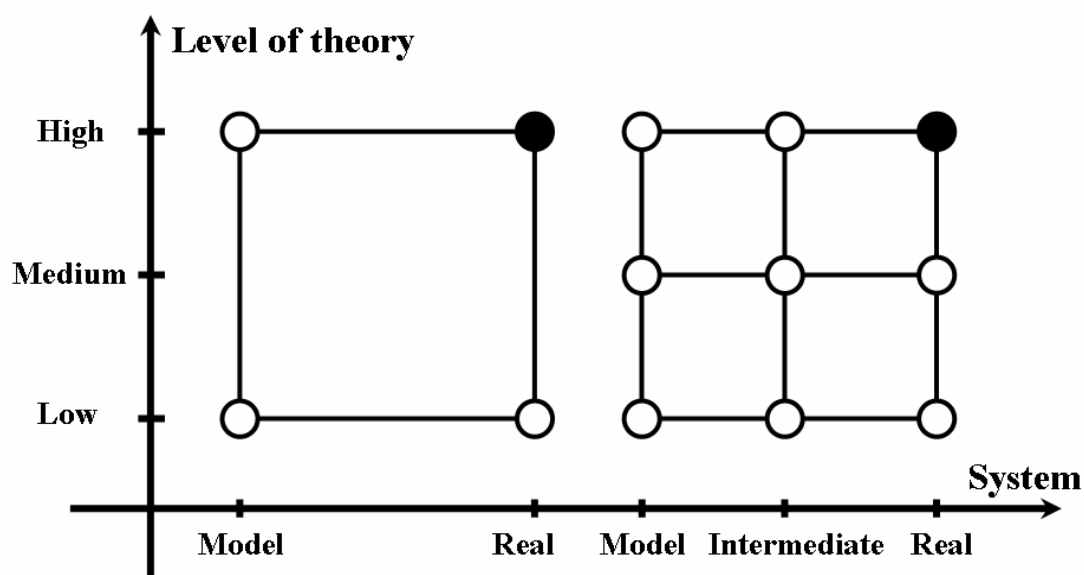


**Figure 4** The two-layer (left) and three-layer ONIOM extrapolation schemes.

The two-layer model requires a high and low level of theory and real and model systems. The energy at the high-level of theory for the real geometry is estimated as

$$E_{Real}^{High} = E_{Model}^{High} - E_{Model}^{Low} + E_{Real}^{Low} \quad (1)$$

The three-layer model requires high, medium and low levels of theory, and real, intermediate and model geometries and the corresponding energy estimate is

$$E_{Real}^{High} = [E_{Model}^{High} - E_{Model}^{Medium}] + [E_{Inter}^{Medium} - E_{Inter}^{Low}] + E_{Real}^{Low} \quad (2)$$

### Molecular Dynamics (MD) simulations

The study of the microscopic behavior of interested systems of interacting particles can be performed by Molecular dynamics (MD). The basis concept of this method is that the motions of the system are solved by the classical equations of motion. This technique was invented by Alder and Wainwright in order to investigate the phase behavior and transport properties in the hard sphere gas in 1957 (Alder and Wainwright, 1957).

In molecular dynamics, at a given potential energy function  $U(r_1, r_2, r_3, \dots, r_N)$  for a system of  $N$  interacting particles, the configurations of the system are generated by integrating of the equation of motion from Newton's laws.

$$F_i = m_i a_i = \frac{d^2 r_i}{dt^2} \quad (3)$$

where  $F_i$  is the force on particle  $i$  due to its interactions with other particles,  $m_i$  is the mass of particle  $i$ , and  $a_i$  is the acceleration of particle  $i$ . The force is determined from the potential energy function, which is a sum of pair potentials.

$$U(r_1, r_2, r_3, \dots, r_N) = \sum_{i>j} u(r_{ij}) \quad (4)$$

where  $r_{ij}$  is the separation between particle  $i$  and  $j$ . The force  $F_i$  acting on particle  $i$  is then:

$$F_i = -\frac{\partial U}{\partial r_i} = \sum_{i \neq j} f_{ij} \quad (5)$$

Here the  $f_{ij}$  is the force on particle  $i$  due to its interaction with particle  $j$ :

$$f_{ij} = -\frac{\partial u(r_{ij})}{\partial r_{ij}} \quad (6)$$

In the presence of the interaction potential, the motions of all the particles are relativistic, giving rise to a many-body problem that cannot be solved analytically. In such circumstances, the equations of motions are integrated by using a finite difference method that can be solved iteratively. To generate molecular dynamics trajectories, the integration is divided into numerous small stages, each separated by a fixed time step of  $\delta t$ . The total forces act on the particles in the configuration at a time  $t$  is used to determine their accelerations, which are then combined with the positions and velocities at a time  $t$  to calculate the positions and velocities at time  $t + \delta t$ . The forces that act on the particles in their new positions are then obtained, leading to new positions and velocities at time  $t + 2\delta t$ , and so on.

In this study, the Verlet algorithm was chosen for integrating the equations of motion (Verlet, 1967). This algorithm is known to be simple and stable and widely used methods in molecular dynamics. The advance of positions is approximated from the one-step forward and one-step backward of the Taylor series expansion truncated after the third term:

$$r(r + \delta t) = r(t) + v(t)\delta t + \frac{1}{2}a(t)\delta t^2 + \frac{1}{6}b(t)\delta t^3 \quad (7)$$

$$r(t - \delta t) = r(t) - v(t)\delta t + \frac{1}{2}a(t)\delta t^2 - \frac{1}{6}b(t)\delta t^3 \quad (8)$$

where  $v$  is the velocity (the first derivative of the positions with respect to time),  $a$  is the acceleration (the second derivative), and  $b$  is the third derivative. Summation of the two equations above gives

$$r(t + \delta t) = 2r(t) - r(t - \delta t) + a(t)\delta t^2 \quad (9)$$

The velocities can be calculated in a variety of ways. A simple approach is to divide the difference in positions at time  $t + \delta t$  and  $t - \delta t$  by  $2\delta t$

$$v(t) = \frac{r(t + \delta t) - r(t - \delta t)}{2\delta t} \quad (10)$$

Figure 5 shows the flow chart of a molecular dynamics simulation integrated by using the Verlet algorithm.

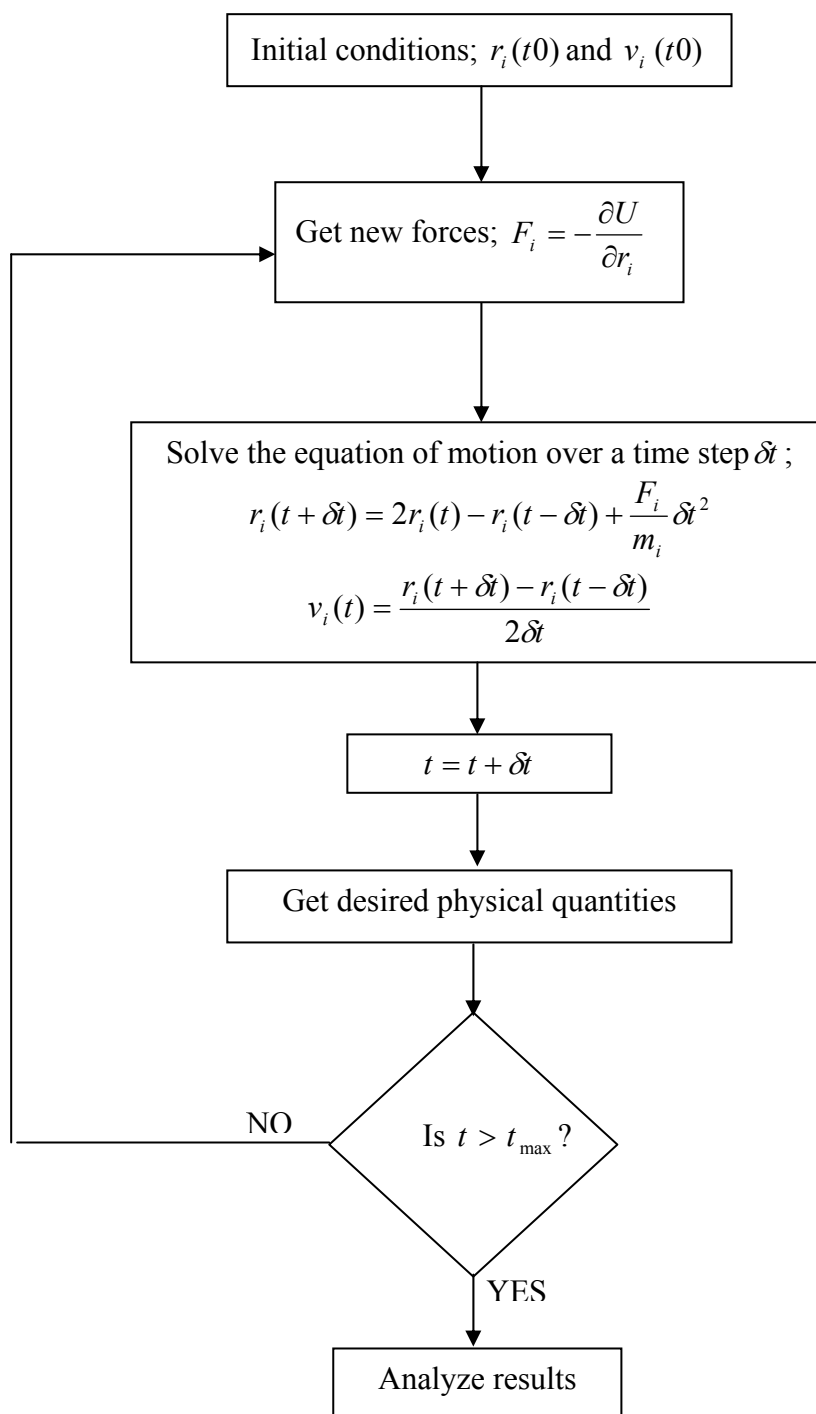


**Figure 5** The flow chart of molecular dynamics simulation integrated by using the Verlet algorithm.

## Density Functional Theory (DFT)

Most of works in this thesis are performed utilizing the Density Functional Theory (DFT). Therefore, brief description details of the DFT are summarized here in order to provide an overview of the quantum mechanical techniques.

The basic idea of the DFT is that the energy of the interested system is a functional of electron density( $\rho$ ),  $E[\rho]$  and the electron density is a function of position( $r$ ),  $\rho(r)$ . The energy functional of an N-electrons system is

$$E[\rho] = T[\rho] + V_{ext}[\rho] + V_{ee}[\rho] \quad (11)$$

where  $T[\rho]$  is total kinetic energy,  $V_{ext}[\rho]$  is the interaction with the external potential which denoted by

$$V_{ext}[\rho] = \int \hat{V}_{ext} \rho(r) dr \quad (12)$$

and  $V_{ee}[\rho]$  is electron-electron potential energy.

Since  $T[\rho]$  and  $V_{ee}[\rho]$  are unknown, Kohn and Sham proposed to approximate the kinetic and e-e functionals. They introduced a system of N non-interacting electrons to be described by a single determinant wavefunction in N orbitals;  $\phi$ . The kinetic energy and electron density are known exactly from the orbitals;

$$T_s[\rho] = -\frac{1}{2} \sum_{i=1}^N \langle \phi_i | \nabla^2 | \phi_i \rangle \quad (13)$$

$$\rho(r) = \sum_{i=1}^N |\phi_i|^2 \quad (14)$$

The electron-electron interaction will be the classical Coulomb interaction

$$V_H[\rho] = \frac{1}{2} \int \frac{\rho(r_1)\rho(r_2)}{|r_1 - r_2|} dr_1 dr_2 \quad (15)$$

The energy functional can be rearranged as;

$$E[\rho] = T_s[\rho] + V_{ext}[\rho] + V_H[\rho] + E_{xc}[\rho] \quad (16)$$

where they have introduced the exchange-correlation functional;

$$E_{xc}[\rho] = (T[\rho] - T_s[\rho]) + (V_{ee}[\rho] - V_H[\rho]) \quad (17)$$

$E_{xc}$  is simply the sum of the error made of using a non-interacting kinetic energy and treating the electron-electron interaction classically.

The major problem of DFT is that an exact term of  $E_{xc}[\rho]$  is unknown so approximate functionals must be used. Therefore, many types of functionals are available; the simplest approximation is the local-density approximation (LDA), which is assumed that the density locally can be treated as a uniform gas. The Generalized Gradient Approximation (GGA) functionals include the derivatives of the electron density. The Hybrid functional has also been proposed. The B3LYP functional is the most widely used functional nowadays. DFT can be implemented either with an atom-centered localized basis set or with a plane-wave basis set. Such basis sets are also used in this thesis works as will be stated in the “Models and Methods” part.

## Models and methods

### Carbonyl-ene reaction of encapsulated formaldehyde in Na-FAU zeolite

In the present study, the ONIOM method has been employed to model the active site of alkaline-exchanged zeolites. Specifically, the reaction mechanism of the carbonyl-ene reaction between an encapsulated formaldehyde molecule and alkene on Na-exchanged faujasite was studied. Propylene was chosen to represent an alkene molecule because it is the smallest one with the required basic structure. This work also studies the carbonyl-ene reaction without the zeolite oxygen framework surrounding the alkaline cation in order to understand the role of alkaline-exchanged zeolites in the carbonyl-ene reaction.

This system is described by three models of different sophistication: (1) The ONIOM2 (B3LYP/6-31G(d,p):UFF) approach is applied to a model of 84T faujasite. The 84T cluster includes two supercages serving as a nanometer-size chemical reactor where the adsorbates can be trapped inside. Its geometry is taken from the lattice structure of faujasite zeolite (Olson and Dempsey, 1969). For Na-exchanged faujasite, the alkaline-metal cation does not bind with a particular bridging oxygen atom of  $[\text{AlO}_4]^-$  but sits in front of the 6-ring inside the supercage (Beauvais *et al.*, 2004) (Figure 6). The interaction of the cationic metal with the zeolite framework leads to perturbation of the active acidic site.

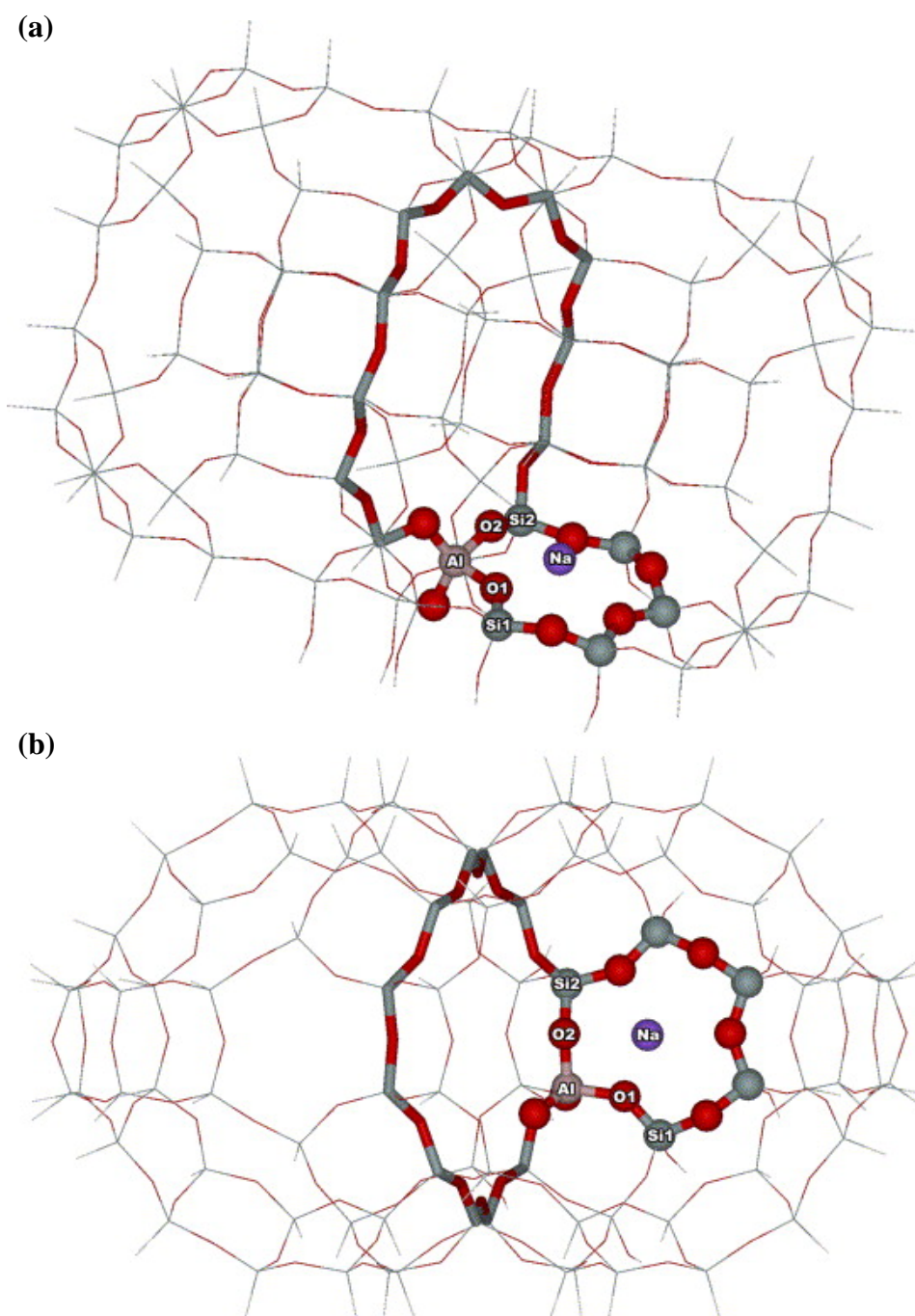


**Figure 6** ONIOM2 model of the 84T cluster. The 6-ring quantum cluster is drawn as bond and stick model and the 12T ring window is drawn with sticks: (a) side view; (b) upper view.

The active region consists of the 6-ring inside the supercage, which can be considered as the smallest unit required to represent the acidic site of zeolite and that of the reactive molecules. It is treated with the B3LYP density-functional and the 6-

31G(d,p) basis set. The extended framework environment is included on the molecular mechanics level with the universal force field (UFF). (2) Density-functional calculations with the same method and basis set but without the zeolite, i.e. on Na(I)/HCHO/CH<sub>3</sub>CH=CH<sub>2</sub> and (3) on the two reactants alone, i.e. on HCHO/CH<sub>3</sub>CH=CH<sub>2</sub>, were also performed.

All the computational work has been performed by using the Gaussian98 code. In the ONIOM2 method, only the 6-ring quantum cluster (NaSi<sub>5</sub>AlO<sub>8</sub>, see figure 6) and the adsorbates (HCHO and CH<sub>3</sub>CH=CH<sub>2</sub>) were fully optimized. Normal mode analyses were carried out to verify the transition states to have one imaginary frequency whose mode correspond to the designated reaction. In (2) and (3) all atomic positions are optimized. For all three models, additional single-point energy calculations with the 6-311++G(d,p) basis sets have also been carried out, and the basis set superposition errors (BSSE) were estimated by the counterpoise (CP) method. The charge distribution in the complexes has been analyzed via the natural population analysis (NPA) (Carpenter and Weinhold, 1988; Foster and Weinhold, 1980; Reed *et al.*, 1988; Reed and Weinhold, 1983; Reed *et al.*, 1985) partitioning scheme applied to the B3LYP/6-31G(d,p) densities.

## **Adsorption and diffusion of n-hexane in nanoporous silicate MCM-41**

### **Models of “Silanol-Free” Siliceous MCM-41**

From experiments, it is known that the MCM-41 possesses a hexagonally packed array of one-dimensional cylindrical pores with a large surface area and pore volume. However, a definitive model of MCM-41 has never been presented because of the difficulty of measuring its noncrystalline atomic structure. A hypothetical perfect lattice of siliceous MCM-41 as a model for the high silica form of amorphous MCM-41 was used. The initial atomic coordinates were generated with the procedure used in previous work (Nanok *et al.*, 2005). By this method, it could vary the pore size and the length of the pores by varying the numbers of silicon tetrahedral atoms of the side of the hexagonal channels. Four orthorhombic supercells of siliceous MCM-

41 with different pore sizes in the simulations denoted as models A (3 Si tetrahedral atoms), B (4 Si tetrahedral atoms), C (5 Si tetrahedral atoms) and D (6 Si tetrahedral atoms) were generated. Each of the models contains two parallel hexagonal channels running along the  $z$ -axis. Their dimensions are given in Table 1 and they are illustrated in Figure 7. Although the terminal silanol groups (Si-OH) were not included in our models, the interaction between sorbate molecules and these groups are considered implicitly by our fitting procedure to reproduce the experimental heat of adsorption of  $n$ -hexane in siliceous MCM-41.

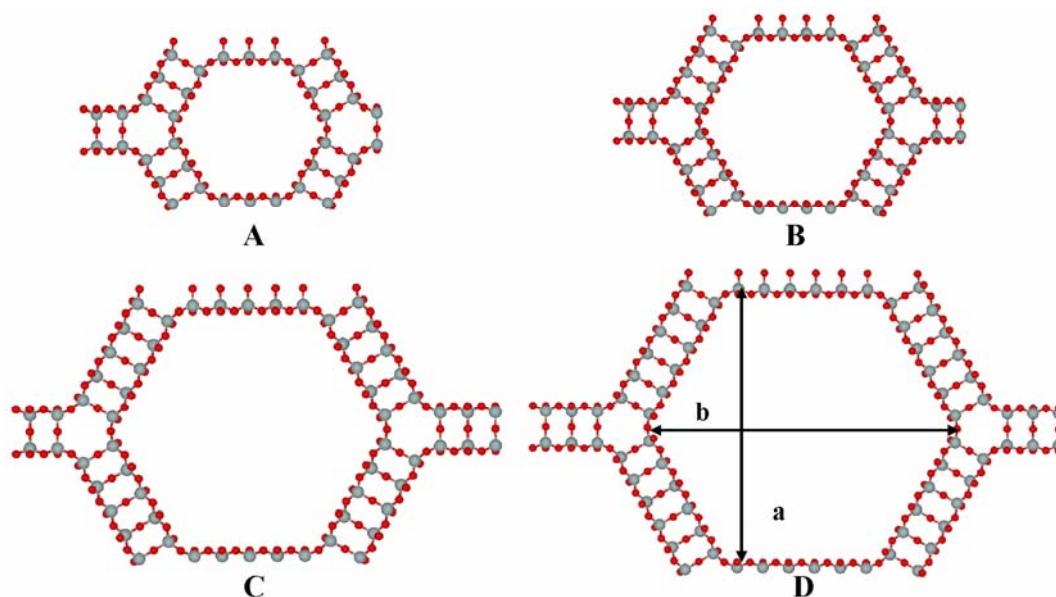


**Figure 7** Models A to D of siliceous MCM-41.

**Table 1** Details of simulation boxes (supercells) of siliceous MCM-41 models. (starting geometry)

Model	number of atoms			Diameters of the pore (Å)		simulation box (Å)			$R_{\text{cut off}}$ (Å)
	Si	O	Total	a	b	X	Y	Z	
A	288	576	864	13.80	15.93	31.36	18.06	36.65	9.00
B	384	768	1152	18.40	21.24	39.31	22.66	36.60	11.10
C	480	960	1440	23.00	26.55	47.26	27.24	36.68	13.50
D	576	1152	1728	27.59	31.86	55.21	31.84	36.66	15.80

### Potential parameters

The potentials of the adsorption complex can be divided into four terms of the total potential function:

$$V_{total} = V_{intraMCM} + V_{intrahexane} + V_{hexane-hexane} + V_{MCM-hexane} \quad (18)$$

where  $V_{intraMCM}$  is the intramolecular potential energy of zeolite,  $V_{intrahexane}$  is the intramolecular potential energy of the  $n$ -hexane molecules,  $V_{hexane-hexane}$  is the potential energy between  $n$ -hexane molecules and  $V_{MCM-hexane}$  is the potential energy between  $n$ -hexane molecules and the zeolitic wall.

The potential energy functions of the siliceous MCM-41 framework,  $V_{intraMCM}$  was approximated by a generalized valence force field (GVFF) from the work of Nicholas et al. (Nicholas *et al.*, 1991). The Si-O bond stretch and O-Si-O angle bend are approximated by simple harmonic potentials while Si-O-Si angle bends are modeled with quadratic potentials. The equilibrium values of bond distances,  $r_0$  and bond angles,  $\theta_0$  are taken from the structural data (Nanok *et al.*, 2005). The potential energy functions are documented in Table 2 and Table 3, respectively. The intramolecular potential energy of the  $n$ -hexane molecule was described by the following expression:

$$V_{intrahexane} = V_{stretch} + V_{bend} + V_{torsion} + V_{vdW} + V_{coul} \quad (19)$$

where  $V_{stretch}$ ,  $V_{bend}$ ,  $V_{torsion}$ , and  $V_{coul}$  are taken from the work of Allinger (Allinger - 1989). A Lennard-Jones potential describes the van der Waals interactions. All intermolecular interactions were expressed by Lennard-Jones plus Coulomb terms. The parameters for the interactions between MCM-41 and  $n$ -hexane were obtained from the C-Si, C-O, H-Si and H-O interaction terms by applying the Lorentz-Berthelot combination rules:

$$\varepsilon_{ij} = \sqrt{\varepsilon_i \varepsilon_j} \quad (20)$$

$$\sigma_{ij} = \frac{\sigma_1 + \sigma_2}{2} \quad (21)$$

Scaling were applied to the  $\varepsilon$  parameters of the Lennard-Jones terms for the interactions between MCM-41 and *n*-hexane (C-Si, C-O, H-Si, and H-O) iteratively until the simulated adsorption energy of *n*-hexane in siliceous MCM-41 resulting from the simulations was close to the experimental values (-8.85 to -9.33 kcal/mol) for the same pore size (Janchen *et al.*, 1998; Trens *et al.*, 2005; Zhao *et al.*, 2001). These adjusted parameters and the ones for the hexane-hexane interactions are given in Table 4. Partial charges of half the formal charge, +2.0 for Si and -1.0 for O of MCM-41, were used (Demontis *et al.*, 1995). The partial charges of the C and H atoms of *n*-hexane were obtained from a Mulliken population analysis at the MP2/6-311++G(d,p) level by the Gaussian03 code.

**Table 2** Mathematical expressions used in the analytical potentials.

Type of potential	Functional form	Used in
Harmonic stretching	$V_{two-body} = \frac{1}{2}k(r - r_0)^2$	$V_{MCM}, V_{hexane}$
Harmonic bending	$V_{three-body} = \frac{1}{2}k(\theta - \theta_0)^2$	$V_{MCM}, V_{hexane}$
Quartic bending	$V_{three-body} = \frac{k}{2}(\theta - \theta_0)^2 + \frac{k'}{3}(\theta - \theta_0)^3 + \frac{k''}{4}(\theta - \theta_0)^4$	$V_{MCM}$
Bond torsion	$V_{four-body} = \frac{1}{2}V_1(1 + \cos(\phi)) + \frac{1}{2}V_2(1 - \cos(2\phi)) + \frac{1}{2}V_3(1 + \cos(3\phi))$	$V_{hexane}$
Lennard-Jones	$V_{Lennard-Jones} = 4\epsilon \left[ \left( \frac{\sigma}{r_{ij}} \right)^{12} - \left( \frac{\sigma}{r_{ij}} \right)^6 \right]$	$V_{hexane}, V_{MCM-hexane}, V_{hexane-hexane}$
Coulomb	$V_{coul} = \frac{q_i q_j}{4\pi\epsilon_0 r_{ij}}$	$V_{MCM-hexane}, V_{hexane-hexane}$

**Table 3** Potential parameters used for siliceous MCM-41.

(see equations from Table 2)

<b>Two-body parameters</b>	
$r(\text{Si-O})$	
$k$ (kcal/mol)	597.32
$r_0$ (Å)	1.626
<b>Three-body parameters</b>	
$\theta(\text{O-Si-O})$	
$k$ (kcal/mol)	138.12
$\theta_0$ (°)	109.47
$\theta(\text{Si-O-Si})$	
$k$ (kcal/mol)	10.85
$k'$ (kcal/mol)	-34.08
$k''$ (kcal/mol)	26.52
$\theta_0$ (°)	121.80, 141.06, 179.47 for the three non-equivalent positions of oxygen

**Table 4** Potential parameters used for *n*-hexane molecules with siliceous MCM-41.  
(see equations in Table 2)

<b>Two-body parameters</b>		$k$ (kcal/mol)	$r_0$ (Å)
C-C		646.56	1.528
C-H		682.56	1.112
<b>Three-body parameters</b>		$k$ (kcal/mol)	$\theta_0$ (°)
C-C-C		96.48	109.50
C-C-H		84.96	109.80
H-C-H		79.20	107.60
<b>Four-body parameters</b>			
	$V_1$ (kcal/mol)	$V_2$ (kcal/mol)	$V_3$ (kcal/mol)
C-C-C-C	0.185	0.170	0.520
C-C-C-H	0.000	0.000	0.280
H-C-C-H	0.000	0.000	0.238
<b>Lennard-Jones parameters</b>		$\varepsilon$ (kcal/mol)	$\sigma$ (Å)
C-C		0.05144	3.3438
C-H		0.05317	2.9918
H-H		0.05496	2.6398
C-Si		0.04377	3.6518
H-Si		0.04524	3.2998
C-O		0.02400	3.2030
H-O		0.02481	2.8510

### Details of simulations

Molecular dynamics simulations were performed using the DL\_POLY 2.0 code. The classical equations of motion of the atoms in the periodic models of siliceous MCM-41 with four different pore diameters were solved by means of the Verlet algorithm. The systems, denoted as A-D, are shown in Figure 7. Loading started with one *n*-hexane molecule and was increased up to the point where the density of *n*-hexane, calculated from the pore volume and the number of molecules, equals the density of liquid *n*-hexane. For comparison, the molecular dynamics simulations of liquid *n*-hexane were also performed in order to determine the confinement effects of siliceous MCM-41 on the liquid structure. This system consisted of 124 *n*-hexane molecules in a periodic box with a size of 30×30×30 Å. The initial structures of the four MCM-41 models with empty pores were first relaxed by simulating in the  $NpT$  ensemble for 500 ps. The structures of the models were then inspected and their radial pair distribution functions were checked. It was found that the dimensions of the supercells (reported in Table 5) stayed very close to the respective starting values. (shown in Figure 7 and Table 1) The resulting geometry was used as the starting structure for  $NVE$  simulations. These simulations were performed with a time step of 1 fs at room temperature (300 K). The resulting configurations were used as input for a 200 ps equilibration period with velocity rescaling. After this period, a simulation over 200 ps was performed without velocity rescaling to ensure that there were no further drifts. In a subsequent 100 ps production run in the  $NVE$  ensemble coordinates and velocities of the atoms were stored every 10 fs for subsequent analysis.

**Table 5** Sizes of simulation boxes of the siliceous MCM-41 models after relaxation.

Model	simulation box (Å)		
	X	Y	Z
A	31.36	18.06	36.65
B	39.31	22.66	36.60
C	47.26	27.24	36.68
D	55.21	31.84	36.66

### Stable Nanoporous Alkali Halide Polymorphs

In order to explore low density phases of the alkali halides, two different sets of DFT calculations were carried out. In the first, the differences between the most energetically stable cluster isomers were calculated, and in the second we obtained the energy versus volume equation of state (EOS) of the extended bulk polymorphs.

In the case of the clusters, this study considered two low energy  $(MX)_{12}$  isomers for all alkali halides: a  $3 \times 2 \times 1$  slab and a discrete SOD cage (Figure 8a and 8b). For the solids, although in principle we may use same  $(MX)_{12}$  units and reduce the vacuum space between the periodically repeated units in such a way that a bulk structure is created, it was computationally more convenient to use the typical cubic unit cell composing 8 atoms for rs-MX and a cubic unit cell containing 12 atoms of a cage for SOD-MX (Figure 8c and 8d), respectively.

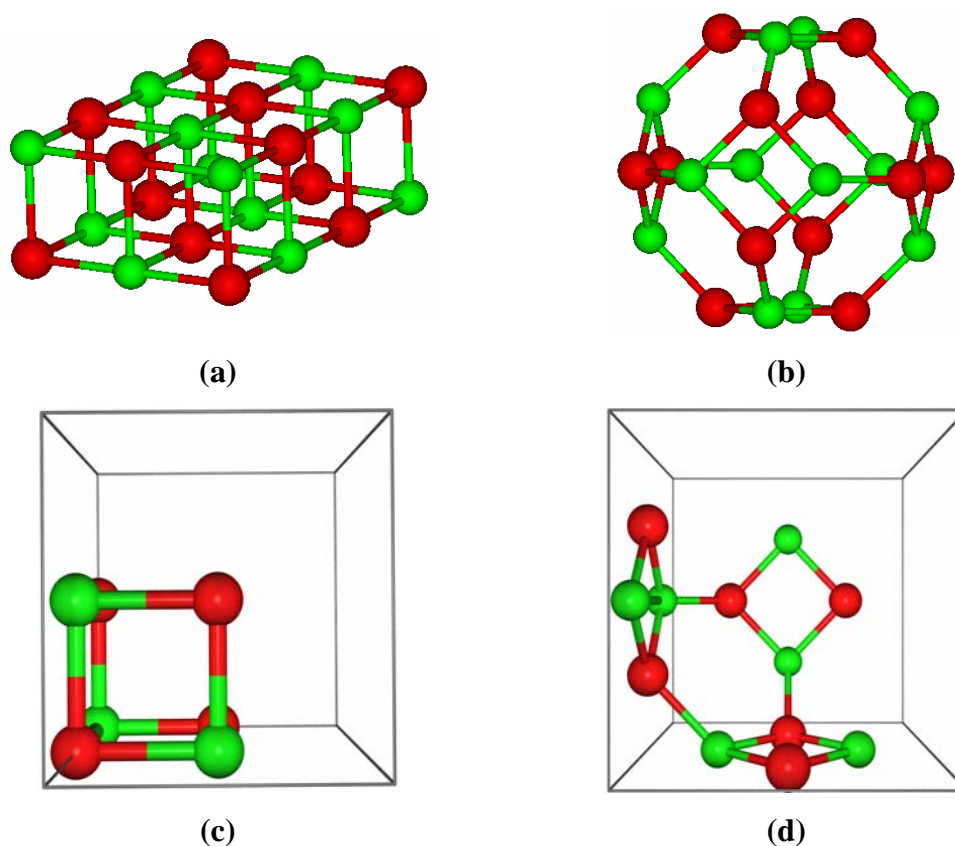


**Figure 8** The illustrative of models used in the calculation: (a) a 3x2x1 slab cluster, (b) a cage cluster, (c) a unit cell of rock salt phase and (d) a unit cell of sodalite phase.

In order to attain a balanced description of both discrete and extended systems, it is convenient to use the same computational approach and, whenever possible, the same basis set. This can be achieved by first choosing a reliable exchange-correlation functional which can be used in molecular and periodic calculations and, secondly, by expanding the total electron density in a plane wave basis using an appropriate unit cell. The choice of a plane wave basis is computationally efficient and for which the quality can be conveniently and generally defined by a single parameter. The Perdew-Wang (PW91) form (Perdew *et al.*, 1992; White and Bird, 1994) of the generalized gradient approach (GGA), as implemented in the VASP code (Kresse and Furthmüller, 1996; Kresse and Furthmüller, 1996; Kresse and Hafner, 1993) has been chosen for the exchange correlation potential. This is known to provide reliable

system energies for many bulk materials and represents a good balance between accuracy and computational efficiency.

For the discrete systems, using a plane wave basis set requires simply placing the clusters inside a large enough box which is periodically repeated. The box chosen has to be large enough so that the distance between repeated  $(MX)_{12}$  clusters is sufficient to make inter-cluster interactions negligible (in our calculations  $>1$  nm). For the bulk systems it is also necessary to carry out appropriate integrations in reciprocal space, this is accomplished by using a Monkhorst-Pack grid of special  $k$ -points (7x7x7) for the rock-salt structure and (3x3x3) for the low density phases).

In the present work, the plane waves were included with kinetic energies up to 415 eV in the basis set. The effect of core electrons on the valence density was taken into account through the plane augmented wave method (Blöchl, 1994) as implemented by Kresse and Joubert (Kresse and Joubert, 1999). For all MX bulk structures density functional optimizations of atomic positions and cell shape were carried out for different volumes of the unit cell and the volume versus energy data fitted using the Birch-Murnaghan EOS (Birch, 1947) in order to obtain the minimum energy and optimum cell parameters.

## RESULTS AND DISCUSSIONS

### Carbonyl-ene reaction on Na-FAU

This part has been separated into 3 sections. In the first section, the structure of the Na-exchanged faujasite zeolite is discussed, then the existence of encapsulated formaldehyde in Na-exchanged faujasite zeolite in order to study the reactivity of this species is also considered, and finally the study of their interactions with propylene using the ONIOM model is demonstrated.

#### Na-exchanged faujasite zeolite

Recent studies (Bobuatong and Limtrakul, 2003; Choomwattana *et al.*, 2008; Jansang *et al.*, 2006; 2008; Kasuriya *et al.*, 2003; Maihom *et al.*, 2008; Namuangruk *et al.*, 2004; Roggero *et al.*, 2001; Tang and Fan, 2000; Torrent *et al.*, 2002) have shown that the van der Waals interactions between hydrocarbons, or aromatic adsorbates and a zeolitic framework contribute significantly to the structural and energetic features of the adsorption–desorption processes in zeolites. Thus, hybrid methods such as QM/MM and ONIOM should be able (and necessary) to describe these interactions with the zeolite framework reasonably well. In this case, the ONIOM method was employed to investigate the structure of the formaldehyde in Na-exchanged faujasite system and its reaction with propylene molecule.

The structure of Na-exchanged faujasite is shown in Figure 6 and the optimized geometrical parameters are documented in Table 6. The charge of Na in the zeolite supercage is calculated (NPA) to be 0.93. It is compensated by the surrounding oxygen atoms in the 6T ring inside the supercage.

**Table 6** Optimized geometric parameters of reactants, transition state and products of the carbonyl-ene reaction between formaldehyde and propylene on Na-

faujasite using the ONIOM2 (B3LYP/6-31G(d,p):UFF) method. (bond lengths are in pm and bond angles are in degrees)

<b>Parameters</b>	<b>Naked Na-FAU</b>	<b>Formaldehyde adsorption</b>	<b>Coadsorption complex</b>	<b>Transition state</b>	<b>Product</b>
<i>Distances</i>					
C–O	–	122.2	122.2	131.7	144.2
C1–C2	–	–	133.6	141.1	150.7
C2–C3	–	–	150.3	141.8	133.7
C3–H	–	–	109.8	122.0	270.6
C–C1	–	–	348.5	180.9	153.5
O–H	–	–	408.7	152.6	97.2
Na–O	–	233.1	232.1	225.4	231.1
Na–Al	315.9	315.1	319.7	323.4	314.6
Na–O1	216.5	220.5	221.6	216.3	221.0
Na–O2	262.7	263.7	272.1	276.5	263.1
Al–O1	180.0	179.1	179.1	180.0	179.1
Al–O2	174.9	174.7	174.3	174.9	174.6
Si1–O1	160.7	161.1	161.1	160.7	160.7
Si2–O2	158.1	158.5	158.4	158.1	158.4
<i>Angles</i>					
O1–Al–O2	97.6	99.4	100.1	97.6	99.5
Si1–O1–Al	138.1	138.3	138.2	138.1	138.7
Si2–O2–Al	146.3	145.5	145.3	146.3	145.3

### Na-exchanged faujasite encapsulated formaldehyde

The structure of formaldehyde as stabilized in the zeolite framework is displayed in Figure 9a. Selected optimized geometrical parameters are documented in Table 6. Formaldehyde first interacts with the active Lewis acid site by its lone electron pair. This leads only to small changes in the zeolite structure (less than 2 pm and 2° for changes in bond distances and bond angles, respectively). The carbon–oxygen bond of formaldehyde is elongated from 120.7 to 122.2 pm. The distance between the formaldehyde oxygen and the Na atom of zeolite is 233.1 pm and the corresponding adsorption energy for the HCHO/Na-faujasite complex is 18.4 kcal/mol due to the interaction between the hydrogen atoms of formaldehyde and the oxygen atoms of the framework. The C–O...Na(I) angle is 124.1°, in contrast to the model system without faujasite (2) where it is linear and the sodium cation in HCHO/Na(I) interacts directly with the oxygen atom of formaldehyde (Figure 10a). In Na(I) system, the C–O bond of formaldehyde bond is elongated from 120.7 to 122.0 pm due to the presence of Na(I) ion and the Na–O distance is 216.1 pm. The binding energy of this complex is –26.5 kcal/mol. A test calculation at QCISD(T) level of theory with 6-311G(d,p) basis set gave –25.8 kcal/mol (Remko, 1997). The results of the NPA analysis (Table 7) correspond to the trends in the binding energies: The NPA-charge of Na(I) ion in HCHO/Na(I) system is +0.98 while it is +0.91 in the zeolite system and the charges of the oxygen atom of formaldehyde are –0.67 (Na(I) system) and –0.61 (bare system), respectively.

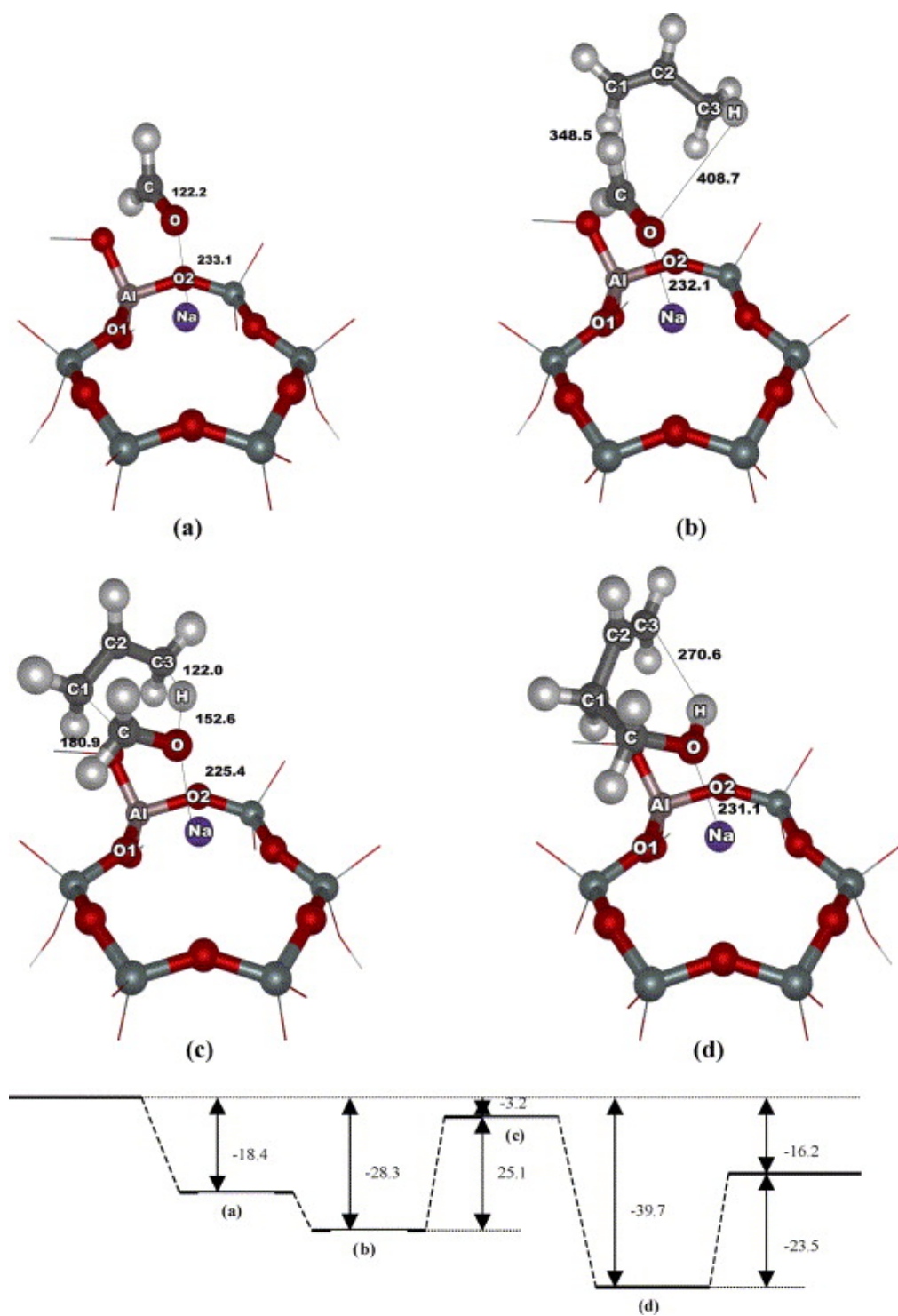


**Figure 9** Structures and calculated energy profile (kcal/mol) of the carbonyl-ene reaction in Na-faujasite: (a) HCHO/Na-faujasite complex, (b) coadsorption complex, (c) transition state structure, and (d) product structure.

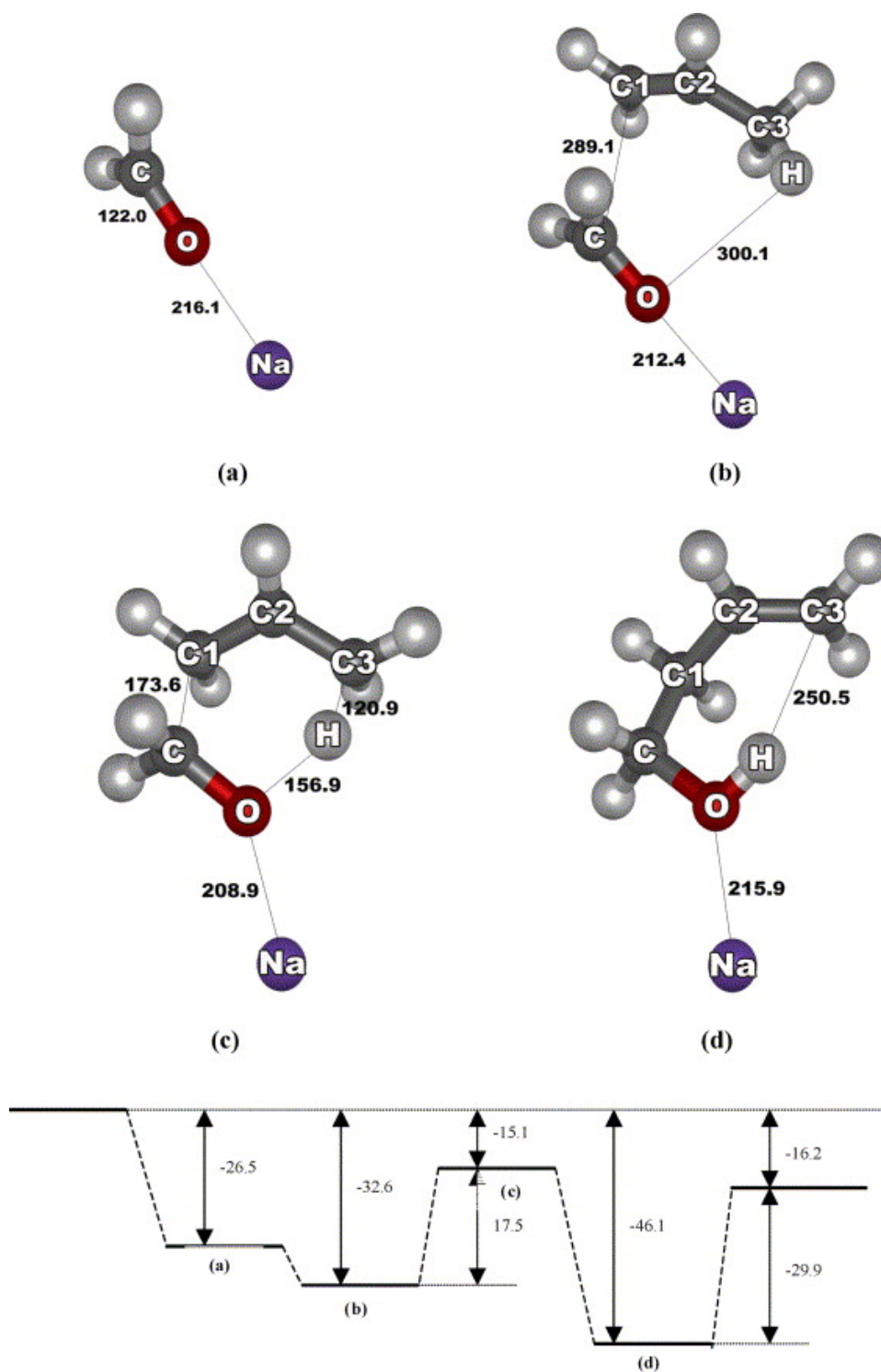


**Figure 10** Structures and calculated energy profile (kcal/mol) of the carbonyl-ene reaction in Na(I) ion system: (a) HCHO/Na(I) complex, (b) coadsorption complex, (c) transition state structure, and (d) product structure.

**Table 7** Atomic charge distribution calculated from the natural population analysis. (NPA)

Parameters	Isolated molecule	Na-FAU zeolite system				Naked Na(I) ion system				Bare system		
		Form. ads. <sup>a</sup>	Coads. <sup>b</sup>	TS	Product	Form. ads. <sup>a</sup>	Coads. <sup>b</sup>	TS	Product	Coads. <sup>b</sup>	TS	Product
q(Na)	1.00	0.91	0.91	0.91	0.92	0.98	0.98	0.96	0.97	–	–	–
q(O)	–0.49	–0.61	–0.61	–0.79	–0.84	–0.67	–0.71	–0.88	–0.89	–0.51	–0.66	–0.76
q(C)	0.23	0.26	0.26	–0.02	–0.10	0.31	0.27	–0.04	–0.10	0.22	–0.02	–0.09
q(C1)	–0.44	–	–0.47	–0.55	–0.54	–	–0.45	–0.55	–0.53	–0.46	–0.53	–0.53
q(C2)	–0.22	–	–0.22	0.01	–0.25	–	–0.20	0.07	–0.25	–0.21	–0.09	–0.23
q(C3)	–0.73	–	–0.72	–0.74	–0.44	–	–0.72	–0.75	–0.43	–0.72	–0.73	–0.45
q(H)	0.25	–	0.24	0.36	0.51	–	0.23	0.35	0.52	0.26	0.38	0.48

<sup>a</sup> Formaldehyde adsorption<sup>b</sup> Coadsorption complex of formaldehyde and propylene

### Carbonyl-ene reaction between Na-exchanged faujasite encapsulated formaldehyde and propylene

The carbonyl-ene reaction can proceed via concerted interaction in the coadsorption complex of the Na-exchanged faujasite zeolite-encapsulated formaldehyde with the propylene without any intermediate. The reaction steps can be written as follow:



Step 1 is the adsorption of formaldehyde onto the Lewis acid site of the zeolite. Step 2 involves the interaction of the encapsulated formaldehyde with propylene, resulting in the adsorbed product (3-buten-1-ol), which is desorbed in the final Step 3. The selected optimized geometrical parameters of the carbonyl-ene reaction between propylene and encapsulated formaldehyde in Na-faujasite zeolite are listed in Table 6 and the same parameters of the naked Na(I) ion system and the system without sodium cation are given in Table 8. Under typical reaction temperatures, formaldehyde readily adsorbs on the Lewis acid site via lone pair electron interaction, but propylene interacts only weakly with the Lewis acid site via a  $\pi$ -interaction.

**Table 8** Optimized geometric parameters of the carbonyl-ene reaction between formaldehyde and propylene for the bare system and the naked Na(I) ion system from B3LYP/6-31G(d,p) calculations. (bond lengths are in pm and bond angles are in degrees)

Parameters	Isolated molecule	Naked Na(I) ion system				Bare system		
		Form. ads. <sup>a</sup>	Coads. <sup>b</sup>	TS	Product	Coads. <sup>b</sup>	TS	Product
<i>Distances</i>								
C–O	120.7	122.0	122.7	133.7	147.7	120.9	128.7	141.6
C1–C2	133.3	–	134.1	142.0	150.7	133.5	139.5	150.4
C2–C3	151.2	–	149.8	141.9	133.8	150.0	141.6	133.5
C3–H	109.6	–	110.0	120.9	250.5	109.7	128.2	280.5
C–C1	–	–	289.1	173.6	153.3	340.5	197.0	154.0
O–H	–	–	300.1	157.0	97.7	266.6	135.4	96.9
Na–O	–	216.1	212.4	208.9	215.9	–	–	–

<sup>a</sup> Formaldehyde adsorption

<sup>b</sup> Coadsorption complex of formaldehyde and propylene

The entire reaction energy profile is presented in Figure 9. The reaction is initiated by coadsorption of propylene on the encapsulated formaldehyde at the active site of the zeolite (Figure 9b). The propylene molecule diffuses over the adsorbed formaldehyde on the Na-exchanged faujasite zeolite with a coadsorption energy of 28.3 kcal/mol. In the naked Na(I) ion system, the coadsorption of the propylene stabilizes the adsorption complex by  $-32.6$  kcal/mol. The distance between formaldehyde carbon (C) and propylene carbon (C1) is calculated to be 289.1 pm. Due to the larger electrostatic field generated by the naked Na(I) ion, this distance is shorter than in Na-faujasite system (348.5 pm). In the bare system, however, the coadsorption energy (Figure 11a) is only  $-3.3$  kcal/mol and the distance between the formaldehyde carbon (C) and the carbon atom of propylene (C1) is 340.5 pm. This indicates that the carbon of the formaldehyde carbonyl group is more electrophilic if it is coordinated to the naked Na(I) ion than in the bare system.

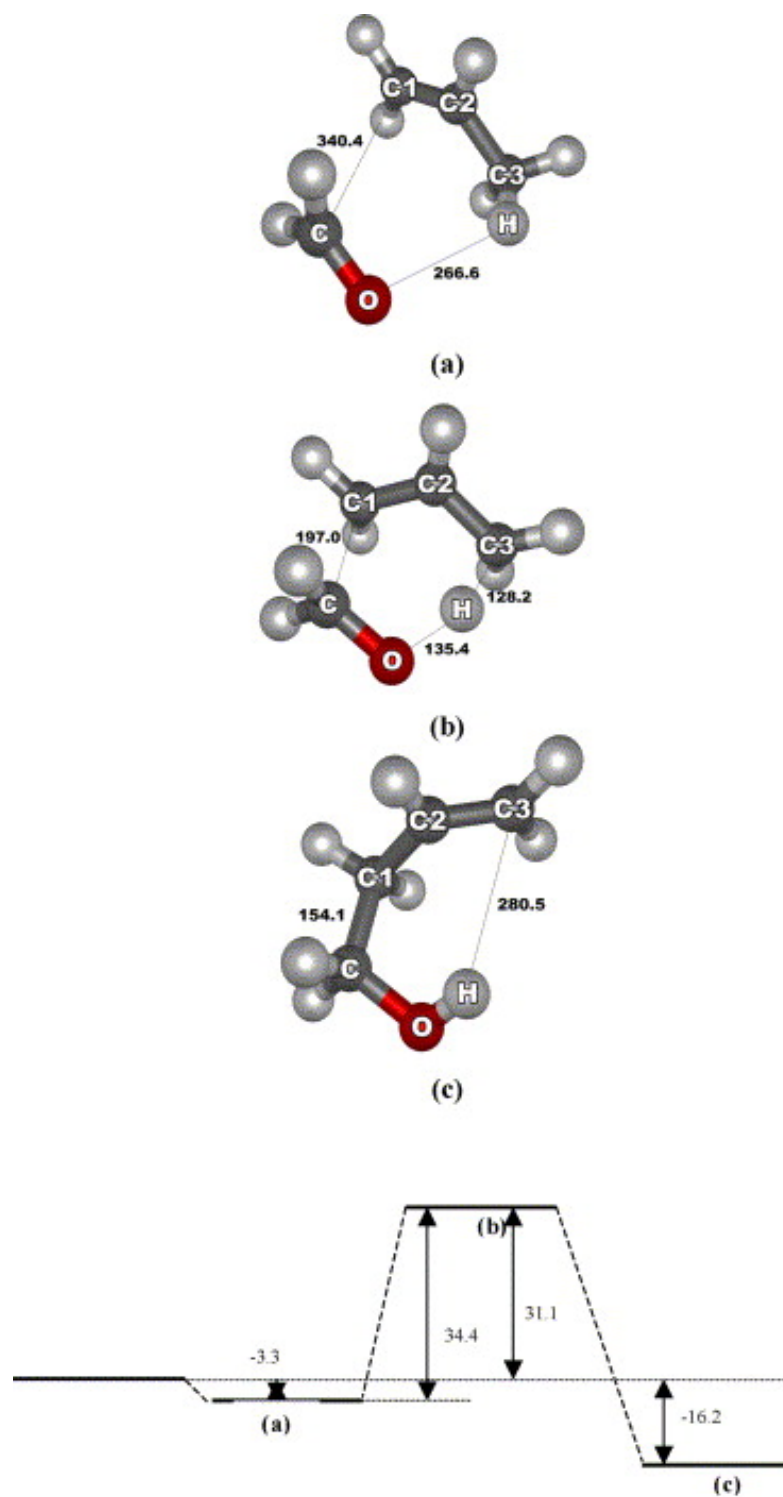


**Figure 11** Structures and calculated energy profile (kcal/mol) of the carbonyl-ene reaction in the bare system: (a) coadsorption complex, (b) transition state structure, and (c) product structure.

The carbonyl-ene reaction involves concerted bond forming between the carbon atom of formaldehyde (C) and the propylene carbon (C1) and the breaking of a propylene proton (H) giving the proton to the formaldehyde oxygen (O). At the transition state (Figure 9c), the complex exhibits one imaginary frequency. The corresponding vibrational motion shows the concerted mechanism of the carbonyl-ene reaction: A carbon-carbon bond is formed between encapsulated formaldehyde and propylene and, simultaneously, a propylene proton leaves toward the formaldehyde oxygen atom. At the transition state, the Lewis acid slightly changes its position on the zeolite (by less than 5 pm, concerning changes in distance between Na and atoms Al, O1, O2 of the zeolite framework) and the distance between formaldehyde oxygen and Na atom becomes 225.4 pm. The propylene C3-H bond distance is lengthened from 109.8 to 122.0 pm and the distance between propylene proton (H) and formaldehyde oxygen (O) becomes 152.6 pm while the C-O double bond of the formaldehyde is elongated from 122.2 to 131.7 pm, whereas the distance between the propylene carbon (C1) and formaldehyde carbon (C) becomes 180.9 pm. The C1-C2 and C2-C3 bond length change from 133.6 and 150.3 to 141.1 and 141.8 pm, respectively. The activation energy for this transition state is 25.8 kcal/mol. In the case of naked Na(I) ion system (2), the distance between the propylene carbon (C1) and formaldehyde carbon (C) is contracted from 289.3 to 173.6 pm and the C1-C2 and C2-C3 bond lengths change from 134.1 and 149.82 to 142.0 and 141.9 pm, respectively, whereas the propylene C3-H bond distance is significantly lengthened from 110.0 to 120.9 pm and the distance between propylene proton (H) and formaldehyde oxygen (O) becomes 157.0 pm while the C-O double bond of formaldehyde is elongated from 122.7 to 133.7 pm. The activation energy is 17.5 kcal/mol and the apparent activation energy is -15.1 kcal/mol. These results demonstrated that the electrostatic contribution from the naked Na(I) ion stabilizes the transition state structure. Therefore, the activation energy barrier of this system is lower than in the Na-faujasite system.

In the bare system (Figure 11b), the C-C1 bond distance is contracted from 340.5 to 197.0 pm. The distance between propylene proton (H) is elongated from 109.7 to 128.2 pm while the distance between formaldehyde oxygen (O) and

propylene proton (H) becomes 135.4 pm. The length of the C1–C2 and C2–C3 bonds in propylene change from 134.11 and 149.82 to 142.04 and 141.87 pm, respectively. The reaction coordinate (the normal mode that has one imaginary frequency) indicates again the concerted mechanism of carbonyl-ene reaction. The activation energy is 34.4 kcal/mol and the reaction energy is  $-16.2$  kcal/mol. This can be compared to the experimental data reported by Benson et al. (Benson and O'Neal, 1970), which are 26.4 and  $-13.5$  kcal/mol, respectively.

The product state (Figure 9d), in which the C–C1 bond is formed involves a proton transfer from the carbon atom of propylene to the formaldehyde oxygen. The adsorbed 3-buten-1-ol product is subsequently desorbed endothermically, requiring 23.5 kcal/mol. In the naked Na(I) ion system, the product oxygen interacts with the Na(I) ion via electrostatic interaction to the lone electron pair of the product. With a binding energy of  $-29.9$  kcal/mol, the interaction of Na(I) with the product is stronger than that in the case of formaldehyde. The distances between the product oxygen and the Na(I) ion in both systems (the naked Na(I) ion system and the Na-faujasite system) are calculated to be 215.9 and 231.1 pm, respectively. The NPA analysis shows that the charge of Na(I) in system is larger (+0.97) than in the Na-faujasite system (+0.92).

The energy diagrams of the three systems are put into one plot in Figure 12. For the Na-exchanged faujasite zeolite, the activation energy of the reaction is 25.1 kcal/mol, which lies between the activation barriers of the bare system (34.4 kcal/mol) and the naked Na(I) system (17.5 kcal/mol). This is due to the electrostatic field generated by the Na(I) ion and the destabilizing role of the oxygen atom in the zeolite lattice surrounding the cation. These results indicate that alkaline-exchanged faujasite zeolite can be used as a catalyst in carbonyl-ene reaction and that they stabilize all species in the carbonyl-ene reaction systems. Na-exchanged faujasite especially can preserve formaldehyde in a monomeric form and can also activate it sufficiently to promote its reaction with various olefins.

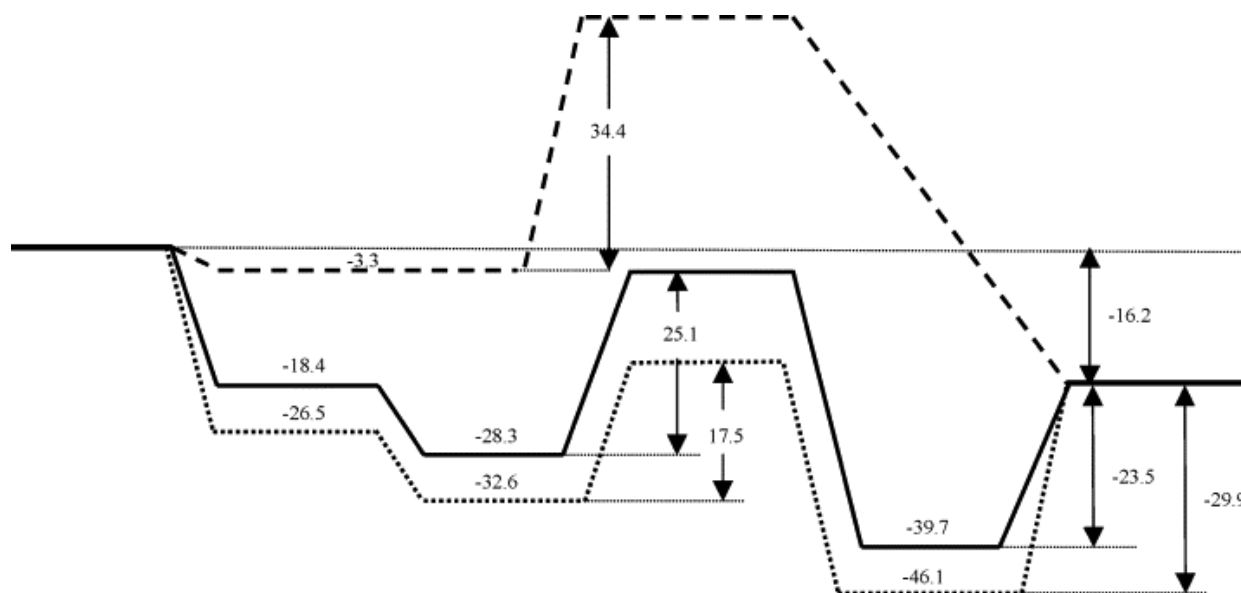


**Figure 12** Calculated energetic profiles (kcal/mol) for the carbonyl-ene reaction between HCHO and CH<sub>3</sub>CH=CH<sub>2</sub> in the Na-faujasite zeolite system (solid line), the naked Na(I) system (dotted line), and the bare system (dashed line).

### Adsorption and diffusion of *n*-hexane in nanoporous silicate MCM-41

This part is the study of adsorption and diffusion of *n*-hexane in siliceous MCM-41 using molecular dynamic simulations. The models of siliceous MCM-41 with different pore sizes in the simulations denoted as models A (3 Si tetrahedral atoms), B (4 Si tetrahedral atoms), C (5 Si tetrahedral atoms) and D (6 Si tetrahedral atoms) are again showed in Figure 13. We divide this chapter into five parts. In the first two parts, the effects of pore size and loading on the adsorption energy are discussed. Next, the diffusivity of *n*-hexane in siliceous MCM-41 is described by term of self-diffusion coefficients. Then the model structures we used are calculated to determine the vibrational spectra and finally the radial distribution functions of sorbate molecules are analyzed.

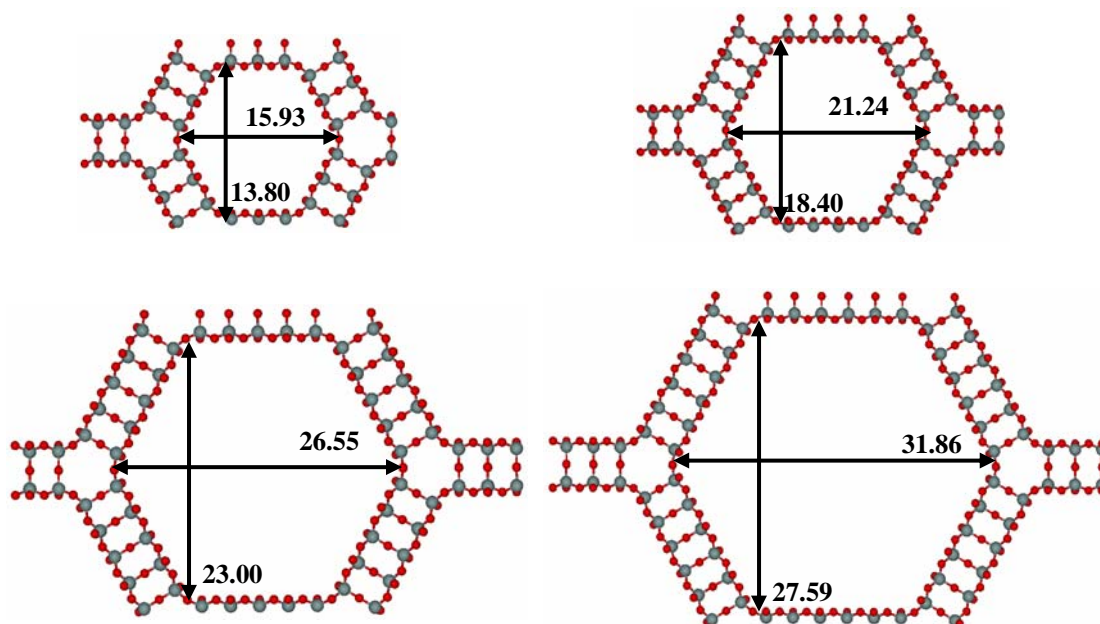


**Figure 13** Structures and sizes of siliceous MCM-41 models A to D.

### Adsorption energy - effect of the pore size

The adsorption energy of *n*-hexane in siliceous MCM-41 has contributions from both the interaction between *n*-hexane molecules with the terminal silanol groups of the siliceous MCM-41 framework and the interaction between *n*-hexane molecules. Although the silanol groups are not explicitly modeled in these simulations, their interactions are included implicitly via our fitting procedure, as mentioned in the models and methods section. The adsorption energies at various loadings of *n*-hexane are given in Table 9. From the experimental data, the adsorption energies of *n*-hexane at low loading in siliceous MCM-41 are in the range -8.85 to -9.33 kcal/mol (Janchen *et al.*, 1998; Trens *et al.*, 2005; Zhao *et al.*, 2001). The framework D has a pore size close to this experimental one. With this model and one molecule of *n*-hexane per supercell we obtain adsorption energy of -9.1 kcal/mol. Since the potential parameters are tuned to reproduce this energy, this is not surprising, but it indicates that the intermolecular potential parameters give reasonable results.

**Table 9** Adsorption energies and self-diffusion coefficients at different *n*-hexane loadings in siliceous MCM-41 model A to D.

<b>Model A</b>			<b>Model B</b>			<b>Model C</b>			<b>Model D</b>		
<b>loading(s)</b>	<b><math>\Delta E_{Ads}</math></b>	<b><math>D</math></b>									
1	-13.7	-	1	-12.2	-	1	-11.1	-	1	-9.1	-
8	-14.1	$5.7 \times 10^{-5}$	8	-12.5	$1.5 \times 10^{-4}$	8	-11.2	$3.6 \times 10^{-4}$	8	-9.1	$5.1 \times 10^{-4}$
16	-14.7	$3.0 \times 10^{-5}$	16	-13.1	$9.7 \times 10^{-5}$	16	-11.4	$1.5 \times 10^{-4}$	16	-9.3	$2.8 \times 10^{-4}$
32	-17.0	$4.8 \times 10^{-6}$	32	-13.4	$5.9 \times 10^{-5}$	32	-11.5	$1.0 \times 10^{-4}$	32	-9.4	$1.4 \times 10^{-4}$
			64	-15.4	$8.4 \times 10^{-6}$	64	-12.0	$4.8 \times 10^{-5}$	64	-9.8	$9.9 \times 10^{-5}$
									128	-10.9	$3.3 \times 10^{-6}$
34	-17.3	$3.8 \times 10^{-6}$	70	-16.0	$4.3 \times 10^{-6}$	118	-14.7	$2.0 \times 10^{-6}$	176	-13.1	$4.3 \times 10^{-6}$

$\Delta E_{Ads}$  in kcal/mol and  $D$  in  $\text{cm}^2/\text{s}$

Loadings in guest molecules per simulation box

For smaller pores, higher adsorption energies are obtained from the simulations (see Table 9). A comparison of the energy components reveals that differences in the van der Waals interactions are mainly due to the effect of the pore size. They dominate the adsorption of the nonpolar molecules and are also responsible for the confinement effects.

### **Adsorption energy - effect of the loading**

In a series of simulations, the studied the effect of the loadings for the four frameworks were discussed. As mentioned above, the number of sorbate molecules,  $N$ , was varied from 1 to a value corresponding to the liquid density. Except for the case of one molecule per supercell, each of the pores in the supercell was loaded with an equal number of guest molecules. It was found that, due to the attractive interaction between *n*-hexane molecules, the adsorption energy for the highest loading is 3-4 kcal/mol larger than the one for single-molecule loading. The calculated energies are again given in Table 9.

### **Self-diffusion of *n*-hexane**

The study of diffusivity of organic molecules confined in porous materials is of importance in the petroleum industry and in the field of catalysis. From the MD trajectories we calculated the diffusion coefficients via the mean square displacement (MSD) using the Einstein relation:

$$\langle X^2(t) \rangle = 6Dt + B \quad (25)$$

$X^2(t)$  is the mean square displacement of the molecular center of mass at time  $t$ ,  $D$  is the self-diffusion coefficient, and  $B$  is the thermal factor arising from vibrational motions. The MSD of the centers of mass of the *n*-hexane molecules as a function of the time are shown in Figure 14 for different loadings. The self-diffusion coefficients were obtained from the slopes when the curves have become linear and

are given in Table 9. It can be seen that at higher loadings the self-diffusion coefficients are smaller than at lower ones. This is because of the steric hindrance between *n*-hexane molecules. Due to the confinement effect, for the same loading, self-diffusion also decreases with decreasing pore size. This is in accord with the work of Qiao and Bhatia (Qiao and Bhatia, 2005), where the diffusion of decane in siliceous MCM-41 was studied by the zero Length Column method and it was found that the diffusivity increases slowly with increasing pore size. This work's find here that the variation of the diffusivity for the different pore sizes, at the same temperature, is small. The diffusion coefficients increase slightly with increasing pore diameter. This means also that the self-diffusion coefficients decrease with increasing adsorption energy. The calculated self-diffusion coefficients are in good agreement with values measured for the diffusion of *n*-hexane in dehydroxylated MCM-41 with pore diameters from 32 to 38 Å. These were determined by pulsed field gradient NMR experiments and lie in the range of  $1.61 - 1.98 \times 10^{-5} \text{ cm}^2/\text{s}$  (Courivaud *et al.*, 2000a; Courivaud *et al.*, 2000b).

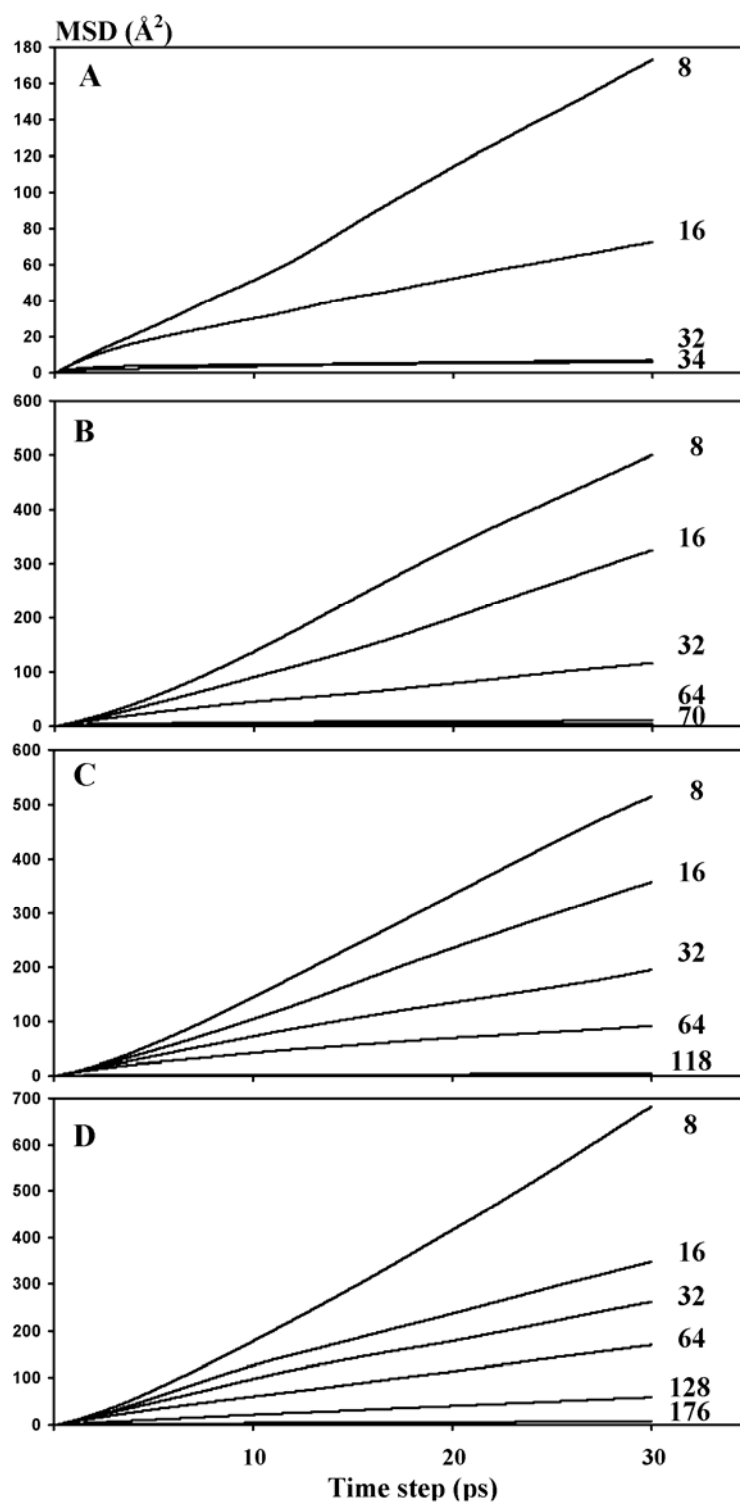


**Figure 14** Mean square displacements (MSDs) of the centers of mass of the *n*-hexane molecules in the models A to D. The loading is indicated on the right hand side of the curves.

## Vibrational spectra

The infrared spectra of the MCM-41 were calculated by Fourier transform of the autocorrelation function of the total dipole moment of the system, computed from the partial charges of the models. The spectra obtained from our trajectories are shown in Figure 15 for the frequency range between 300 and 1200  $\text{cm}^{-1}$ . The peaks at about 480 and 620  $\text{cm}^{-1}$  are due to the Si-O-Si bending modes. The symmetric stretching modes of the Si-O bonds appear at approximately 770  $\text{cm}^{-1}$  and the strong peak around 1100  $\text{cm}^{-1}$  is due to the asymmetric stretching of these bonds. The calculated spectra agree with the experimental infrared spectrum of Al-MCM-41 (Wang *et al.*, 2004).

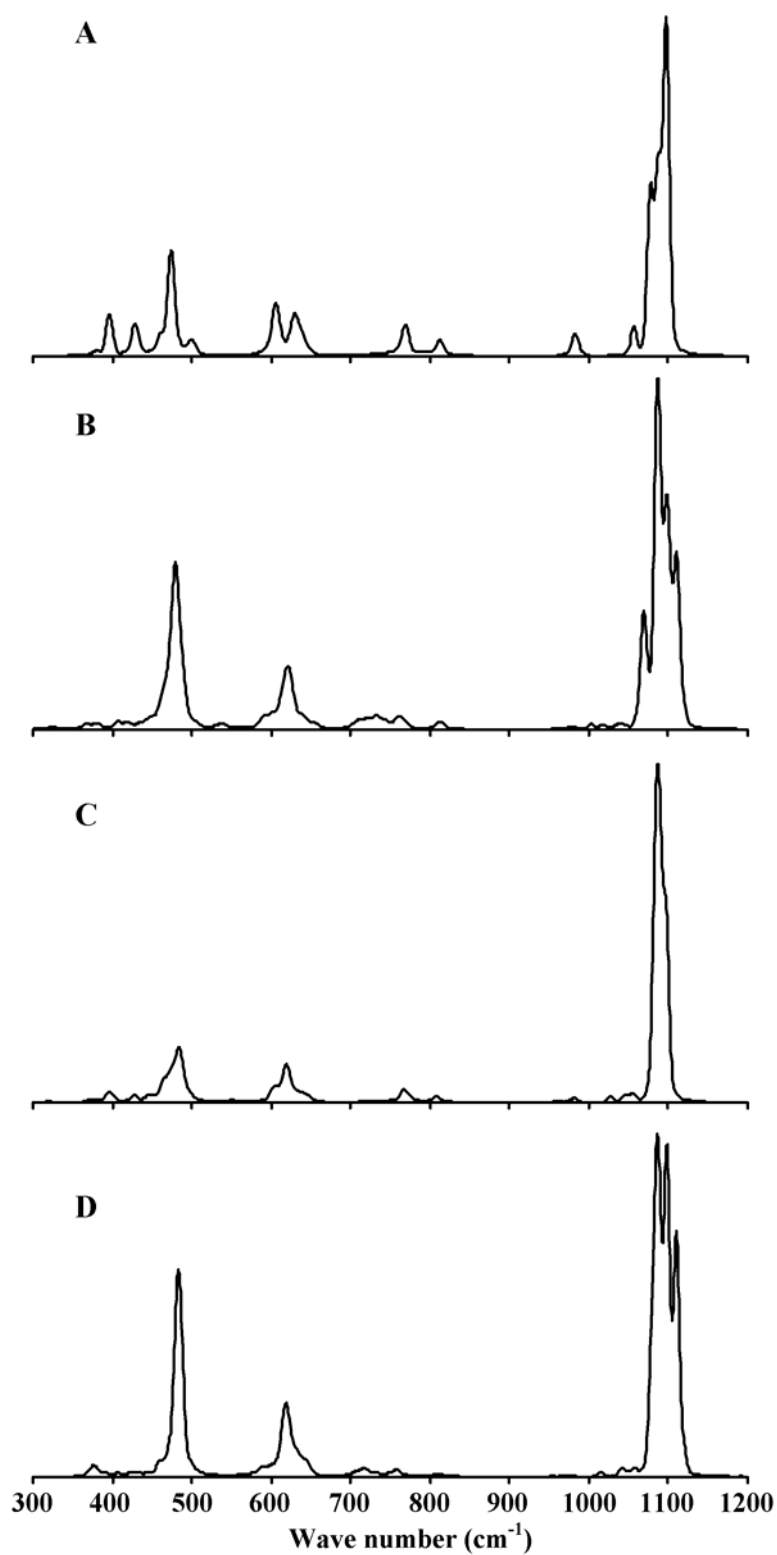


**Figure 15** Simulated infrared spectra of silanol-free siliceous-MCM-41 of the models A to D from the normalized correlation functions.

### Radial distribution functions

The structural characteristics of sorbate molecules in the pores of siliceous MCM-41 were analyzed by means of the radial distribution functions (RDFs),  $g_{AB}(r)$ . Such pair correlation functions describe how, on average, the atoms or molecules in a system are radially packed around each other:

$$g_{AB}(r) = \left\langle \frac{dn_{AB}}{dr} \frac{1}{4\pi r^2 \rho_B N_A} \right\rangle \quad (26)$$

$N_A$  indicates the number of  $A$  centers,  $\rho_B$  is the macroscopic density of  $B$  centers, and  $n_{AB}$  is the number of  $AB$  pairs.

Figure 16 shows the RDFs of the centers of mass of the  $n$ -hexane molecules for various models of siliceous MCM-41 with different  $n$ -hexane loadings up to the saturation limit. The first peak of the RDF is at 6.3-6.6 Å for  $n$ -hexane in siliceous MCM-41 and 6.7 Å for liquid  $n$ -hexane (Figure 17). These values agree well with the distances between the liquid  $n$ -hexane molecules obtained from experimental ultrasonic velocity experiments (6.502 Å) (Kalidoss and Ravi, 2002). Finally, one can see from Figure 17 that the positions of the peak maxima are shifted to larger distances with increasing pore sizes. The distribution functions between the centers of the pore and the centers of mass of the  $n$ -hexane molecules along the  $z$ -axis were also calculated (Figure 18). It can be seen that at small loadings the  $n$ -hexane molecules prefer an orientation parallel to the pore surface and close to it. The space between the pore surface and the  $n$ -hexane molecules is due to the short-range repulsion between the oxygen atoms on the siliceous MCM-41 framework and the adsorbed molecule.

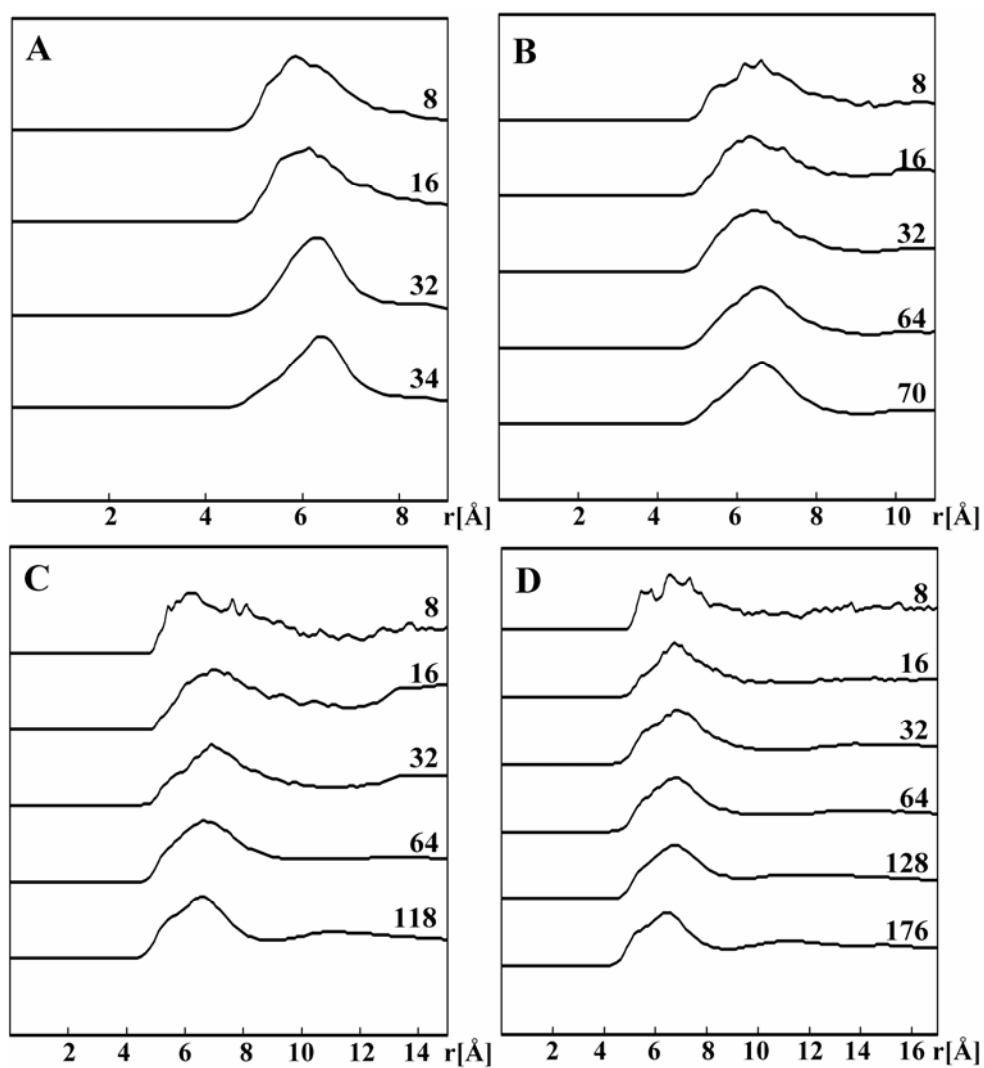


**Figure 16** Centers of mass radial distribution functions of the *n*-hexane molecules in models A to D for different loadings. (the curves are shifted vertically by 5 units)

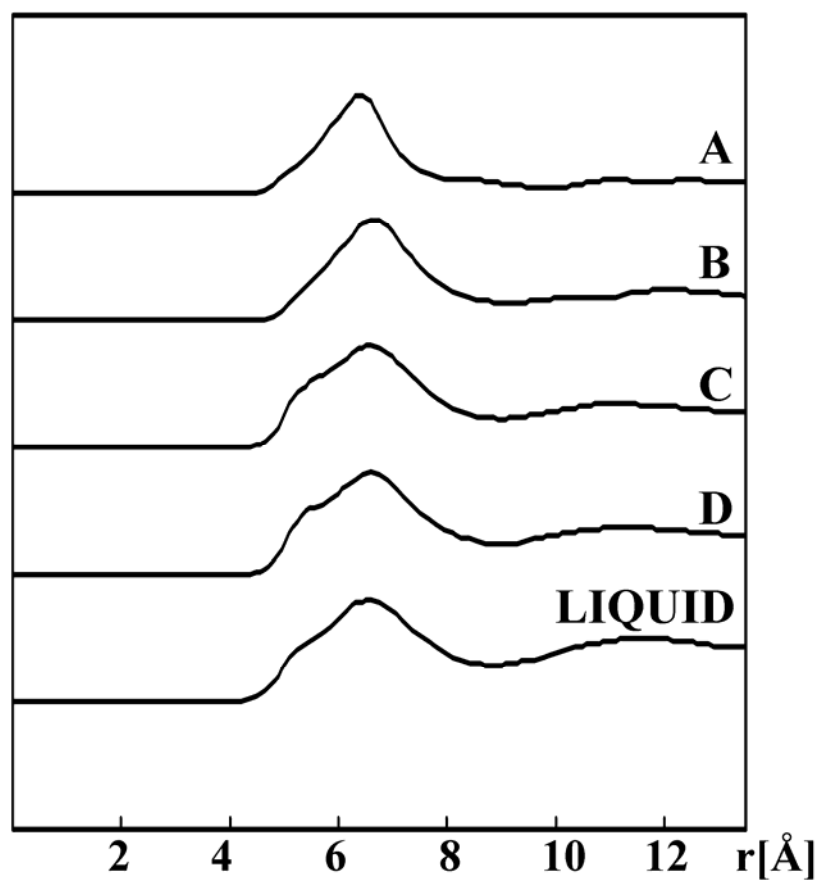


**Figure 17** Centers of mass radial distribution of the *n*-hexane molecules at saturation in the four systems and in the liquid phase. (the curves are shifted vertically by 5 units)

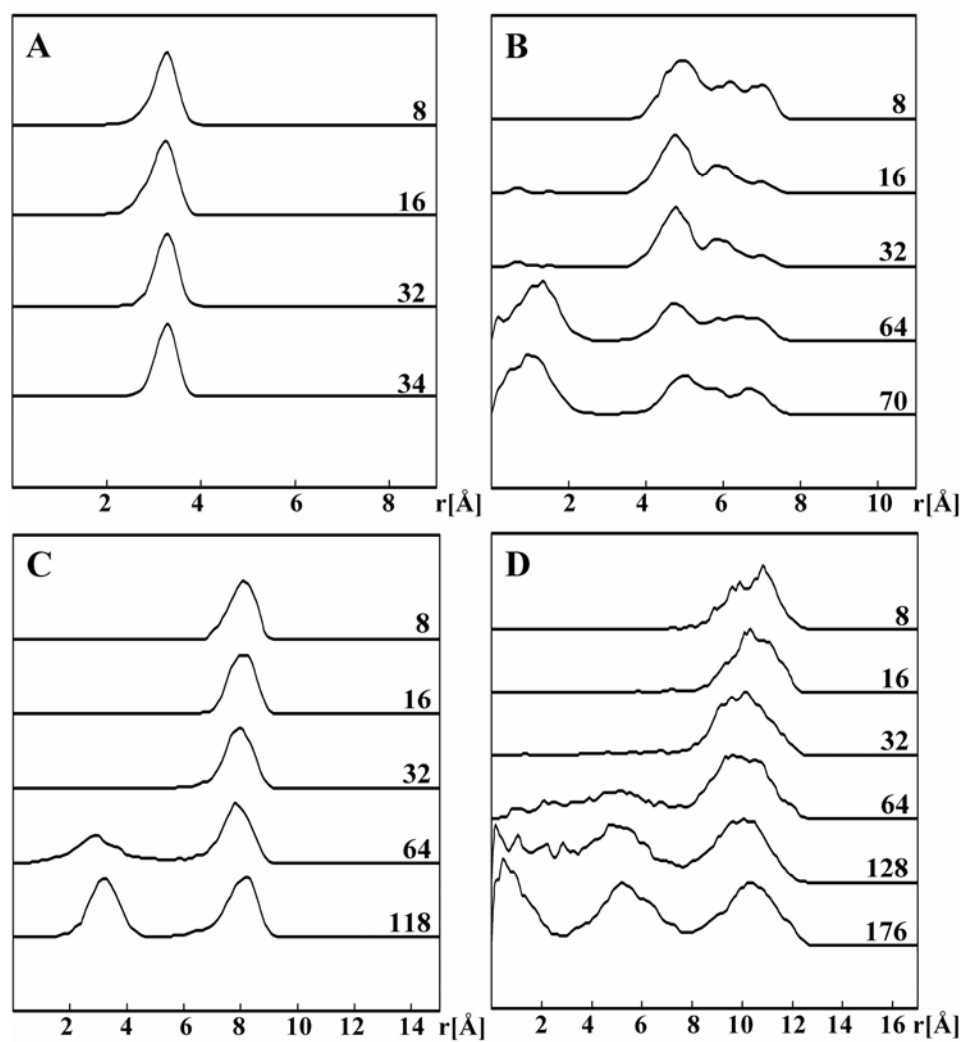


**Figure 18** Distribution functions of the distances between the centers of the pore and the centers of mass of *n*-hexane molecules in models A to D. (the curves are shifted vertically by 5 units)

For framework A, the loading has no effect on the position of the first maximum of this RDF because the *n*-hexane molecules form rings inside the MCM-41 pores and for larger loadings, more of the pore surface is covered by these rings. For framework B with a wider pore channel it is found that at low loadings (8 and 16 molecules per supercell), all molecules are also located near the pore surface. There are 2 peak maxima that indicate that the *n*-hexane molecules are arranged into 2 configurations. An inspection of the coordinates from the trajectories shows that some *n*-hexane molecules lie parallel to the pore surface and some are randomly oriented near the pore surface. For loadings of 32 molecules per supercell and above, a second peak, with a distance of about 4-6 Å from the first one appears. The *n*-hexane molecules that make up this peak lie either parallel or perpendicular to the wall surface. Again, inspection of the trajectories shows that these molecules do not form a layer but a more chainlike structure along the pore. The results have not been observed an exchange of molecules between these two regions. The second peak increases further with increasing loading, indicating that the added *n*-hexane molecules find space in the center of the pore. For the next bigger framework C, all *n*-hexane molecules are lying parallel to the pore surface at loadings of 8, 16 and 32 molecules per supercell. At a loading of 64 molecules per supercell a second peak appears. It can be seen from the trajectories that the added *n*-hexane molecules now form a second layer inside the pore, which is accommodating them up to saturation. Also no exchange took place here between the two layers. In the biggest framework D we see both peaks: at 64 molecules per supercell, the second layer of *n*-hexane molecules starts to build up, the pores are now wide enough that at a loading of 128 molecules per supercell the excess *n*-hexane molecules are also accommodated at the center of the pore. Therefore, at the saturation limit, *n*-hexane molecules form two concentric layers with other *n*-hexane molecules located in the center of the cylindrical pore. In this framework the three regions are not separated, which indicates that there is an exchange between the three domains. In summary, orientations and positions of *n*-hexane molecules in siliceous MCM-41 are different from the ones in the liquid phase, in which orientations are random (Kioupis and Maginn, 1999).

The RDFs between the centers of the pore and the centers of mass of *n*-hexane in siliceous MCM-41 at saturated loadings are shown in Figure 19, superimposed on the atomic coordinates. The features discussed above can be seen clearly. A snapshot from one time step of the simulation is displayed in Figure 20 and further illustrates the effects of the pore size and the formation of *n*-hexane layers.

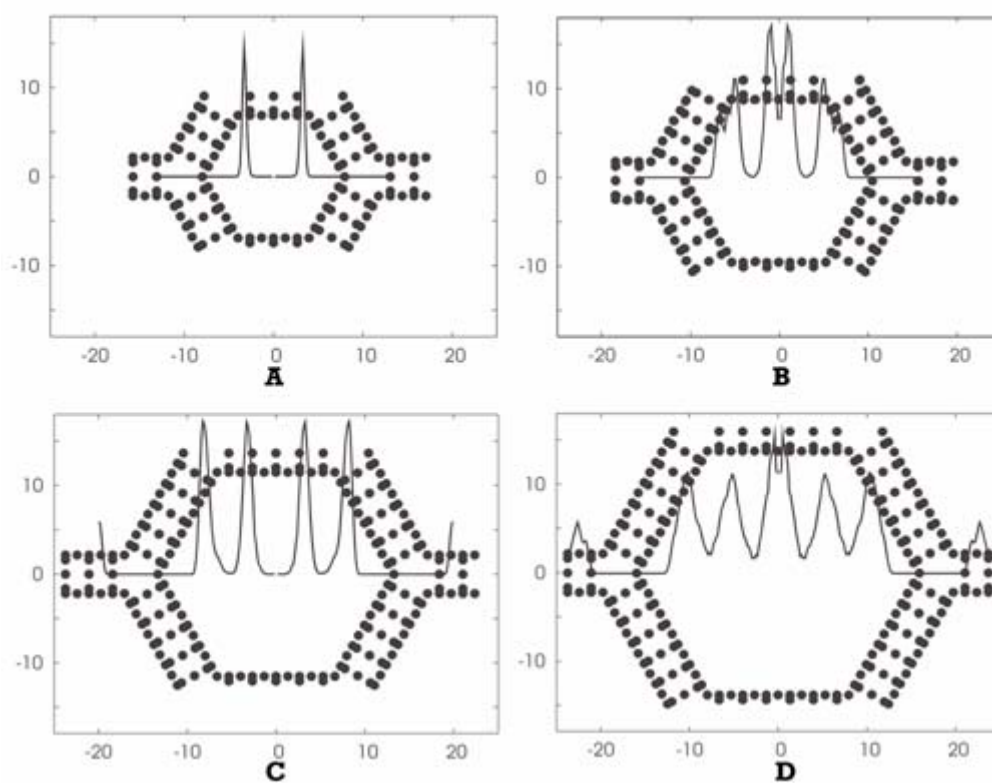


**Figure 19** Distribution functions at saturation (Figure 6) superimposed on the structures of models A to D.

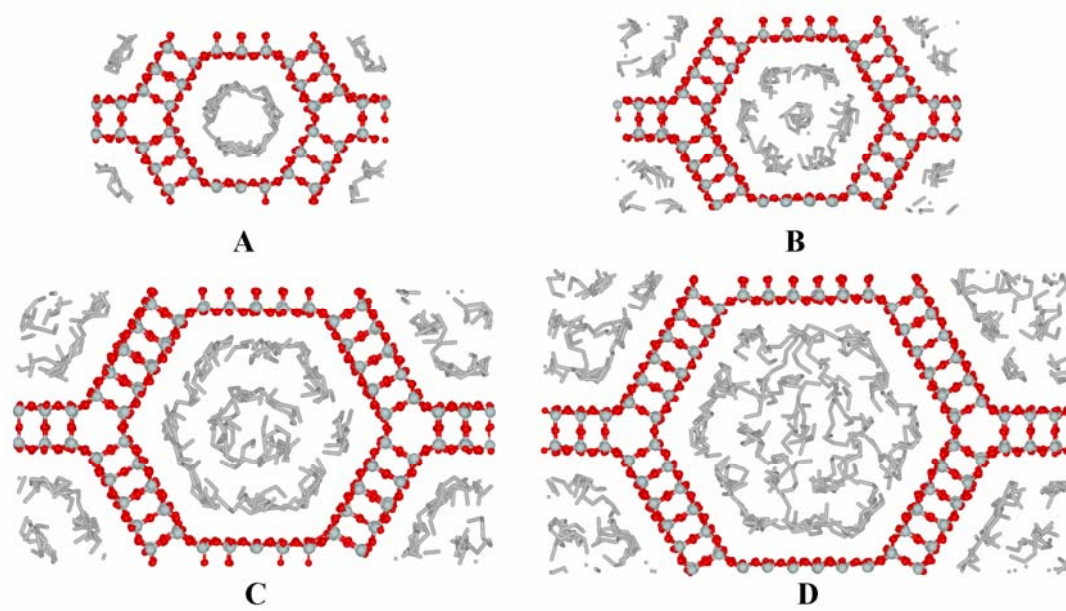


**Figure 20** Snapshots from the simulation showing a typical distribution of *n*-hexane molecules at saturated loading in models A to D.

## Theoretical bottom-up Study Stable Nanoporous Alkali Halide Polymorphs

In this part, density functional calculations are utilized to study the relative stability of  $(MX)_{12}$  ( $M$  = alkali metal,  $X$ = halogen) cluster isomers with respect to that of two polymorphs which could be considered as formed from the aggregation of these clusters. The comparison between the energetic trends of the cluster isomers (slab and cage clusters) and their respective bulk phases (the rock-salt ( $rs$ - $MX$ ), and SOD- $MX$  phases) are studied, throughout the full range of materials which reveals an interesting link between nanoscale and macroscopic stabilities.

### Relative stability of $(MX)_{12}$ alkali halide clusters

The main purpose of the present work is to analyze the possibility of low density bulk phases of alkali halides and their relative stability with respect to the face-centered cubic ( $fcc$ ) structure, which is almost always the most stable alkali halide polymorph. It should be noted that for the most voluminous cation ( $Cs^+$ ) with the three larger anions:  $Cl^-$ ,  $Br^-$ ,  $I^-$ , the body centered cubic ( $bcc$ ) phase is the ground state bulk phase. With relation to the bottom-up approach, however, the clusters  $(CsCl)_{12}$ ,  $(CsBr)_{12}$ ,  $(CsI)_{12}$ , all appear to be most stable as  $3 \times 2 \times 1$   $fcc$  slab isomers. For each alkali halide, we performed the energy minimization of the slab and the cage as  $(MX)_{12}$  isomers. In all cases the  $(MX)_{12}$  tube was never found to be the most stable isomer, with the lowest energy isomers being either the cage or slab only. Results for the relative energy of the slabs and cages for the series ( $M$ = Li-Cs and  $X$ =F-I) are reported in Table 10.

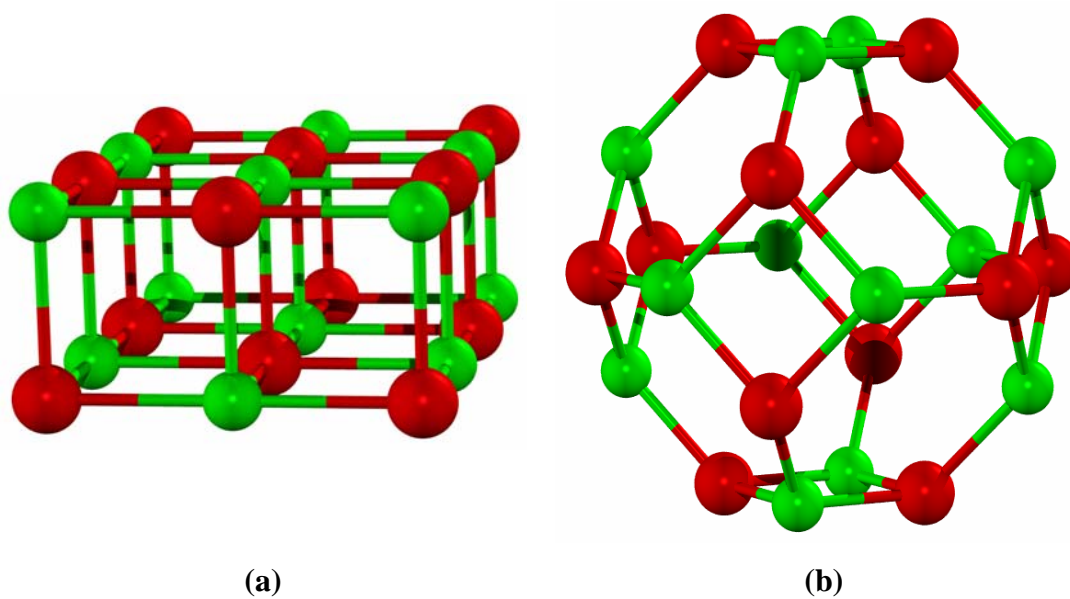
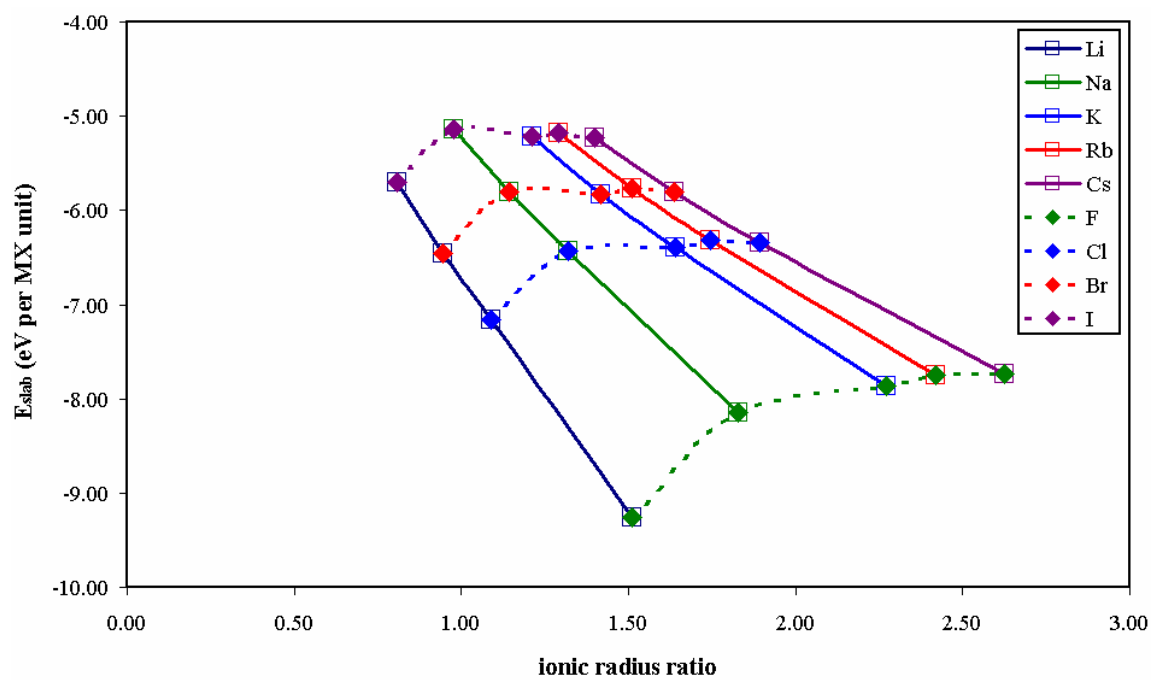


**Figure 21** Schematic representation of the structure of (a) the slab and (b) the cage structures of the  $(MX)_{12}$  alkali halide clusters. Red spheres represent the anion whereas the green spheres represent the cations.

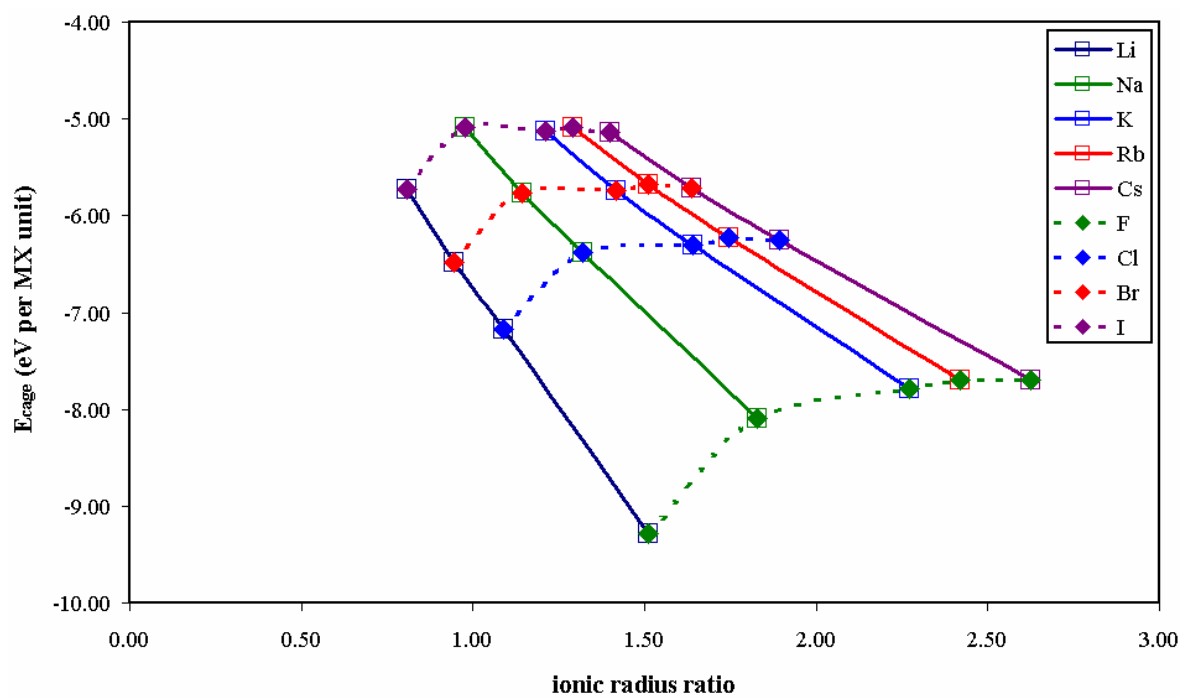
**Table 10** Total energy per MX unit (in eV) of the slab and cage isomers of the  $(MX)_{12}$  alkali halide clusters.

<b>MX</b>	<b>Slab</b>	<b>Cage</b>
LiF	-9.25	-9.28
LiCl	-7.16	-7.18
LiBr	-6.46	-6.48
LiI	-5.70	-5.72
NaF	-8.14	-8.09
NaCl	-6.43	-6.38
NaBr	-5.81	-5.76
NaI	-5.14	-5.09
KF	-7.86	-7.79
KCl	-6.39	-6.31
KBr	-5.83	-5.74
KI	-5.22	-5.13
RbF	-7.76	-7.69
RbCl	-6.32	-6.23
RbBr	-5.77	-5.68
RbI	-5.17	-5.08
CsF	-7.73	-7.69
CsCl	-6.34	-6.25
CsBr	-5.80	-5.72
CsI	-5.22	-5.13

For both slab and cage isomers, it is found that with the same alkali cation ( $M^+$ ) and varying the halide anion ( $X^-$ ), the optimized energies increase with decreasing ionic radius ratios and follow an almost linear correlation (see Figure 22a, 21b). Correspondingly, the most stable clusters are those of  $(MF)_{12}$  type while the least stable are those of  $(MI)_{12}$  composition. In contrast along each series:  $(MF)_{12}$ ,  $(MCl)_{12}$ ,  $(MBr)_{12}$ ,  $(MI)_{12}$  (i.e. fixing the halide type and varying the alkali metal ion) we see that, although for  $(MCl)_{12}$ ,  $(MBr)_{12}$ ,  $(MI)_{12}$  the energy varies very little, for  $(MF)_{12}$  both the cages and slabs clusters are significantly more stabilised (see figure 22a, 22b). Of all alkali halides, LiF is found to provide the most stable clusters for both slab and cage structures with energies (per MX unit) of -9.25 eV/LiF and -9.28 eV/LiF, respectively. This result together with the energetic preference of LiF for the cage isomer over the slab already provides an indication that LiF can be regarded as a special case.



(a)



(b)

**Figure 22** Total energy MX halides clusters (a) slab and (b) cage as a function of the cation and anion.

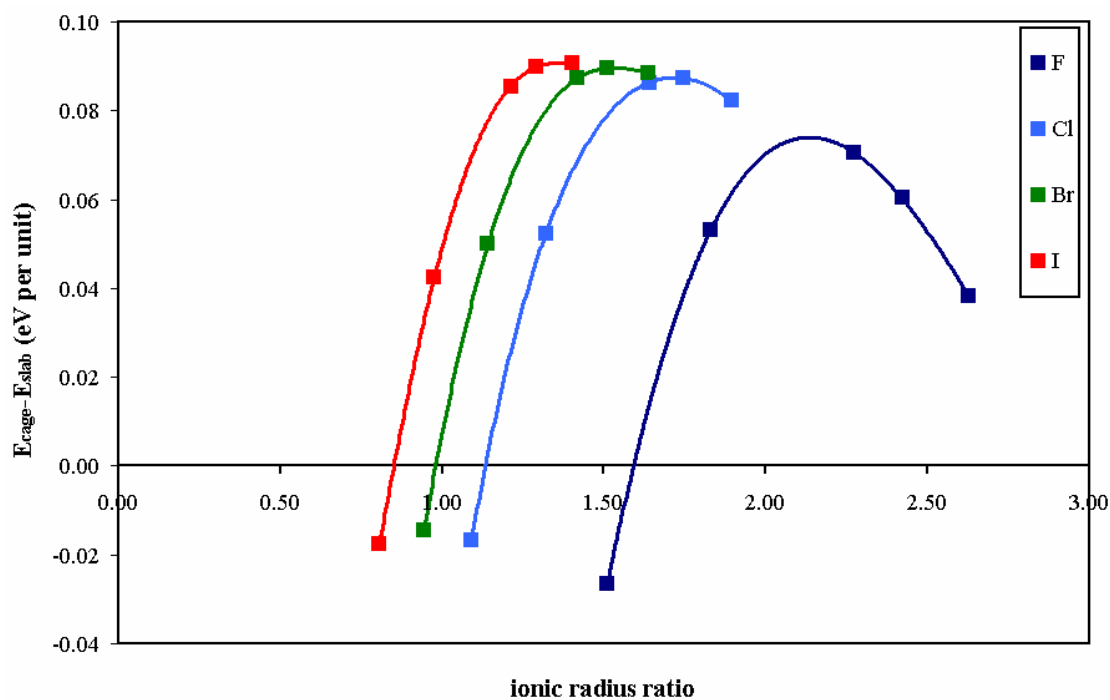


**Figure 23** Energy difference per MX unit (in eV) between the slab and cage structure of the  $(MX)_{12}$  alkali halide clusters as a function of the cation/anion ionic radius. Each set of points relates to a series maintaining the halide and varying the alkali metal. (the lines are parabolic fits to the points to guide the eye)

In Figure 23 we report the energy difference (per MX unit) between the cage and the slab isomers for each fixed halide (X) while varying the metal type (M). In most cases we find that the cubic slab isomer is most stable. This concurs with previous work showing an energetic preference for cubic isomers in alkali halide clusters containing Na, K and Rb using a variety of theoretical methods including global optimization techniques with empirical potentials, ab initio Hartree-Fock and Møller-Plesset second order perturbation theory (Aguado *et al.*, 1997; Croteau and Patey, 2006; Doye and Wales, 1999; Lintuluoto, 2002; Ochsenfeld and Ahlrichs, 1994). These works also often found evidence for competition between the energetic stability between rock-salt and tubular hexagonal ring-based structures with the latter being generally favoured for Li-containing clusters. On idealized ionic packing grounds, it has been argued that the relative energy between the dense cubic and more open tubular structures may be rationalized by consideration of the ratio between the cationic and anionic radii (Aguado *et al.*, 1997; Wootton and Harrowell, 2004). Essentially, the argument is analogous to that used in the approximate rationalization of dense crystal structures (Pettifer, 1995) whereby increasing differences in cation and anion radii lead to the inability of the ions to pack as closely as when of similar size, thus leading to more open crystal structures. In clusters, as there are no restrictions on periodicity, we may expect that the respective ions when of significantly different size may use non-bulklike means to optimize their ionic packing. The reported emergence of non-bulklike tubular low energy cluster isomers is in line with such packing rationalizations for the LiX series due to the very small relative size of the  $\text{Li}^+$  ion with respect to all the halide ions. However, as noted above, for the size  $(\text{MX})_{12}$  the tubular clusters are not the ground state isomer for any alkali halide and further that for the  $(\text{LiX})_{12}$  series the more open SOD cage structure appears to be the optimal manner to “pack”  $\text{Li}^+$  and  $\text{X}^-$  ions. Specifically, the cage structure is found to be more stable than both the slab and tubular cluster isomers for all the  $(\text{LiX})_{12}$  clusters, and for the remainder the cubic slab is the  $(\text{MX})_{12}$  ground state. For  $(\text{LiX})_{12}$  the energy differences between cubic slab and cage isomers are rather small, lying in the range between -0.015 to -0.026 eV/LiX. However, from Li to Cs for a fixed halide, the energy difference between the two clusters increases steeply with increasing cation versus anion ionic radius ratio up to a maximum

difference. For I the energy difference increase stops at this maximum point for CsI, whereas for Br, Cl and F containing clusters the energy difference maximizes and then starts to reduce again. For the F series this effect is most notable with an energy difference between slab and cage reaching a maximum for KF and then decreasing significantly for RbF and CsF. Again, one could rationalize this trend with respect to ionic radii ratios, where by at the maximum of the curves in Figure 23 have ions of a very similar size (and thus a preference for close-packed slabs) and away from these maxima such packing is not possible and the more open cage isomer becomes progressively more competitive.

Although ionic packing arguments are useful, they are only general idealized guides to structural preferences that omit many details (e.g. polarization induced ion distortions) of the bonding in real systems which are governed by the electronic structure. To gain some more detailed insight into the bonding and ionic polarization in the cage and slab clusters, these cluster have been analyzed the changes in the electronic structure upon increasing the formal cation/anion radii ratio using the Electron Localization Function (ELF). The ELF was introduced by (Becke and Edgecombe, 1990) and has been extensively used to analyse chemical bonding in a range of systems (Krokidis *et al.*, 1997; Savin *et al.*, 1997; Silvi and Savin, 1994). The topological analysis of the ELF allows one to distinguish between core and valence electrons and, in this last case, between lone pairs, covalent bonding between two atoms or multi-centered bonds. In the case of the alkali halide clusters, the chemical bonding is highly ionic as is reflected in the ELF maps shown in Figure 24. When going from the extremes of LiF to CsF, through KF as an intermediate case, one can note interesting changes in the ELF maps for both cage and slab cluster isomers. The ELF maps for the slab cluster show rather spherical ELF basins, which are indicative of a highly ionic character, although with an increasing and noticeable deformation when going from LiF to CsF. For the cage clusters the situation is rather different, the ELF maps are largely deformed from the symmetric spherical shape, even for LiF. This is a clear indication that, in spite of similar stability, the chemical bond between the alkali metal and the halogen atom in the slab and cage clusters is different, with a more marked polarized and directional character in the cage

structures. The directional character of the chemical bond in the cage structures is enhanced when going from LiF to CsF. This may seem counterintuitive since one would expect the ionic character to increase along the series in response to the decrease of the alkali atom ionization potential. However, one must also consider the different polarization of the electron density upon increasing the cation atomic radius. In any case, the ELF maps in Figure 24 show that a clear difference exists in the chemical bond of alkali halides in the slab and cage structures.

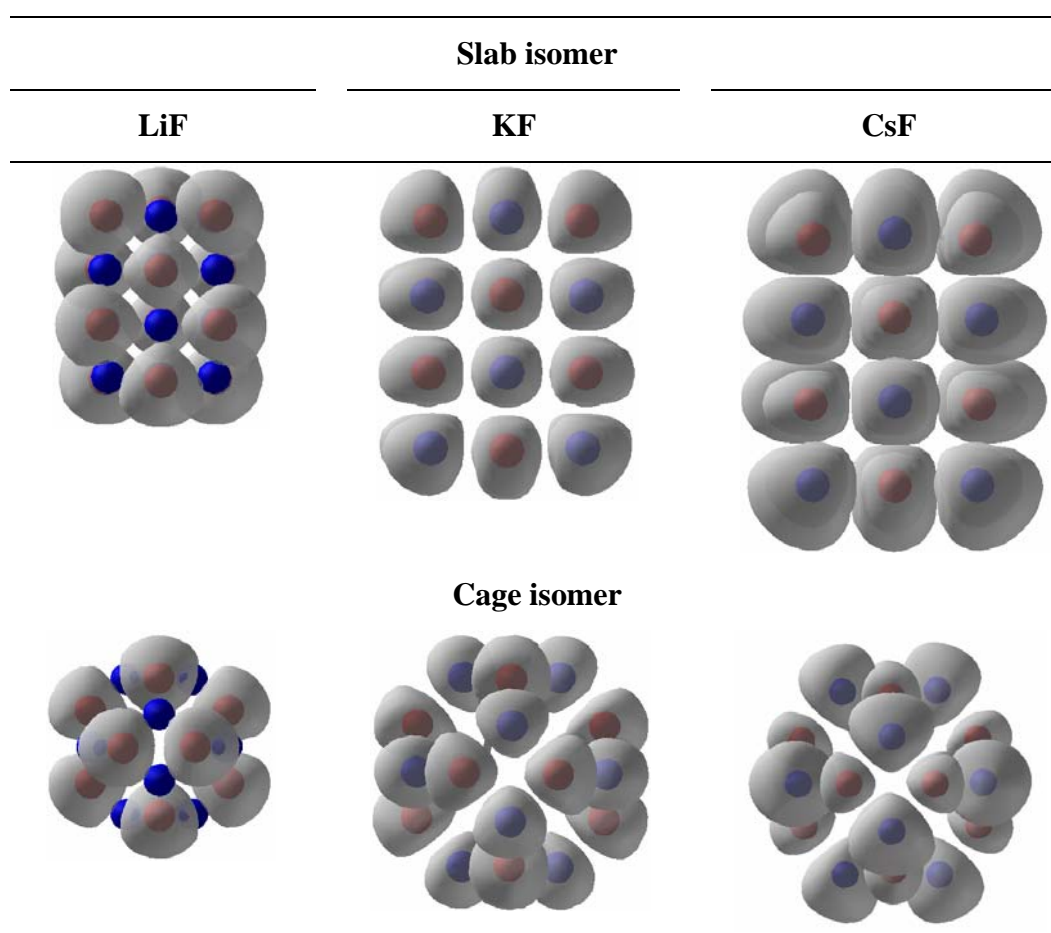


**Figure 24** ELF maps for the slab and cage structures of LiF, KF and CsF. The red centres indicate the positions of the alkali metal ions and the blue centres the halide ion positions. The grey area shows the form of the ELF basins for each ion.

### **Rock-salt structure versus sodalite structure of bulk alkali halides**

Two types of bulk structures have been considered for the alkali halide materials (rs-MX and SOD-MX) both of which may be thought of as arising from assembling slab or cage clusters respectively (see Figure 25a and 25b). SOD-MX may be constructed by assembling twelve  $(MX)_{12}$  cages by square links in such a way that an equivalent empty cage is created in the center of the resulting unit (see Figure 25c). In the SOD-MX phase, the alkali and halide atoms are four-coordinated centers whereas in the rs-MX, the usual octahedral coordination is maintained. It should be noted that the sodalite (SOD) is not the only low density phase which may be generated by using  $(MX)_{12}$  clusters as building blocks. Other low density nanoporous zeolite-like structures (e.g. LTA or faujasite) can also be constructed from this simple building block, however, these are generally less stable than SOD and have not been further considered. Total energy per MX unit (in eV) and volume per MX unit (in  $\text{\AA}^3$ ) of the rock salt and sodalite phases of the alkali halide polymorphs are documented in Table 11.

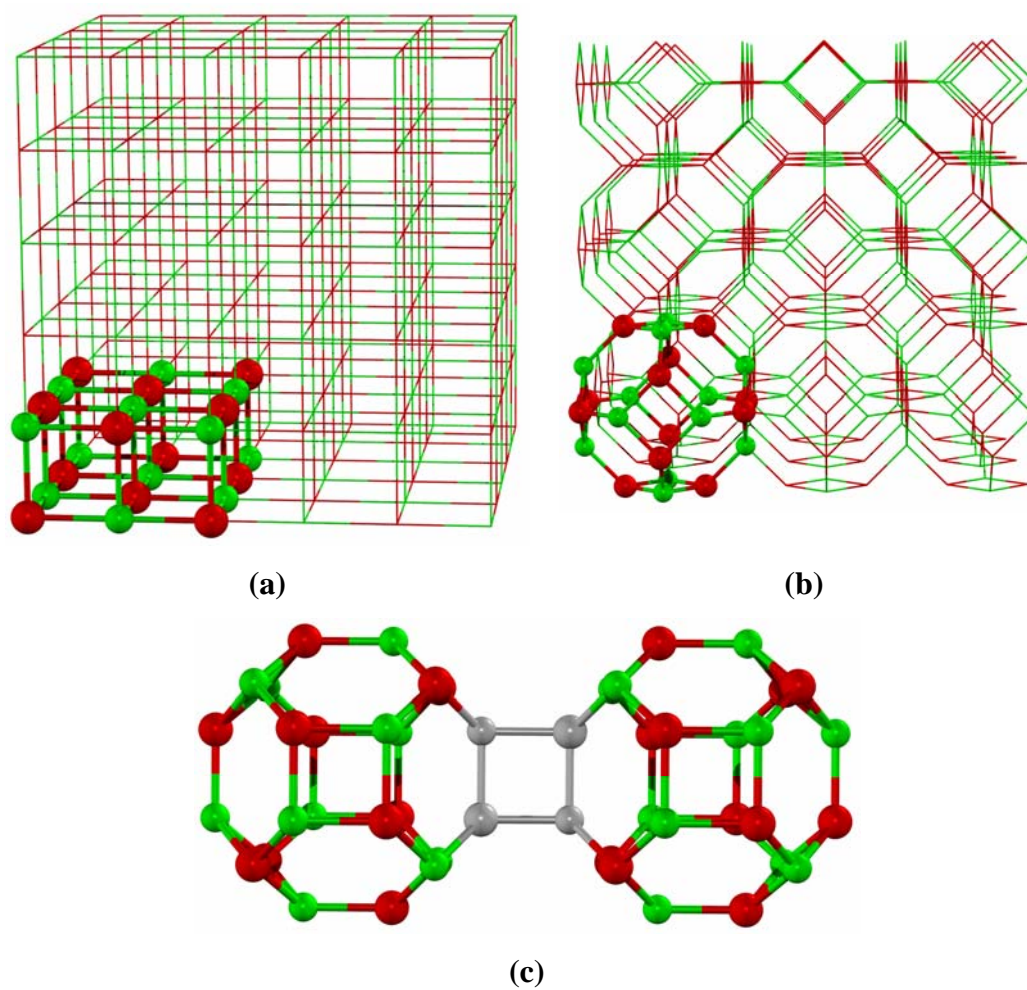
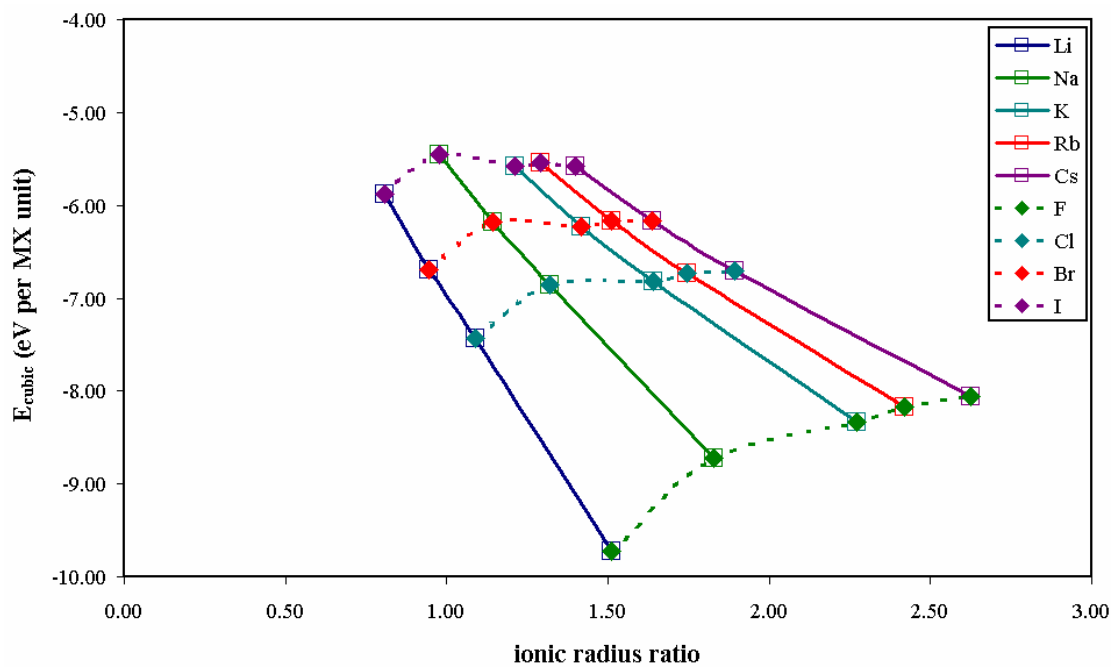


**Figure 25** rs-MX and SOD-MX structures of alkali halides viewed as the assembling of (a)  $(MX)_{12}$  slabs, (b)  $(MX)_{12}$  cage clusters, and (c) the assembling of  $(MX)_{12}$  cages. Red spheres represent the anion whereas the green spheres represent the cations.

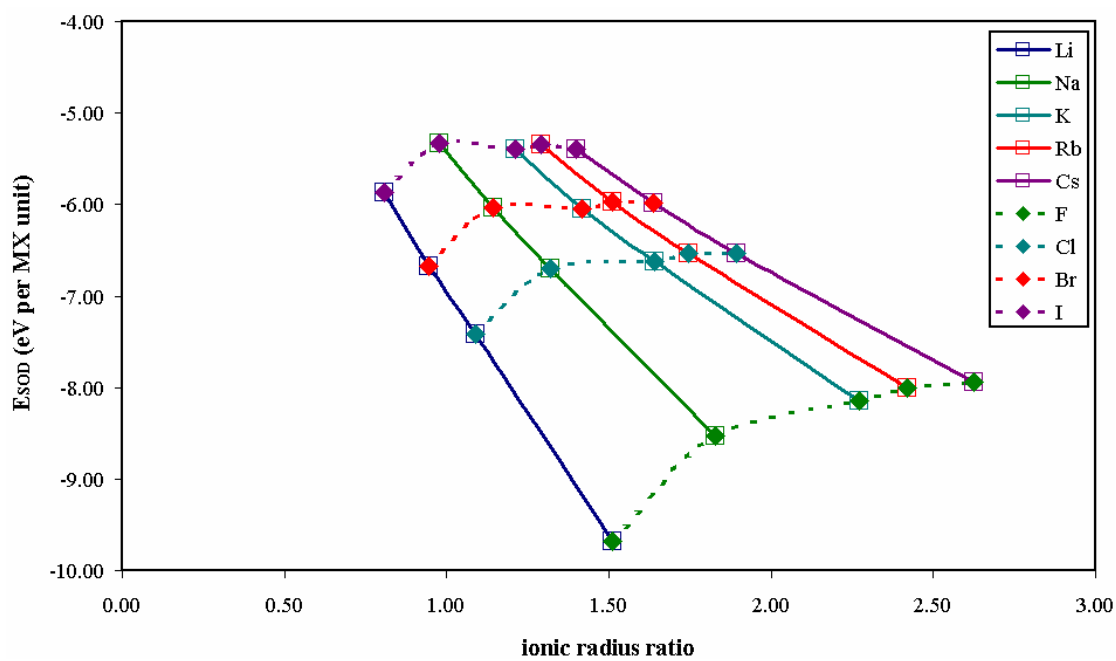
**Table 11** Total energy per MX unit (in eV) and volume per MX unit (in Å<sup>3</sup>) of the rock salt and sodalite phases of the alkali halide polymorphs.

MX	Rock salt		Sodalite	
	energy	volume	energy	volume
LiF	-9.73	16.85	-9.68	25.87
LiCl	-7.44	34.14	-7.42	52.37
LiBr	-6.69	41.77	-6.67	64.12
LiI	-5.88	54.50	-5.87	84.07
NaF	-8.72	25.49	-8.53	41.37
NaCl	-6.85	45.73	-6.70	74.56
NaBr	-6.18	54.52	-6.04	88.93
NaI	-5.45	69.17	-5.32	113.12
KF	-8.33	40.94	-8.15	66.81
KCl	-6.82	65.99	-6.62	110.22
KBr	-6.24	76.35	-6.04	128.03
KI	-5.58	93.57	-5.40	158.11
RbF	-8.17	47.20	-8.01	76.31
RbCl	-6.73	75.04	-6.54	125.60
RbBr	-6.16	86.22	-5.97	144.65
RbI	-5.54	104.77	-5.35	177.50
CsF	-8.06	57.10	-7.94	90.68
CsCl	-6.71	88.49	-6.53	146.49
CsBr	-6.17	100.72	-5.99	168.69
CsI	-5.58	121.03	-5.39	205.09

For all the alkali halides series, the energy minimum for the SOD-MX structure has a volume per MX unit which is significantly larger than that of the rs-MX structure with a concomitant lower density. Moreover, the SOD-MX phase is always higher in energy than that of the rs-MX polymorph. This represents a qualitative difference with respect to the results for the  $(MX)_{12}$  slab and cage clusters where the cage structure was predicted to be more stable for the lithium halides. Nevertheless, as with the clusters, LiF is found to be the most stable compound in both rs-MX and SOD-MX phases with the calculated total energies being rather close: -9.73 eV/LiF and -9.68 eV/LiF respectively. In order to investigate energetic trends, following the above analysis of the clusters, the dependence of the total energy of the rs-MX and SOD-MX phases with respect to the ionic radii ratio of the respective alkali metal and halide have been considered. For both phases, the total energy of the most stable polymorph, for a given cation while varying the anion, increases almost linearly with decreasing the ionic radii ratio (see Figure 26a, 26b) in line with the trend observed for the clusters. Also following the variation in cluster energetics, one can also observe relatively little change in the energy of either bulk phase with the MCl, MBr, or MI composition, whereas the SOD-MF and rs-MF phases are particularly stable.



(a)



(b)

**Figure 26** Total energy MX halides materials (a) rs and (b) SOD as a function of the cation and anion.

Examining the energy difference between rs-MX and SOD-MX phases at their corresponding optimized geometries, Figure 27 shows that the energy difference between the rs-MX and SOD-MX phases also follows the same trend as the energy difference between the slab and cage (MX)<sub>12</sub> clusters (Figure 23).

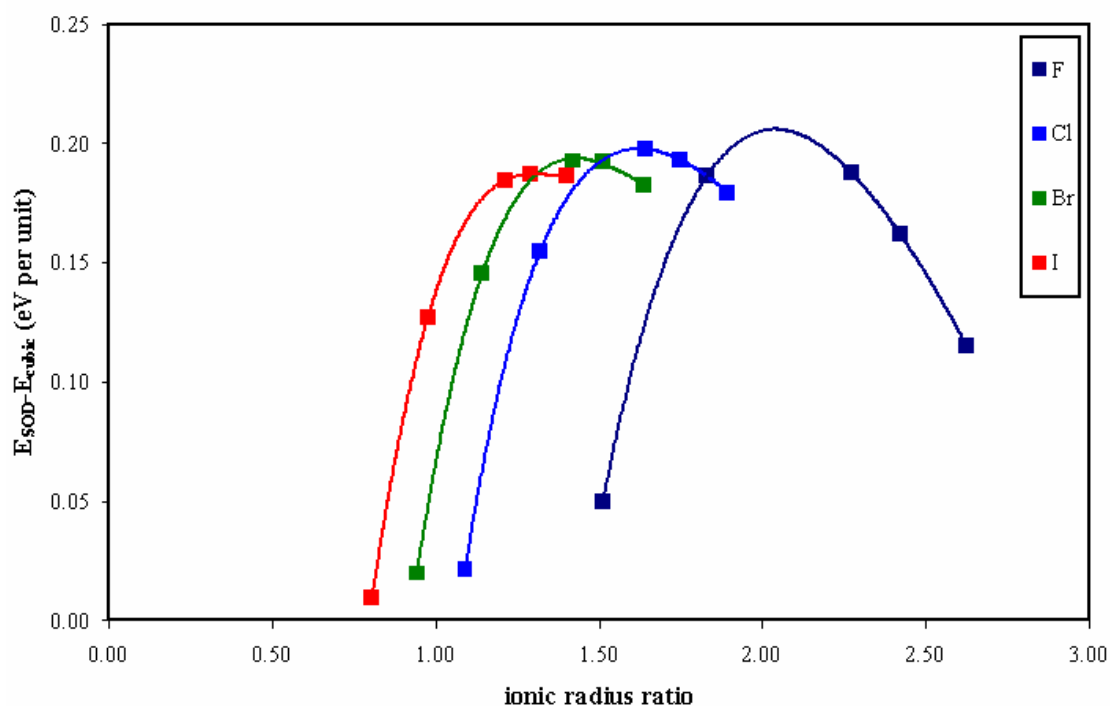


**Figure 27** Energy difference per MX unit (in eV) between the rs-MX and SOD-MX alkali halide materials as a function of the cation/anion ionic radius. Each set of points relates to a series maintaining the halide and varying the alkali metal. (the lines are parabolic fits to the points to guide the eye)

This interesting finding strongly suggests that the relative energy of the rs-MX and SOD-MX crystal structures is largely determined by the same driving forces that cause the energy difference between the slab and cage building blocks. However, contrary to the cluster energetics, the SOD-MX phase is always less stable than rs-MX. However, for the most stable SOD-MX materials (i.e. those containing the smallest cation, Li) the minimum energies of the SOD-LiX phases (LiF, LiCl, LiBr and LiI) are only 0.01-0.05 eV/LiX above the ground state rs-LiX structure. These very small energy differences suggest that for these compositions the SOD-LiX structure could be a viable synthesis target. Furthermore, in line with the behavior observed in Figure 23 for the clusters, SOD-CsF phase (exhibiting a significant difference between anion and cation radius) is only 0.12 eV/CsF higher than the rs-CsF phase.

### **Stability of SOD-LiF**

In order to compare present results with previous work, this thesis have calculated the energy versus volume EOS for rs-LiF and SOD-LiF together with a range of other reported phases in the literature. In particular we compare the bottom-up generated LiF-SOD phase with three new LiF phases predicted by Doll et al (Doll *et al.*, 2007) by global optimization. These authors have also carried out periodic Hartree-Fock and LDA calculations for the different polymorphs predicted from their global optimization studies. Interestingly, the low density SOD-LiF structure was not located by this method although it is very competitive in energy with respect to their newly predicted low energy LiF-phases. The probable reason for this omission is not due to any failure in the global optimization methodology employed but rather due to the concentration on relatively dense materials with typically smaller unit cells. Although periodic Hartree-Fock calculations incorrectly predicts wurtzite as the most stable LiF polymorph, both LDA calculations by Doll et al. (Doll *et al.*, 2007) and the present GGA calculations correctly predict rs-LiF to be the most stable structure, in agreement with experiment. The energetic stability order of the remaining polymorphs predicted by LDA and GGA is, however, rather different. This is not so surprising since LDA is known to overestimate binding energies. Consequently,

different polymorphs with different crystal structures and different coordinations around each atom and are affected differently by the LDA error. The GGA energies are likely to be considerably more accurate and it is likely that the phase diagram in Figure 28 provides a more realistic picture of the energy landscape of LiF polymorphs. The optimized parameters are shown in Table 12. The GGA calculated EOS curves predict that the SOD-LiF structure is marginally lower in energy than the LiF-I phase and significantly lower in energy than the LiF-II and LiF-III phases generated by Doll *et al.* (Doll *et al.*, 2007). Only four phases appear to lie lower in energy than the SOD-LiF phase: rs-LiF, 5-5-LiF, wz-LiF (wurtzite), and zb-LiF (zincblende), all of which are significantly denser than SOD-LiF. The 5-5 phase (also known as the hexagonal phase in other studies (Carrasco *et al.*, 2007; Limpijumnong and Lambrecht, 2001) was first proposed by Schön in the context of global optimization of alkali metal oxide phases (Schoen, 2004). Interestingly, from a bottom-up perspective, the 5-5 phase can also be regarded as being generated from the assembly of hexagonal tubular clusters. Structurally, the 5-5 phase lies between wurtzite and rocksalt and is thought to be a relatively unstable phase with respect to its collapse into rocksalt, and, thus, 5-5-LiF is probably only viable as a real material at very low temperatures and low pressures (Doll *et al.*, 2007; Limpijumnong and Lambrecht, 2001; Schoen, 2004). Although the EOS curve of SOD-LiF shows that the structure is stable with respect to a wide range of pressures (both negative and positive in relation to the ground state) this only strictly applies at 0 K. Considering that SOD-LiF is one of the lowest density phase yet predicted for a purely ionic material it is of interest as to whether the structure would be also stable to collapse to a denser more stable phase at finite temperatures.

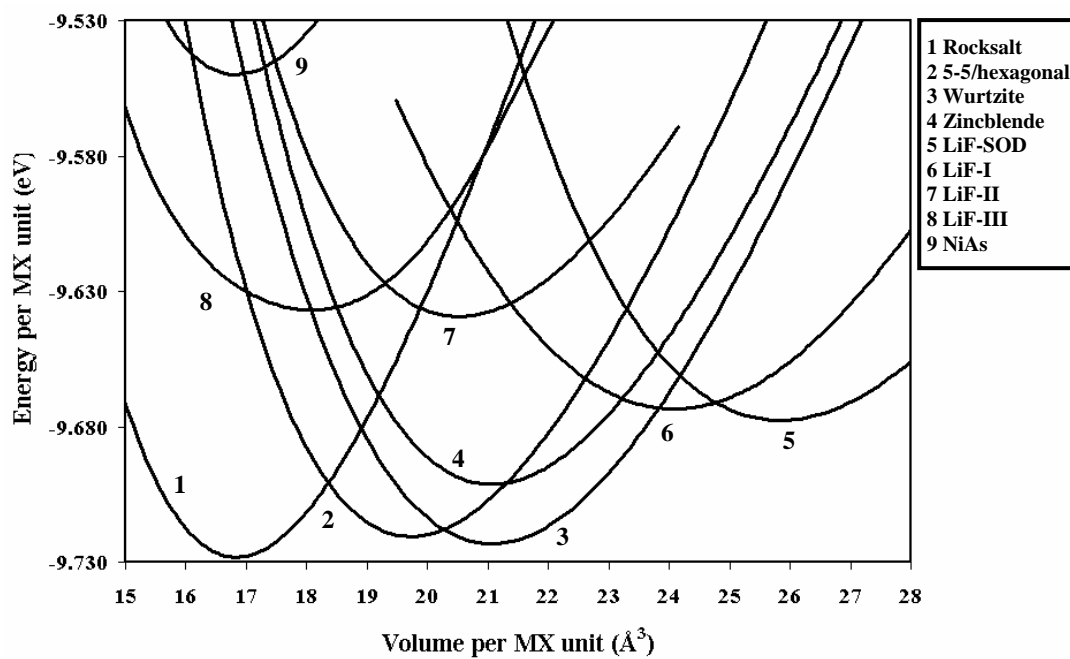


**Figure 28** Energy versus volume phase diagram for various polymorphs of LiF:  
 1=Rock salt, 2=5-5 (or hexagonal), 3=Wurtzite, 4=Zincblende, 5=SOD  
 6=LiF-I, 7=LiF-II, 8=LiF-III, and 9=NiAs.

**Table 12** Properties of a range of LiF polymorphs calculated from the EOS fits to the GGA-DFT:  $E_0$ , minimum total energy (eV/LiF),  $\Delta E_0$ , total energy differences (eV/LiF),  $V_0$ , volume at minimum energy ( $\text{\AA}^3/\text{LiF}$ ) and  $B_0$ , the bulk modulus (GPa/LiF).

	$E_0$	$\Delta E_0$	$V_0$	$B_0$
rs-LiF	-9.726	0.000	16.85	68.55
zb-LiF	-9.700	0.026	21.06	51.75
wz-LiF	-9.720	0.006	21.08	48.33
NiAs-LiF	-9.550	0.176	17.02	67.33
5-5-LiF	-9.701	0.006	16.94	60.43
LiF-I	-9.673	0.054	24.05	36.03
LiF-II	-9.639	0.087	20.52	48.63
LiF-III	-9.639	0.087	18.13	72.45
SOD-LiF	-9.676	0.050	25.87	41.66

In order to test the finite temperature stability of LiF-SOD, the additional calculations have employed constant pressure and temperature (NPT) in molecular dynamics (MDs). Due to the current unavailability of NPT-MD simulations within the VASP code and the very high computational expense of performing such simulations in a full ab-initio manner, classical MDs were used. For these simulations employed the GULP code (Gale, 1997) and the interionic potentials of Catlow *et al.* (Catlow *et al.*, 1977) with a 3  $\text{\AA}$  cut-off and a 0.25  $\text{\AA}$  smoothing taper to avoid discontinuities in the energy and first and second derivatives. Importantly, considering the ELF analysis in section 2, the potentials account for ionic polarization by the shell model of Dick and Overhauser (Dick and Overhauser, 1958). Firstly, it is note that energy minimizations of atomic position and cell parameters using these potentials, confirm that the SOD-LiF phase is metastable (by 0.03-0.17 eV/LiF) with respect to the lower energy denser phases (rs-LiF, wz-LiF, zb-LiF, 5-5-LiF) in qualitative agreement with the GGA-DFT optimizations. This confirms that the SOD-MX phase is not artificially stabilised by the potential which recover the small energetic preference for these

dense LiF phases. Furthermore, although fitted with respect to rs-LiF, the potentials also give optimized SOD-LiF cell parameters ( $a, b, c = 5.17\text{\AA}$ ,  $\alpha, \beta, \gamma = 90^\circ$ ) in reasonable agreement with the GGA results ( $a, b, c = 5.37\text{\AA}$ ,  $\alpha, \beta, \gamma = 90^\circ$ ). After first equilibrating the SOD-LiF system for 30 ps, the system is simulated the behavior of a SOD-LiF  $2 \times 2 \times 2$  supercell at 300 K at zero external pressure for 350 ps throughout the MD simulation and found that the bonding topology of the SOD-LiF structure remained fully intact with the root mean squared deviations from the optimal cell parameters varying by only  $0.12\text{ \AA}$  and cell angles by  $1.44$  degrees. Surprisingly, unlike the probable instability of the 5-5-LiF phase, this suggests that the SOD-LiF phase, if synthesized, should be structurally stable at finite temperatures. In Figure 29 we show a typical snapshot from the MD simulations.

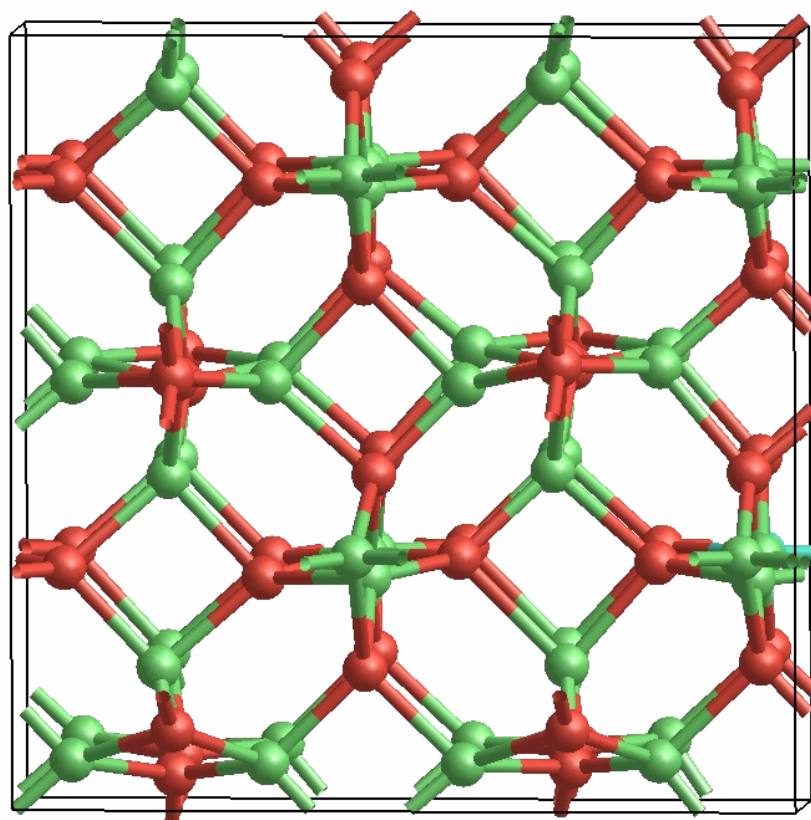


**Figure 29** Snapshot from the MD simulation of the SOD-LiF phase showing a typical configuration of the  $2 \times 2 \times 2$  super cell at 300 K. Red spheres represent the fluoride anion whereas the green spheres represent the cations.

## CONCLUSIONS

### Carbonyl-ene reaction on Na-FAU

The carbonyl-ene reaction between formaldehyde and propylene has been investigated theoretically. Three different models were employed to model the carbonyl-ene reaction system: (1) Na-exchanged faujasite zeolite, (2) the naked Na(I) ion system, and (3) the bare system. The reaction occurs via a concerted mechanism without an intermediate and involves a proton transfer from propylene to formaldehyde and a carbon-carbon bond formation which occur simultaneously at the transition state. The interaction between Na-exchanged faujasite zeolite and formaldehyde leads to a structure in which formaldehyde is stabilized in the zeolite framework. The energy barrier for this system is calculated to be 25.1 kcal/mol and the apparent activation energy is  $-3.2$  kcal/mol. It is well established that carbonyl-ene reactions are catalyzed by Lewis acids. In order to gain some insight into the mechanism by which a Lewis acid can catalyze this reaction, we employed Na(I) as a Lewis acid in order to compare these results (2) with the results from the Na-exchanged zeolite system (1). The activation barrier in system (2) is even lower (17.5 kcal/mol), due to the electrostatic interaction between the naked Na(I) ion and the complex. In the bare system (3) where no zeolite framework or electrostatic field from Na(I) are present, the structure of the transition state is a 6-membered ring and its energy barrier is 34.4 kcal/mol. The results indicate that Na-exchanged faujasite can preserve formaldehyde in a monomeric form and can also act as a Lewis acid which can catalyze the carbonyl-ene reaction of formaldehyde with olefins without the presence of potentially harmful acidic chemicals.

### Adsorption and diffusion of *n*-hexane in nanoporous silicate MCM-41

The adsorption and diffusion of *n*-hexane in simple models of siliceous MCM-41 at room temperature were studied by molecular dynamics simulations. New potential parameters were constructed from existing ones and experimental energetic data. The adsorption energies at a loading of one *n*-hexane molecule per supercell

range between -9.1 and -13.7 kcal/mol. The variation of the molecular self-diffusion coefficients with loadings exhibits the normal trend of decreasing self-diffusion with increasing loadings and decreasing size of the pores. From the calculated radial distribution functions it can be seen that the *n*-hexane molecules have an average centers of mass distance of about 6.3-6.6 Å, slightly less than in the liquid phase (6.7 Å). This is also a result of the confined space. We calculated the radial distribution of *n*-hexane molecules to the center of the pore channel and found that at low loadings they prefer locations parallel to and close to the pore surface. With increased loadings the *n*-hexane molecules arrange themselves into concentric ring and chainlike structures inside the pores.

### **Theoretical bottom-up Study Stable Nanoporous Alkali Halide Polymorphs**

The possible existence of low density phases of bulk alkali halides has been investigated using a bottom-up approach together with state-of-the-art plane wave DF calculations. To this end, the relative energies of the lowest energy cluster isomers of  $(MX)_{12}$  have been studied throughout the MX series. The slab form of the  $(MX)_{12}$  cluster may be viewed as the precursor of the rock-salt (rs-MX) structure while the assembling of  $(MX)_{12}$  cages can lead to a low density phase reminiscent of the sodalite zeolite (SOD-MX). The slab  $(MX)_{12}$  isomer is found to be energetically more stable than the cage, except for the LiX (X = F, Cl, Br, I) series where the cage is the most stable  $(MX)_{12}$  cluster isomer. For a given halide series the energy difference between slab and cage isomers increases up until a maximum is reached and then decreases towards CsX. In the bulk analogues, the same behaviour with respect to the energy difference between rs-MX and SOD-MX is also observed. In both cases, the trends may be approximately rationalized in terms of ionic packing. In all alkali halides the SOD-MX phase is found to be stable with respect to compression and expansion at 0 K through the calculation of their volume versus energy EOS. Furthermore, in the LiX (X = F, Cl, Br, I) series, where the cage is the ground state  $(LiX)_{12}$  cluster, the SOD-LiX material is found to be particularly low in energy with respect to the lowest energy rs-LiX phase ( $E_{SOD-rs}$  energy differences ranging between 0.01-0.05 eV/LiX). Taking the LiF-SOD phase as a case study, we have further

employed MD simulations to confirm that the structure of this nanoporous alkali halide is thermally stable at 300 K. Considering that the lowest energy cluster for  $(\text{LiX})_{12}$  is an open cage, together with the demonstration that for LiF, a nanoporous phase based upon its assembly, is stable with respect to zero pressure variation and at finite temperature, we suggest that these highly ionic yet low density materials may be realistic, yet challenging, synthesis targets through an appropriate bottom-up route.

**LITERATURE CITED**

- Aguado, A., A. Ayuela, J.M. Lopez and J.A. Alonso. 1997. Structure and bonding in small neutral alkali halide clusters. **Phys. Rev. B: Condens. Matter**, 56(23):15353-15360.
- Alder, B.J. and T.E. Wainwright. 1957. Phase transition for a hard sphere system. **J. Chem. Phys.**, 27128.
- Barlak, T.M., J.E. Campana, R.J. Colton, J.J. DeCorpo and J.R. Wyatt. 1981. Secondary ion mass spectrometry of metal halides. 1. Stability of alkali iodide clusters. **J. Phys. Chem.**, 85(25):3840-3844.
- \_\_\_\_\_, J.R. Wyatt, R.J. Colton, J.J. DeCorpo and J.E. Campana. 1982. Secondary ion mass spectrometry of metal halides. 2. Evidence for structure in alkali iodide clusters. **J. Am. Chem. Soc.**, 104(5):1212-1215.
- Beauvais, C., X. Guerrault, F.-X. Coudert, A. Boutin and A.H. Fuchs. 2004. Distribution of Sodium Cations in Faujasite-Type Zeolite: A Canonical Parallel Tempering Simulation Study. **J. Phys. Chem. B**, 108(1):399-404.
- Beck, J.S., J.C. Vartuli, W.J. Roth, M.E. Leonowicz, C.T. Kresge, K.D. Schmitt, C.T.W. Chu, D.H. Olson and E.W. Sheppard. 1992. A new family of mesoporous molecular sieves prepared with liquid crystal templates **J. Am. Chem. Soc.**, 114(27):10834-10843.
- Becke, A.D. and K.E. Edgecombe. 1990. A simple measure of electron localization in atomic and molecular systems. **J. Chem. Phys.**, 925397.
- Benson, S.W. and H.E. O'Neal. 1970. **Kinetic Data on Gas Phase Unimolecular Reactions**; National Standard and Reference Data Series.
- Berenguer-Murcia, A., A.J. Fletcher, J. Garcia-Martinez, D. Cazorla-Amoros, A. Linares-Solano and K.M. Thomas. 2003. Probe Molecule Kinetic Studies of Adsorption on MCM-41. **J. Phys. Chem. B**, 107(4):1012-1020.
- Birch, F. 1947. Finite Elastic Strain of Cubic Crystals. **Phys. Rev.**, 71809.
- Blöchl, P.E. 1994. Projector augmented-wave method. **Phys. Rev. B**, 5017953.
- Bloomfield, L.A., C.W.S. Conover, Y.A. Yang, Y.J. Twu and N.G. Phillips. 1991. Experimental and theoretical studies of the structure of alkali halide clusters. **Z. Phys. D: At., Mol. Clusters**, 20(1-4):93-96.

- Bobuatong, K. and J. Limtrakul. 2003. Effects of the zeolite framework on the adsorption of ethylene and benzene on alkali-exchanged zeolites: an ONIOM study. **Appl. Catal., A**, 253(1):49-64.
- Boger, T., R. Roesky, R. Glaeser, S. Ernst, G. Eigenberger and J. Weitkamp. 1997. Influence of the aluminum content on the adsorptive properties of MCM-41. **Microporous Mater.**, 8(1,2):79-91.
- Braendle, M. and J. Sauer. 1998. Acidity Differences between Inorganic Solids Induced by Their Framework Structure. A Combined Quantum Mechanics/Molecular Mechanics ab Initio Study on Zeolites. **J. Am. Chem. Soc.**, 120(7):1556-1570.
- Campana, J.E., T.M. Barlak, R.J. Colton, J.J. DeCorpo, J.R. Wyatt and B.I. Dunlap. 1981. Effect of cluster surface energies on secondary-ion-intensity distributions from ionic crystals. **Phys. Rev. Lett.**, 47(15):1046-1049.
- Cao, D., Z. Shen, J. Chen and X. Zhang. 2004. Experiment, molecular simulation and density functional theory for investigation of fluid confined in MCM-41. **Microporous Mesoporous Mater.**, 67(2-3):159-166.
- Carpenter, J.E. and F. Weinhold. 1988. Analysis of the geometry of the hydroxymethyl radical by the "different hybrids for different spins" natural bond orbital procedure. **J. Mol. Struct.: THEOCHEM**, 16941-62.
- Carrasco, J., F. Illas and S.T. Bromley. 2007. Ultralow-Density Nanocage-Based Metal-Oxide Polymorphs. **Phys. Rev. Lett.**, 99(23):235502/235501-235502/235504.
- Catlow, C.R.A., K.M. Diller and M.J. Norgett. 1977. Interionic potentials for alkali halides. **J. Phys. C: Solid State Phys.**, 10(9):1395-1412.
- Choomwattana, S., T. Maihom, P. Khongpracha, M. Probst and J. Limtrakul. 2008. Structures and Mechanisms of the Carbonyl-ene Reaction between MOF-11 Encapsulated Formaldehyde and Propylene: An ONIOM Study. **J. Phys. Chem. C**, 112(29):10855-10861.
- Courivaud, F., E.W. Hansen, A. Karlsson, S. Kolboe and M. Stocker. 2000a. Pulsed field gradient NMR study of the diffusion of n-hexane confined in hydroxylated and dehydroxylated MCM-41 of various pore diameters. **Microporous Mesoporous Mater.**, 35-36327-339.
- \_\_\_\_\_, \_\_\_\_\_, S. Kolboe, A. Karlsson and M. Stocker. 2000b. Enhanced n-hexane diffusion in partially filled MCM-41 of different surface hydrophobicity probed by NMR. **Microporous Mesoporous Mater.**, 37(1-2):223-232.

- Croteau, T. and G.N. Patey. 2006. Structures and rearrangements of LiCl clusters. **J. Chem. Phys.**, 124(24):244506/244501-244506/244507.
- de Vries, A.H., P. Sherwood, S.J. Collins, A.M. Rigby, M. Rigutto and G.J. Kramer. 1999. Zeolite Structure and Reactivity by Combined Quantum-Chemical-Classical Calculations. **J. Phys. Chem. B**, 103(29):6133-6141.
- Deka, R.C. and K. Hirao. 2002. Lewis acidity and basicity of cation-exchanged zeolites: QM/MM and density functional studies. **J. Mol. Catal. A: Chem.**, 181(1-2):275-282.
- Demontis, P., G.B. Suffritti, S. Bordiga and R. Buzzoni. 1995. Atom pair potential for molecular dynamics simulations of structural and dynamic properties of aluminosilicates: test on silicalite and anhydrous Na-A and Ca-A zeolites and comparison with experimental data. **J. Chem. Soc., Faraday Trans.**, 91(3):525-533.
- Di Renzo, F., H. Cambon and R. Dutartre. 1997. A 28-year-old synthesis of micelle-templated mesoporous silica. **Microporous Mater.**, 10(4-6):283-286.
- Dick, B.G. and A.W. Overhauser. 1958. Theory of the Dielectric Constants of Alkali Halide Crystals. **Phys. Rev.**, 11290-103.
- Doll, K., J.C. Schoen and M. Jansen. 2007. Global exploration of the energy landscape of solids on the ab initio level. **PCCP**, 9(46):6128-6133.
- Doye, J.P.K. and D.J. Wales. 1999. Structural transitions and global minima of sodium chloride clusters. **Phys. Rev. B: Condens. Matter**, 59(3):2292-2300.
- Ens, W., R. Beavis and K.G. Standing. 1983. Time-of-flight measurements of cesium-iodide cluster ions. **Phys. Rev. Lett.**, 50(1):27-30.
- Foster, J.P. and F. Weinhold. 1980. Natural hybrid orbitals. **J. Am. Chem. Soc.**, 102(24):7211-7218.
- Fox, J.P. and S.P. Bates. 2005. Adsorption and Structure of Hydrocarbons in MCM-41: A Computational Study. **Langmuir**, 21(10):4746-4754.
- Freeman, C.L., F. Claeysens, N.L. Allan and J.H. Harding. 2006. Graphitic Nanofilms as Precursors to Wurtzite Films: Theory. **Phys. Rev. Lett.**, 96(6):066102/066101-066102/066104.
- Gale, J.D. 1997. GULP: a computer program for the symmetry-adapted simulation of solids. **J. Chem. Soc., Faraday Trans.**, 93(4):629-637.

- Girgis, M.J. and Y.P. Tsao. 1996. Impact of Catalyst Metal-Acid Balance in n-Hexadecane Hydroisomerization and Hydrocracking. **Ind. Eng. Chem. Res.**, 35(2):386-396.
- Goniakowski, J., C. Noguera and L. Giordano. 2004. Using Polarity for Engineering Oxide Nanostructures: Structural Phase Diagram in Free and Supported MgO(111) Ultrathin Films. **Phys. Rev. Lett.**, 93(21):215702/215701-215702/215704.
- Greatbanks, S.P., I.H. Hillier, N.A. Burton and P. Sherwood. 1996. Adsorption of water and methanol on zeolite Brønsted acid sites: an ab initio, embedded cluster study including electron correlation. **J. Chem. Phys.**, 105(9):3770-3776.
- Hansen, E.W., F. Courivaud, A. Karlsson, S. Kolboe and M. Stocker. 1998. Effect of pore dimension and pore surface hydrophobicity on the diffusion of n-hexane confined in mesoporous MCM-41 probed by NMR. A preliminary investigation. **Microporous Mesoporous Mater.**, 22(1-3):309-320.
- Hemley, R.J. 1998. **Ultrahigh-Pressure Mineralogy: Physics and Chemistry of the Earth's Deep Interior**. vol. 37 of Reviews in Mineralogy.
- Hillier, I.H. 1999. Chemical reactivity studied by hybrid QM/MM methods. **J. Mol. Struct.: THEOCHEM**, 463(1-2):45-52.
- Hussain, I. and J.O. Titiloye. 2005. Molecular dynamics simulations of the adsorption and diffusion behavior of pure and mixed alkanes in silicalite. **Microporous Mesoporous Mater.**, 85(1-2):143-156.
- Janchen, J., H. Stach, M. Busio and J.H.M.C. van Wolput. 1998. Microcalorimetric and spectroscopic studies of the acidic- and physisorption characteristics of MCM-41 and zeolites. **Thermochim. Acta**, 312(1-2):33-45.
- Jansang, B., T. Nanok and J. Limtrakul. 2006. Structures and Reaction Mechanisms of Cumene Formation via Benzene Alkylation with Propylene in a Newly Synthesized ITQ-24 Zeolite: An Embedded ONIOM Study. **J. Phys. Chem. B**, 110(25):12626-12631.
- \_\_\_\_\_, \_\_\_\_\_ and \_\_\_\_\_. 2008. Structure and reaction mechanism of alkylation of phenol with methanol over H-FAU zeolite: an ONIOM study. **J. Phys. Chem. C**, 112(2):540-547.
- Joshi, Y.V. and K.T. Thomson. 2005. Embedded cluster (QM/MM) investigation of C<sub>6</sub> diene cyclization in HZSM-5. **J. Catal.**, 230(2):440-463.

- Kalidoss, M. and S. Ravi. 2002. New method of determining the structure factor of real liquids and their mixtures using ultrasonic velocity. **Physica A**, 312(1-2):59-69.
- Kasuriya, S., S. Namuangruk, P. Treesukol, M. Tirtowidjojo and J. Limtrakul. 2003. Adsorption of ethylene, benzene, and ethylbenzene over faujasite zeolites investigated by the ONIOM method. **J. Catal.**, 219(2):320-328.
- Katakuse, I., T. Ichihara, H. Ito, T. Matsuo, T. Sakurai and H. Matsuda. 1988. Ultra-high mass spectra of cesium iodide clusters and evidence for the existence of stable neutral cubic-like structures with an even number of atoms. **Rapid Commun. Mass Spectrom.**, 2(9):191-194.
- Khaliullin, R.Z., A.T. Bell and V.B. Kazansky. 2001. An Experimental and Density Functional Theory Study of the Interactions of CH<sub>4</sub> with H-ZSM-5. **J. Phys. Chem. A**, 105(45):10454-10461.
- Kioupis, L.I. and E.J. Maginn. 1999. Rheology, dynamics, and structure of hydrocarbon blends: a molecular dynamics study of n-hexane/n-hexadecane mixtures. **Chem. Eng. J. (Lausanne)**, 74(1-2):129-146.
- Kleestorfer, K., H. Vinek and A. Jentys. 2001. Structure simulation of MCM-41 type materials. **J. Mol. Catal. A: Chem.**, 166(1):53-57.
- Koh, C.A., R.E. Westacott, R.I. Nooney, V. Boissel, S.F. Tahir and V. Tricarico. 2002. Separation of dichloromethane-nitrogen mixtures by adsorption: experimental and molecular simulation studies. **Mol. Phys.**, 100(13):2087-2095.
- Kresge, C.T., M.E. Leonowicz, W.J. Roth, J.C. Vartuli and J.S. Beck. 1992. Ordered mesoporous molecular sieves synthesized by a liquid-crystal template mechanism. **Nature**, 359:710-712.
- Kresse, G. and J. Furthmüller. 1996. Efficient iterative schemes for ab initio total-energy calculations using a plane-wave basis set. **Phys. Rev. B: Condens. Matter**, 54(16):11169-11186.
- \_\_\_\_\_, and \_\_\_\_\_. 1996. Efficiency of ab-initio total energy calculations for metals and semiconductors using a plane-wave basis set. **Comput. Mater. Sci.**, 6(1):15-50.
- Kresse, G. and J. Hafner. 1993. Ab initio molecular dynamics for liquid metals. **Phys. Rev. B** 47:558.
- \_\_\_\_\_ and D. Joubert. 1999. From ultrasoft pseudopotentials to the projector augmented-wave method. **Phys. Rev. B: Condens. Matter**, 59(3):1775-1775.

- Krokidis, X., S. Noury and B. Silvi. 1997. Characterization of Elementary Chemical Processes by Catastrophe Theory. **J. Phys. Chem. A**, 101(39):7277-7282.
- Kulkarni, A.J., M. Zhou, K. Sarasamak and S. Limpijumnong. 2006. Novel Phase Transformation in ZnO Nanowires under Tensile Loading. **Phys. Rev. Lett.**, 97(10):105502/105501-105502/105504.
- Leroy, F., B. Rousseau and A.H. Fuchs. 2004. Self-diffusion of n-alkanes in silicalite using molecular dynamics simulation: A comparison between rigid and flexible frameworks. **PCCP**, 6(4):775-783.
- Limpijumnong, S. and W.R.L. Lambrecht. 2001. Theoretical study of the relative stability of wurtzite and rocksalt phases in MgO and GaN. **Phys. Rev. B: Condens. Matter**, 63(10):104103/104101-104103/104111.
- Limtrakul, J. 1995. Adsorption of methanol in zeolite, gallosilicate and SAPO catalysts. **Chem. Phys.**, 193(1-2):79-87.
- \_\_\_\_\_, S. Jungstittiwong and P. Khongpracha. 2000. Adsorption of carbon monoxide on H-FAU and Li-FAU zeolites. An embedded cluster approach. **J. Mol. Struct.**, 525153-162.
- \_\_\_\_\_, T. Nanok, S. Jungstittiwong, P. Khongpracha and T.N. Truong. 2001. Adsorption of unsaturated hydrocarbons on zeolites: the effects of the zeolite framework on adsorption properties of ethylene. **Chem. Phys. Lett.**, 349(1,2):161-166.
- \_\_\_\_\_, P. Treesukol, C. Ebner, R. Sansone and M. Probst. 1997. Structures and potential energy surface of Faujasitic zeolite/water. **Chem. Phys.**, 215(1):77-87.
- Lintuluoto, M. 2002. Theoretical study on the structure and energetics of alkali halide clusters. **J. Mol. Struct.: THEOCHEM**, 540177.
- Liu, L. and W.A. Bassett. 1986. **Elements, Oxides, and Silicates. High-Pressure Phases with Implications for the Earth's Interior.**
- Llewellyn, P.L., F. Schueth, Y. Grillet, F. Rouquerol, J. Rouquerol and K.K. Unger. 1995. Water Sorption on Mesoporous Aluminosilicate MCM-41. **Langmuir**, 11(2):574-577.
- Maihom, T., S. Namuangruk, T. Nanok and J. Limtrakul. 2008. Theoretical Study on Structures and Reaction Mechanisms of Ethylene Oxide Hydration over H-ZSM-5: Ethylene Glycol Formation. **J. Phys. Chem. C**, 112(33):12914-12920.

- Namuangruk, S., P. Pantu and J. Limtrakul. 2004. Alkylation of benzene with ethylene over faujasite zeolite investigated by the ONIOM method. **J. Catal.**, 225(2):523-530.
- Nanok, T., P.A. Bopp and J. Limtrakul. 2005. Molecular dynamics simulation studies of p-xylene in OH-free Si-MCM-41. **Z. Naturforsch. A**, 60(11/12):805-813.
- Nguyen, C., C.G. Sonwane, S.K. Bhatia and D.D. Do. 1998. Adsorption of Benzene and Ethanol on MCM-41 Material. **Langmuir**, 14(17):4950-4952.
- Nicholas, J.B., A.J. Hopfinger, F.R. Trouw and L.E. Iton. 1991. Molecular modeling of zeolite structure. 2. Structure and dynamics of silica sodalite and silicate force field **J. Am. Chem. Soc.**, 113(13):4792-4800.
- Ochsenfeld, C. and R. Ahlrichs. 1994. An ab initio investigation of structure and energetics of clusters  $\text{KnCl}_n$  and  $\text{LinFn}$ . **Ber. der Bunsen-Gesellschaft**, 98(1):34-47.
- Oganov, A.R. and C.W. Glass. 2006. Crystal structure prediction using ab initio evolutionary techniques: Principles and applications. **J. Chem. Phys.**, 124(24):244704/244701-244704/244715.
- Okachi, T. and M. Onaka. 2004. Formaldehyde Encapsulated in Zeolite: A Long-Lived, Highly Activated One-Carbon Electrophile to Carbonyl-Ene Reactions. **J. Am. Chem. Soc.**, 126(8):2306-2307.
- Olson, D.H. and E. Dempsey. 1969. The crystal structure of the zeolite hydrogen faujasite. **J. Catal.**, 13(2):221-231.
- Perdew, J.P., J.A. Chevary, S.H. Vosko, K.A. Jackson, M.R. Pederson, D.J. Singh and C. Fiolhais. 1992. Atoms, molecules, solids, and surfaces: Applications of the generalized gradient approximation for exchange and correlation. **Phys. Rev. B**, 46:6671-6687.
- Pettifer, D. 1995. Bonding and Structure of Molecules and Solids
- Pflaum, R., P. Pfau, K. Sattler and E. Recknagel. 1985. Electron impact studies on sodium halide microclusters. **Surf. Sci.**, 165-172.
- Qiao, S.Z. and S.K. Bhatia. 2005. Diffusion of n-decane in mesoporous MCM-41 silicas. **Microporous Mesoporous Mater.**, 86(1-3):112-123.
- \_\_\_\_\_, \_\_\_\_\_, and D. Nicholson. 2004. Study of Hexane Adsorption in Nanoporous MCM-41 Silica. **Langmuir**, 20(2):389-395.

- Rathousky, J., A. Zukal, O. Franke and G. Schulz-Ekloff. 1995. Adsorption on MCM-41 mesoporous molecular sieves. Part 2. Cyclopentane isotherms and their temperature dependence. **J. Chem. Soc., Faraday Trans.**, 91(5):937-940.
- Reed, A.E., L.A. Curtiss and F. Weinhold. 1988. Intermolecular interactions from a natural bond orbital, donor-acceptor viewpoint. **Chem. Rev.**, 88(6):899-926.
- \_\_\_\_\_, and F. Weinhold. 1983. Natural bond orbital analysis of near-Hartree-Fock water dimer. **J. Chem. Phys.**, 78(6):4066.
- \_\_\_\_\_, R.B. Weinstock and F. Weinhold. 1985. Natural population analysis. **J. Chem. Phys.**, 83:735.
- Remko, M. 1997. Gas-phase binding of Li<sup>+</sup>, Na<sup>+</sup> and Mg<sup>2+</sup> to formaldehyde, acetaldehyde and their silicon and sulfur analogs. A theoretical study by means of ab initio molecular orbital methods at the G2 level of theory. **Chem. Phys. Lett.**, 270:369-375.
- Ribeiro Carrott, M.M.L., A.J.E. Candeias, P.J.M. Carrott, P.I. Ravikovitch, A.V. Neimark and A.D. Sequeira. 2001. Adsorption of nitrogen, neopentane, n-hexane, benzene and methanol for the evaluation of pore sizes in silica grades of MCM-41. **Microporous Mesoporous Mater.**, 47(2-3):323-337.
- Roggero, I., B. Civalleri and P. Ugliengo. 2001. Modeling physisorption with the ONIOM method: the case of NH<sub>3</sub> at the isolated hydroxyl group of the silica surface. **Chem. Phys. Lett.**, 341(5,6):625-632.
- Rungsirisakun, R., T. Nanok, M. Probst and J. Limtrakul. 2006. Adsorption and diffusion of benzene in the nanoporous catalysts FAU, ZSM-5 and MCM-22: A molecular dynamics study. **J. Mol. Graph. Model.**, 24(5):373-382.
- Sauer, J., P. Ugliengo, E. Garrone and V.R. Saunders. 1994. Theoretical Study of van der Waals Complexes at Surface Sites in Comparison with the Experiment. **Chem. Rev.**, 94(7):2095-2160.
- Savin, A., R. Nesper, S. Wengert and T.F. Fassler. 1997. ELF: the electron localization function. **Angew. Chem. Int. Ed.**, 36(17):1808-1832.
- Schleife, A., F. Fuchs, J. Furthmüller and F. Bechstedt. 2006. First-principles study of ground- and excited-state properties of MgO, ZnO, and CdO polymorphs. **Phys. Rev. B: Condens. Matter**, 73(24):245212/245211-245212/245214.
- Schön, J.C. 2004. Enthalpy landscapes of the earth alkaline metal oxides. **Z. Anorg. Allg. Chem.**, 630(13-14):2354-2366.
- Sherwood, P., A.H. de Vries, M.F. Guest, G. Schreckenbach, C.R.A. Catlow, S.A. French, A.A. Sokol, S.T. Bromley, W. Thiel and A.J. Turner. 2003. QUASI: A

- general purpose implementation of the QM/MM approach and its application to problems in catalysis. **J. Mol. Struct.: THEOCHEM**, 623(1-3):1-28.
- Silvi, B. and A. Savin. 1994. Classification of chemical bonds based on topological analysis of electron localization functions **Nature**, 371683-686.
- Sinclair, P.E., A. de Vries, P. Sherwood, C.R.A. Catlow and R.A. van Santen. 1998. Quantum-chemical studies of alkene chemisorption in chabazite: A comparison of cluster and embedded-cluster models. **J. Chem. Soc., Faraday Trans.**, 94(22):3401-3408.
- Snider, B.B. 1980. Lewis-acid catalyzed ene reactions. **Acc. Chem. Res.**, 13(11):426-432.
- Sonwane, C.G. and Q. Li. 2005. Structure and Transport Properties of Nanostructured Materials. **J. Phys. Chem. B**, 109(12):5691-5699.
- Stallmach, F., A. Graser, J. Karger, C. Krause, M. Jeschke, U. Oberhagemann and S. Spange. 2001. Pulsed field gradient NMR studies of diffusion in MCM-41 mesoporous solids. **Microporous Mesoporous Mater.**, 44-45745-753.
- Svensson, M., S. Humbel, R.D.J. Froese, T. Matsubara, S. Sieber and K. Morokuma. 1996. ONIOM: A Multi-Layered Integrated MO + MM Method for Geometry Optimizations and Single Point Energy Predictions. A Test for Diels-Alder Reactions and Pt(P(t-Bu)<sub>3</sub>)<sub>2</sub> + H<sub>2</sub> Oxidative Addition. **J. Phys. Chem.**, 100(50):19357-19363.
- Tanchoux, N., P. Trens, D. Maldonado, F. Di Renzo and F. Fajula. 2004. The adsorption of hexane over MCM-41 type materials. **Colloids Surf., A**, 246(1-3):1-8.
- Tang, H.R. and K.N. Fan. 2000. Application of ONIOM to cluster modeling of the metal surface. **Chem. Phys. Lett.**, 330(5,6):509-514.
- Torrent, M., T. Vreven, D.G. Musaev, K. Morokuma, O. Farkas and H.B. Schlegel. 2002. Effects of the Protein Environment on the Structure and Energetics of Active Sites of Metalloenzymes. ONIOM Study of Methane Monooxygenase and Ribonucleotide Reductase. **J. Am. Chem. Soc.**, 124(2):192-193.
- Trens, P., N. Tanchoux, P.-M. Papineschi, D. Maldonado, F. di Renzo and F. Fajula. 2005. Confinement effects in MCM-41-type materials: Comparison of the energetics of n-hexane and 1-hexene adsorption. **Microporous Mesoporous Mater.**, 86(1-3):354-363.
- Twu, Y.J., C.W.S. Conover, Y.A. Yang and L.A. Bloomfield. 1990. Alkali-halide cluster ions produced by laser vaporization of solids. **Phys. Rev. B: Condens. Matter**, 42(8):5306-5316.

- van Baten, J.M. and R. Krishna. 2005. Entropy effects in adsorption and diffusion of alkane isomers in mordenite: An investigation using CBMC and MD simulations. **Microporous Mesoporous Mater.**, 84(1-3):179-191.
- Verlet, L. 1967. Computer "experiment" on classical fluids. I. Thermodynamical properties of Lennard-Jones molecules. **Phys. Rev.**, 15998-103.
- Wang, S., T. Dou, Y. Li, Y. Zhang, X. Li and Z. Yan. 2004. Synthesis, characterization, and catalytic properties of stable mesoporous molecular sieve MCM-41 prepared from zeolite mordenite. **J. Solid State Chem.**, 177(12):4800-4805.
- Weissenrieder, J., S. Kaya, J.L. Lu, H.J. Gao, S. Shaikhutdinov, H.J. Freund, M. Sierka, T.K. Todorova and J. Sauer. 2005. Atomic structure of a thin silica film on a Mo(112) substrate. A two-dimensional network of SiO<sub>4</sub> tetrahedra. **Phys. Rev. Lett.**, 95(7):076103/076101-076103/076104.
- White, J.A. and D.M. Bird. 1994. Implementation of gradient-corrected exchange-correlation potentials in Car-Parrinello total-energy calculations. **Phys. Rev. B**, 504954.
- Wojdel, J.C., M.A. Zwijnenburg and S.T. Bromley. 2006. Magic Silica Clusters as Nanoscale Building Units for Super-(Tris)tetrahedral Materials. **Chem. Mater.**, 18(6):1464-1469.
- Wongthong, P., R. Rungsirisakun, M. Probst and J. Limtrakul. 2007. Adsorption and diffusion of light alkanes on nanoporous faujasite catalysts investigated by molecular dynamics simulations. **Microporous Mesoporous Mater.**, 100(1-3):160-166.
- Woodley, S.M., P.D. Battle, J.D. Gale and C.R.A. Catlow. 1999. The prediction of inorganic crystal structures using a genetic algorithm and energy minimization. **PCCP**, 1(10):2535-2542.
- Wootton, A. and P. Harrowell. 2004. Polyhedral ground states in clusters of asymmetric hard sphere ions. **J. Chem. Phys.**, 121(15):7440-7442.
- Yun, J.-H., T. Dueren, F.J. Keil and N.A. Seaton. 2002. Adsorption of methane, ethane, and their binary mixtures on MCM-41: Experimental evaluation of methods for the prediction of adsorption equilibrium. **Langmuir**, 18(7):2693-2701.
- Zhang, L. and H. Huang. 2007. Structural transformation of ZnO nanostructures. **Appl. Phys. Lett.**, 90(2):023115/023111-023115/023113.

- Zhao, X.S., G.Q. Lu and X. Hu. 2001. Organophilicity of MCM-41 adsorbents studied by adsorption and temperature-programmed desorption. **Colloids Surf., A**, 179(2-3):261-269.
- \_\_\_\_\_, \_\_\_\_\_, A.K. Whittaker, G.J. Millar and H.Y. Zhu. 1997. Comprehensive Study of Surface Chemistry of MCM-41 Using  $^{29}\text{Si}$  CP/MAS NMR, FTIR, Pyridine-TPD, and TGA. **J. Phys. Chem. B**, 101(33):6525-6531.

## CURRICULUM VITAE

**NAME** : Mr. Winyoo Sangthong  
**BIRTH DATE** : February 24, 1980  
**BIRTH PLACE** : Phrae, Thailand  
**NATIONALITY** : Thai  
**EDUCATION** :  
 1998 – 2002 Chiang Mai University, B.Sc. (Chemistry)

### SCHOLARSHIPS / AWARDS:

1. The Development and Promotion of Science & Technology Talent Project (DPST) scholarship
2. The Thailand Research Fund Royal Golden Jubilee Ph. D. Program
3. Higher Education Development Project Scholarship Postgraduate Education and Research Program in Physical
4. The Kasetsart University Research and Development Institute (KURDI)

### PUBLICATIONS:

- 1. Computational study of the carbonyl-ene reaction of encapsulated formaldehyde in Na-FAU zeolite.**  
 Winyoo Sangthong, Michael Probst and Jumras Limtrakul. *Journal of Molecular Structure* 748 (2005) 119-127.
- 2. Confinement Effects on Adsorption and Diffusion of Hexane in Nanoporous MCM-41 with Different Pore Sizes: A Molecular Dynamics Study.**  
 Winyoo Sangthong, Michael Probst and Jumras Limtrakul. *Chemical Engineering Communications* 195 (2008) 1486-1501.
- 3. Stable Nanoporous Alkali Halide Polymorphs: a first principles theoretical bottom-up Study.**  
 Winyoo Sangthong, Jumras Limtrakul, Francesc Illas and Stefan T. Bromley. *Journal of Materials Chemistry* 18 (2008) 5871-5879.

**CONFERENCES / WORK SHOPS:****1. Comparing the stabilities of nanoclusters and cluster-based materials: alkali halides.**

Winyoo Sangthonga, Francesc Illas, Stefan T. Bromley, and Jumras Limtrakul. 9<sup>th</sup> RGJ Congress, Jomtien Palm Beach Hotel, Pattaya, Thailand, April 4-6, 2008. (Poster Presentations)

**2. Confinement Effects on Adsorption and Diffusion of Hexane in Nanoporous MCM-41 with Different Pore Sizes: A Molecular Dynamics Study.**

Winyoo Sangthong, Michael Probst and Jumras Limtrakul. The Proceeding of 32<sup>th</sup> Congress on Science and Technology of Thailand, Queen Sirikit National Convention Center, Bangkok, Thailand, October 10-12, 2006. (Oral Presentations)

**3. Computational study of the carbonyl-ene reaction of encapsulated formaldehyde in Na-FAU zeolite.**

Winyoo Sangthong, Michael Probst and Jumras Limtrakul. Abstracts of Papers, the 331<sup>st</sup> ACS National Meeting, San Diego, CA, United States, March 13-17, 2005. (Poster Presentations)